NASA/TM–2014-218171
NESC-RP-11-00697

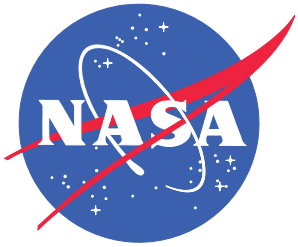

Orion Multi-Purpose Crew Vehicle (MPCV) Capsule Parachute Assembly System (CPAS) Wake Deficit Wind Tunnel Testing

James C. Ross
Ames Research Center, Moffett Field, California

David M Schuster/NESC
Langley Research Center, Hampton, Virginia

February 2014

NASA STI Program . . . in Profile

Since its founding, NASA has been dedicated to the advancement of aeronautics and space science. The NASA scientific and technical information (STI) program plays a key part in helping NASA maintain this important role.

The NASA STI program operates under the auspices of the Agency Chief Information Officer. It collects, organizes, provides for archiving, and disseminates NASA's STI. The NASA STI program provides access to the NASA Aeronautics and Space Database and its public interface, the NASA Technical Report Server, thus providing one of the largest collections of aeronautical and space science STI in the world. Results are published in both non-NASA channels and by NASA in the NASA STI Report Series, which includes the following report types:

- TECHNICAL PUBLICATION. Reports of completed research or a major significant phase of research that present the results of NASA Programs and include extensive data or theoretical analysis. Includes compilations of significant scientific and technical data and information deemed to be of continuing reference value. NASA counterpart of peer-reviewed formal professional papers, but having less stringent limitations on manuscript length and extent of graphic presentations.

- TECHNICAL MEMORANDUM. Scientific and technical findings that are preliminary or of specialized interest, e.g., quick release reports, working papers, and bibliographies that contain minimal annotation. Does not contain extensive analysis.

- CONTRACTOR REPORT. Scientific and technical findings by NASA-sponsored contractors and grantees.

- CONFERENCE PUBLICATION. Collected papers from scientific and technical conferences, symposia, seminars, or other meetings sponsored or co-sponsored by NASA.

- SPECIAL PUBLICATION. Scientific, technical, or historical information from NASA programs, projects, and missions, often concerned with subjects having substantial public interest.

- TECHNICAL TRANSLATION. English-language translations of foreign scientific and technical material pertinent to NASA's mission.

Specialized services also include organizing and publishing research results, distributing specialized research announcements and feeds, providing information desk and personal search support, and enabling data exchange services.

For more information about the NASA STI program, see the following:

- Access the NASA STI program home page at *http://www.sti.nasa.gov*

- E-mail your question to help@sti.nasa.gov

- Fax your question to the NASA STI Information Desk at 443-757-5803

- Phone the NASA STI Information Desk at 443-757-5802

- Write to:
  STI Information Desk
  NASA Center for AeroSpace Information
  7115 Standard Drive
  Hanover, MD 21076-1320

NASA/TM–2014-218171
NESC-RP-11-00697

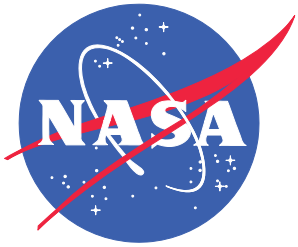

Orion Multi-Purpose Crew Vehicle (MPCV) Capsule Parachute Assembly System (CPAS) Wake Deficit Wind Tunnel Testing

James C. Ross
Ames Research Center, Moffett Field, California

David M Schuster/NESC
Langley Research Center, Hampton, Virginia

National Aeronautics and
Space Administration

Langley Research Center
Hampton, Virginia 23681-2199

February 2014

Available from:

NASA Center for AeroSpace Information
7115 Standard Drive
Hanover, MD 21076-1320
443-757-5802

Orion Multi-Purpose Crew Vehicle (MPCV) Capsule Parachute Assembly System (CPAS) Wake Deficit Wind Tunnel Testing

January 23, 2014

Report Approval and Revision History

NOTE: This document was approved at the January 23, 2014, NRB. This document was submitted to the NESC Director on February 13, 2014, for configuration control.

Approved:	*Original Signature on File*	2/13/14
	Acting NESC Director	Date

Version	Description of Revision	Office of Primary Responsibility	Effective Date
1.0	Initial Release	Dr. David Schuster, NASA Technical Fellow for Aerosciences, LaRC	1/23/14

Table of Contents

Technical Assessment Report

1.0 Notification and Authorization 7
2.0 Signature Page 8
3.0 Team List 9
3.1 Acknowledgements 9
4.0 Executive Summary 10
5.0 Introduction and Objectives 11
5.1 Boundary Layer Tripping Study 12
5.2 Transonic Wind Tunnel Test 12
6.0 Boundary Layer Tripping Study 13
6.1 Test Cell 2 at the Ames Research Center (ARC) Fluid Mechanics Laboratory (FML) 14
6.2 Trip Study at Texas A&M University Low-Speed Wind Tunnel 16
6.3 High-Reynolds Number Test of Orion CM 16
7.0 Transonic Wind Tunnel Test 17
7.1 Model Configuration 17
7.2 Model Mounting 17
7.3 CM Model Details 20
7.4 Instrumentation 25
8.0 Test Conduct 38
8.1 IR Thermography 40
8.2 PSP Measurements 47
8.3 PIV Measurements 50
8.4 Unsteady Pressure Measurements 58
8.5 Boundary Layer Measurements 62
9.0 Findings, Observations, and NESC Recommendations 64
9.1 Findings 64
9.2 Observations 65
9.3 NESC Recommendations 65
10.0 Alternate Viewpoint 65
11.0 Other Deliverables 65
12.0 Lessons Learned 65
13.0 Recommendations for NASA Standards and Specifications 65
14.0 Definition of Terms 66
15.0 Acronyms List 67
15.1 Nomenclature 67

16.0 References 68
17.0 Appendices 70

List of Figures

Figure 6.1-1. MPCV CM Model Mounted in 32x48-inch FML Subsonic Wind Tunnel 14
Figure 6.1-2. IR Image of the Orion Model Showing Transition on the Heatshield at the Trip Location 15
Figure 6.1-3. Oil Flow Visualization on the Heatshield Corresponding to the IR Image in Figure 6.1-2 16
Figure 7.1-1. Definition of Smooth CM Geometry (dimensions are model-scale inches); x- and z-Axes are shown with the Origin at the Heatshield Apex 17
Figure 7.2-1. Oblique View of the Model Support Strut Arrangement 18
Figure 7.2-2. Side and Top Views of Model Installation showing the Lateral Offset Cable Arrangement (without cable fairings) and the Floor Plates and Feet at the Base of the Lower Struts 19
Figure 7.2-3. Interior Pivot and Pivot Cover Plates on the CM Model 20
Figure 7.3-1. Computer-Aided Design (CAD) Image of the CM Mounted to Struts showing Cover Plates, Boundary Layer Probe, and Leveling Plate 21
Figure 7.3-2. Pin and Bolt Arrangements for the Three CM AoAs 21
Figure 7.3-3. Back Shell Design showing Inner Details 22
Figure 7.3-4. Unsteady Transducer Insert 23
Figure 7.3-5. Cutout in Heatshield Shoulder to Accommodate an Unsteady Transducer Insert 23
Figure 7.3-6. Rough Heatshield Surface 24
Figure 7.3-7. Dimples Machined into Rough Heatshield Surface 24
Figure 7.4-1. Pressure Tap Layout on the Heatshield, K1-K40 are Unsteady Transducers 26
Figure 7.4-2. Pressure Tap Layout on the Heatshield and Back Shell, K1-K44 are Unsteady Transducers 27
Figure 7.4-3. Kulite® Transducer Holder 28
Figure 7.4-4. Layout of Cameras and Lights around Test Section in Vinci Modeling Tool (view of right-hand wall; wind is right to left) 29
Figure 7.4-5. Illumination quality (left) and Camera View Angle Relative to Surface Normal (right) for PSP Cameras 29
Figure 7.4-6. Traversing Boundary Layer Total-Pressure Probe, Stanton Gauge, and Static Pressure Tap 30
Figure 7.4-7. Boundary Layer Insert 30
Figure 7.4-8. Boundary Layer Insert Mounted in Rough Heatshield 31
Figure 7.4-9. Strain Gauges on Left Upper Strut 32
Figure 7.4-10. Laser Sheet Paths in 11x11-ft Test Section 34
Figure 7.4-11. PIV Laser Sheets 35
Figure 7.4-12. PIV Imaging Areas for Both Model Positions 36

Figure 8.1-1. IR Image of the Rough Heatshield at Mach 0.7, AoA 30 degrees, and Reynolds Number 10^7 41
Figure 8.1-2. PSP Image Compared to IR Image with Temperature Range to Show Stagnation Point; Rough Heatshield at Mach 0.3, AoA of 15 degrees, and Reynolds Number $5.3x10^6$ 42
Figure 8.1-3. IR Image Showing Changes in Flow Structure with Increasing Mach Number 42
Figure 8.1-4. IR Images of Heatshield taken with the Ceiling Mounted Camera at Mach 0.5, AoA of 30 degrees, and Reynolds Number $1.33x10^6$ 43
Figure 8.1-5. Difference in Roughness Depth Across Machining Seam 44
Figure 8.1-6. Top-view IR Image of Smooth Heatshield; M = 0.7, AoA of 30 degrees, and Reynolds Number $10x10^6$ 44
Figure 8.1-7. Side-view of IR Image; M = 0.7, AoA of 30 degrees, and Reynolds Number $10x10^6$ 45
Figure 8.1-8. Map of Defects on Smooth Heatshield 46
Figure 8.1-9. IR Image of Smooth Heatshield Mach 1.02, AoA of 30 degrees, and Reynolds Number $1.33x10^6$ 47
Figure 8.2-1. Pressure Distributions on CM at AoA of 30 Degrees 48
Figure 8.2-2. Axial Force Coefficient Variation with Mach Number 50
Figure 8.3-1. Average Velocity in CM Wake; Mach 0.7, AoA of 14.0 degrees, and Reynolds Number $10x10^6$ Color Contours of Vx, Every 10^{th} Vector Shown 51
Figure 8.3-2. RMS of Vx in CM Wake; Mach 0.7, AoA of 14.0 degrees, and Reynolds Number $10x10^6$ 52
Figure 8.3-3. Velocity Measurements from High-speed PIV; Mach 0.3, AoA of 14.0 degrees Reynolds Number $5.3x10^6$, and V_∞ = 103 m/s 53
Figure 8.3-4. RMS X-velocity Measurements from High-speed PIV; Mach 0.3, AoA of 14.0 degrees, and Reynolds Number $5.3x10^6$ 53
Figure 8.3-5. Distribution of V_x Along Center of Wake at Mach 0.7, AoA of 13.9 degrees, and Reynolds Number 10^7 54
Figure 8.3-6. Variation in Total Velocity at Various Downstream Locations; Mach 0.7, AoA of 13.9 degrees, and Reynolds Number 10^7 55
Figure 8.3-7. Contours of V_x in Far-field Wake (Mach 0.7, AoA of 15 degree) at an Instant Showing Low Velocity Across Approximate Drogue Parachute Diameter, V_∞ = 234 m/s 56
Figure 8.3-8. Contours of V_x in Far-field Wake (Mach 0.7, AoA of 15 degrees) at an Instant Showing High Velocity Across Approximate Drogue Parachute Diameter, V_∞ = 234 m/s 56
Figure 8.3-9. DLC from Current Study Compared to Results in Reference 1 58
Figure 8.4-1. 1/3-octave SPL Levels for Unsteady Pressures; Mach 0.7, AoA of 29.25 degrees, and Reynolds Number $10x10^6$ 59
Figure 8.4-2. Narrow Band SPL Levels Showing Effect of Roughness on Shedding Frequency; Mach 0.7, AoA of 29.25 degrees, and Reynolds Number $10x10^6$ 60

Figure 8.4-3. Narrow Band SPL Levels Showing Effect of Mach Number on Shedding Frequency; Mach 0.7, AoA 29.25 degrees, and Reynolds Number $10x10^6$ 61
Figure 8.4-4. Correlation Coefficient versus Time Referenced to Sensor K8; Mach 0.7, AoA of 29.25 degrees, and Reynolds Number $10x10^6$ 62
Figure 8.5-1. Boundary Layer Profiles for Rough Heatshield 63
Figure 8.5-2. Example of Oil Film Images for Measuring Skin Friction; Mach 0.7, AoA of 15 degrees, and Reynolds Number $10x10^6$, Skin Friction Coefficient = 0.0026 directed 4.6 degrees from Vertical 64

List of Tables

Table 5.2-1. Runs Accomplished during AUPWT Test (numbers in the boxes indicate the Reynolds Number) 13
Table 7.4-1. Flow Statistics in Archived PIV Data Files 37
Table 8.0-1. List of Runs Accomplished During Test 38
Table 8.2-1. Integrated Forces and Moments from Surface Pressures 49

Technical Assessment Report

1.0 Notification and Authorization

Dr. David Schuster, NASA Technical Fellow for Aerosciences at the NASA Langley Research Center, was selected to lead this assessment. The assessment plan was approved by the NASA Engineering and Safety Center (NESC) Review Board on May 12, 2011.

The key stakeholders for this assessment are the Orion Multi-Purpose Crew Vehicle Capsule Parachute Assembly System Project and the Crew Exploration Vehicle Aerosciences Project. The Agency's wind tunnel test facilities are also a key stakeholder.

2.0 Signature Page

Submitted by:

Team Signature Page on File – 2/25/14

Dr. David M. Schuster Date

Significant Contributors:

Dr. James C. Ross Date

Mr. J. T. Heineck Date

Dr. Gloria K. Yamauchi Date

Mr. Theodore J. Garbeff Date

Mr. Marvin Sellers Date

Ms. Laura K. Kushner Date

Ms. Nettie Halcomb Date

Mr. Nathan J. Burnside Date

Signatories declare the findings, observations, and NESC recommendations compiled in the report are factually based from data extracted from program/project documents, contractor reports, and open literature, and/or generated from independently conducted tests, analyses, and inspections.

3.0 Team List

Name	Discipline	Organization
Core Team		
David Schuster	NASA Technical Fellow for Aerosciences	LaRC
James Ross	Aerospace Engineer	ARC
Patricia Pahlavani	MTSO Program Analyst	LaRC
J.T. Heineck	Photographic Technologist	ARC
Gloria Yamauchi	Aerospace Engineer	ARC
Theodore Garbeff	Instrumentation Engineer	ARC
Marvin Sellers	Senior Engineer	Aerospace Testing Alliance
Laura Kushner	Senior Engineer	Aerospace Computing, Inc.
Nettie Halcomb	Aerospace Engineer	ARC
Nathan Burnside	Aerospace Engineer	ARC
Administrative Support		
Diane Sarrazin	Project Coordinator	LaRC/AMA
Linda Burgess	Planning and Control Analyst	LaRC/AMA
Christina Williams	Technical Writer	LaRC/AMA

3.1 Acknowledgements

The staff at the Ames Research Center Unitary Plan Wind Tunnel provided outstanding support for the test, keeping the test on track. Management instituted customized shift hours that matched the unusual nature of the test and made test execution more efficient. The Facility Manager, John Holmberg, was invaluable in solving many problems during the testing. The Test Manager, Jennifer Everett, and Test Engineer, Ross Flach, were key contributors in balancing the needs of the test with the practical aspects of completing the test in the allotted time.

4.0 Executive Summary

Sizing of the parachute system for the Multi-Purpose Crew Vehicle (MPCV) is critical for safe operation. In particular, the drogue parachutes need to be large enough to ensure reliable deployment and inflation, but making them too large unnecessarily increases the load on the vehicle, system weight, and packing volume. The wake deficit at the drogue parachute location behind the capsule is the primary parameter that determines the size of the parachutes. Empirical wake deficit estimates are available in the literature, but their validity for all configurations is not well documented. A computational method of determining the wake deficit would be preferred, but the available computational fluid dynamics (CFD) tools have not been reliable for predicting bluff body separation and wake development at the Mach numbers expected for drogue parachute deployment. This test provides data at a variety of relevant flight conditions to validate the computational tools. The data provided the Orion Capsule Parachute Assembly System (CPAS) team with a measured wake deficit value to verify the value selected for their drogue parachute design.

The model tested in this assessment was an approximately 8 percent-scale generic/axisymmetric Orion crew module (CM). Measurements included the surface pressure distribution, skin friction at a point on the heatshield, separation locations around the heatshield shoulder, and velocity measurements in the CM wake to the drogue parachute location. The test was conducted at Mach numbers of approximately 0.3, 0.5, 0.7, 0.9, and 1.05, and angles of attack (AoA) of 15 and 30 degrees. A brief study was done to examine the effect of heatshield roughness, but the majority of the data was acquired using a heatshield model that approximated the post-entry roughness of an MPCV Avcoat heatshield.

The acquired data demonstrated the separated wake behind the CM was highly unsteady for all conditions tested, and the level of unsteadiness increased as the capsule AoA decreased and the heatshield was pointed directly into the flow (i.e., from 30 towards 0 degrees). In general, the testing confirmed that handbook wake persistence estimates were conservative, but these estimates do not effectively account for the unsteadiness of the wake flow or motion, which could be important to parachute design. Heatshield roughness was found to be an important contributor to the wake flowfield character and should be accounted for in future testing of these classes of vehicles.

The surface and off-body flowfield data acquired and archived in this test are suitable for CFD code validation and comprise a unique dataset characterizing the unsteady flow behind a blunt capsule body. With the accelerating development of CFD tools for predicting unsteady separated flows, this dataset should be an important contributor to the validation of these future computational methods.

5.0 Introduction and Objectives

During descent after re-entry into the Earth's atmosphere, the Orion CM deploys its drogue parachutes at approximately Mach 0.7. Accurately predicting the dynamic pressure experienced by the drogue parachutes at deployment is critical to properly designing the parachutes. Previous recovery system designs made extensive use of data manuals to estimate the dynamic pressure at the parachute location [ref. 1]. The Orion CPAS team wanted improved estimates and employed CFD methods to model the flow around the capsule at the drogue parachute deployment condition. Unfortunately, this flight condition proved difficult to accurately model with CFD. The flow in the wake was difficult to measure in a wind tunnel since the model is usually mounted on a sting located in the wake region. The prediction and measurement shortcomings led to uncertainty in the Orion parachute system design. This shortcoming affected the CM aerodynamic predictions during descent leading to a mismatch between the aerodynamic database and the capsule aerodynamics measured during the Pad Abort 1 flight test.

The task of predicting and measuring the MPCV CM aerodynamics was complicated by uncertainty concerning the boundary layer state on the heatshield. Based on the Reynolds number for the descent trajectories, the heatshield boundary layer is expected to be turbulent. After entering the atmosphere from the Earth's orbit or lunar return, the heatshield surface is roughened due to Avcoat ablation from the high temperatures encountered. The roughness forces the boundary layer to be turbulent from the stagnation point with additional turbulent kinetic energy generated by the flow over the rough surface. The flow also experiences a favorable pressure gradient, which tends to stabilize the boundary layer and delay transition, particularly at the lower Reynolds numbers encountered in wind tunnel testing. During a potential launch abort (i.e., pad or ascent), the CM may experience lower Reynolds numbers at drogue-chute deployment with a smooth heatshield, resulting in larger areas of laminar boundary layer. Therefore, simulating the desired boundary layer state in the wind tunnel becomes even more problematic for this type of vehicle than for typical aircraft, which the team has a much broader experience base. This test, and other similar experiments, addresses the issue of modeling a rough heatshield and employs innovative techniques to simulate the proper boundary layer state on capsules in a wind tunnel.

This assessment was designed to provide a complete set of flowfield measurements on and around an idealized Orion CM shape with the most appropriate wind tunnel simulation of the Orion flight conditions prior to parachute deployment. The first part of the study was to examine potential boundary layer tripping strategies to best simulate flight conditions. The bulk of the effort was spent performing a high-fidelity wind tunnel test in the Ames Unitary Plan Wind Tunnel (AUPWT). The test covered a range of Mach numbers, Reynolds numbers, and AoAs. The data includes full-body pressure distributions using pressure sensitive paint (PSP) anchored to approximately 60 discrete surface static pressure taps; infrared (IR) thermography to capture boundary layer transition and separation locations; particle image velocimetry (PIV) measurements of the velocity in the CM model wake; unsteady pressure measurements on the

heatshield shoulder and back shell; boundary layer surveys at one heatshield location; and skin friction at a point adjacent to the boundary layer survey.

The CM model was a smooth body to avoid obscuring important flow physics with local flow disturbances from protuberances. The model was mounted in the wind tunnel so as to minimize the influence of the mounting struts on the model wake flow in a downstream vertical plane where air velocity was measured across the full wake.

5.1 Boundary Layer Tripping Study

Before running the more expensive test in the AUPWT, a smaller effort was undertaken to study the effect of various boundary layer tripping strategies on the CM aerodynamics. For most wind tunnel tests, the boundary layer is tripped using roughness elements. These elements can be made from wires or tape, lines of grit or small adhesive dots, or grit distributed over the surface. There are established criteria for determining the size of these roughness elements based on the flight conditions to be simulated and the conditions in the wind tunnel for aircraft models [refs 2, 3]. The criteria are different for wings and fuselages, but are established for both types of flows. Most aircraft manufacturers have refined their own sizing methods to ensure tripping the flow from laminar to turbulent with minimal drag increments due to the drag of the roughness elements themselves.

The flow on the blunt entry capsule heatshield is different than found on most aircraft so it may be that those methods do not apply directly or may need modification. Two wind tunnel tests were included in this effort to determine what an appropriate tripping strategy should be for a capsule after re-entry.

5.2 Transonic Wind Tunnel Test

The comprehensive test of the CM model was performed in the 11x11-foot (ft) transonic wind tunnel test section of the AUPWT [ref. 4]. This test facility can obtain Mach numbers from 0.3 to 1.4. The total pressure in the facility can be varied from 0.5 to 2.0 atmospheres providing a range of Reynolds numbers. The first priority of the transonic wind tunnel test was to document the velocity deficit into which the Orion drogue parachute is deployed at Mach 0.7. A longer term objective was to gather aerodynamic and flowfield data for the purpose of validating CFD methods. The measurements made in the wind tunnel included velocity distributions in the wake, time-averaged surface pressure distribution over the entire model, unsteady pressures around the heatshield shoulder, transition location on the heatshield, separation lines on the heatshield shoulder region, and skin friction on the heatshield. Time-averaged flowfield velocity measurements were made in a vertical plane downstream of the CM model from as close to the model as possible to approximately 6 model diameters downstream. A second set of high-rate (i.e., 1900 frames/second) velocity measurements were made in a smaller horizontal plane in the model near wake.

The surface measurements were made at Mach numbers of approximately 0.3, 0.5, 0.7, 0.9, and 1.05, and AoAs of 15 and 30 degrees. A limited number of measurements were acquired at

0 degree AoA. The PIV measurements were made only for 15 degrees AoA and Mach numbers of 0.3, 0.5, and 0.7. These conditions cover the expected Orion parachute deployment and lower Mach numbers to allow more comprehensive CFD tool validation. The test conditions and types of data acquired are shown in Table 5.2-1.

Table 5.2-1. Runs Accomplished during AUPWT Test (numbers in the boxes indicate the Reynolds Number)

Pressure Sensitive Paint, IR Thermography, Unsteady Pressures, Schlieren

Heat Shield	Angle of Attack	Mach 0.3	Mach 0.5	Mach 0.7	Mach 0.9	Mach 1.05
Smooth	30°			$1.3x10^6$		$1.3x10^6$
Smooth	30°	$5.3x10^6$	$8.7x10^6$	$10x10^6$	$10x10^6$	$10x10^6$
Rough	15°	$5.3x10^6$	$8.7x10^6$	$10x10^6$	$10x10^6$	$10x10^6$
Rough	30°			$1.3x10^6$		$1.3x10^6$
Rough	30°	$5.3x10^6$	$8.7x10^6$	$10x10^6$	$10x10^6$	$10x10^6$

Boundary-Layer Surveys, Skin Friction, IR Thermography

Heat Shield	Angle of Attack	Mach 0.3	Mach 0.5	Mach 0.7	Mach 0.9	Mach 1.05
Rough	0°	$5.3x10^6$	$8.7x10^6$	$10x10^6$		
Rough	15°	$5.3x10^6$		$10x10^6$		$6.6x10^6$
Rough	30°	5.3x107		10x107		6.6x107

Particle Image Velocimetry, Unsteady Pressures, Schlieren

Model Position	Angle of Attack	Mach 0.3	Mach 0.5	Mach 0.7	Mach 0.9	Mach 1.05
Downstream	15°	$5.3x10^6$	$8.7x10^6$	$10x10^6$		$10x10^6$
Upstream	15°	$5.3x10^6$	$8.7x10^6$	$10x10^6$		

6.0 Boundary Layer Tripping Study

Two studies were performed in preparation for the main test in the AUPWT. The first was to apply IR thermography on a capsule model to ensure the flow features of interest would be visible and to obtain experience with the IR camera. This practice was in preparation for the second part of the study at Texas Agricultural and Mechanical (A&M) University to look at the effects of different tripping strategies on the CM aerodynamics and flow structure. In addition, the IR image quality was examined for the models fabricated of aluminum and from nylon using selective laser sintering (SLS).

6.1 Test Cell 2 at the Ames Research Center (ARC) Fluid Mechanics Laboratory (FML)

The first test was performed in the ARC FML Test Cell 2 32x48-inch subsonic wind tunnel. The model used in the study is shown in Figure 6.1-1, mounted on a sting and balance. The SLS material is white and fairly rough when manufactured so the model was filled and painted to give a smooth heatshield. The black color provided good contrast with the white oil (Figure 6.1-1) used for flow visualization with IR imagery.

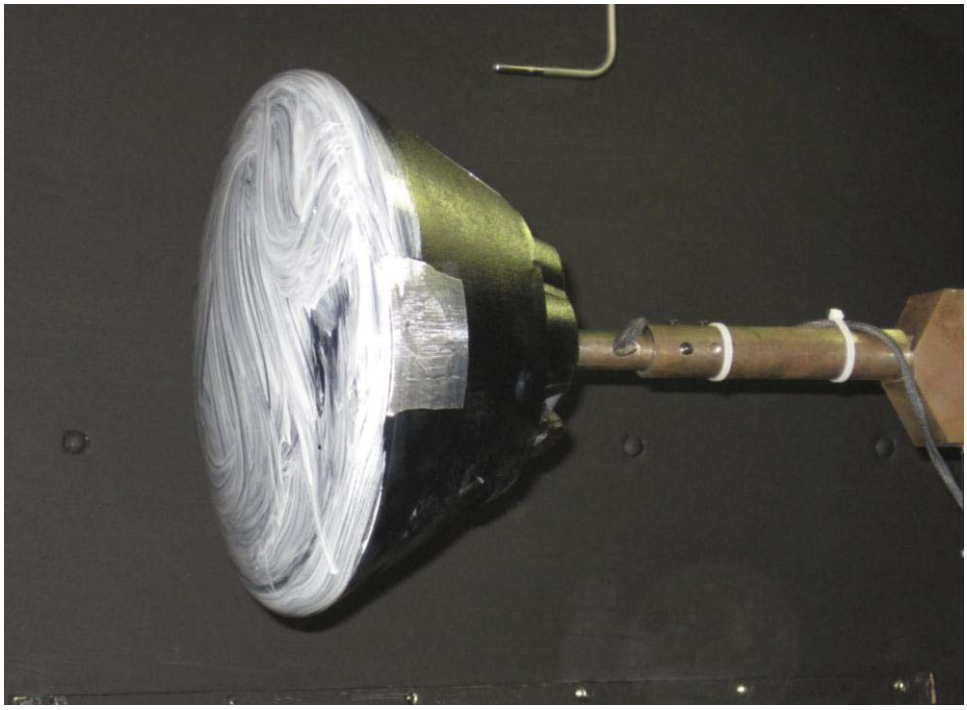

Figure 6.1-1. MPCV CM Model Mounted in 32x48-inch FML Subsonic Wind Tunnel
Note: For flow visualization, white oil is spread on the model heatshield prior to tunnel operation.

This study generated IR imagery showing detail about the flow over the model surface. Since this is a low-speed indraft wind tunnel, the flow temperature was nearly the ambient temperature and essentially the same as the model. Therefore, prior to each run, the model was heated above the ambient by approximately 20 degrees. This was done to enhance the flow-induced temperature differences on the models surface using the IR camera. The images in Figures 6.1-2 and 6.1-3 show an IR image and the corresponding oil flow visualization. In this case, a boundary layer trip was applied to the heatshield consisting of a band of course grit (~60 grit). The oil was applied from the trip outboard on the heatshield and showed separation occurring near the start of the heatshield shoulder (Figure 6.1-3). The IR image in Figure 6.1-2 was taken through the only available open hole in the tunnel wall, which was perpendicular to the heatshield shoulder. This image shows transition occurring at the trip location and the separation at the same location as in the oil flow visualization.

The images obtained during this test demonstrated the IR images would show transition from laminar to turbulent flow and possibly show the separation line. The main concern for this technique was maintaining a temperature difference between the airstream and the interior model temperature. Since the technique had been successful when used in the AUPWT 11x11-ft test section, the FML results indicated the IR cameras had sufficient sensitivity to show the desired flow features.

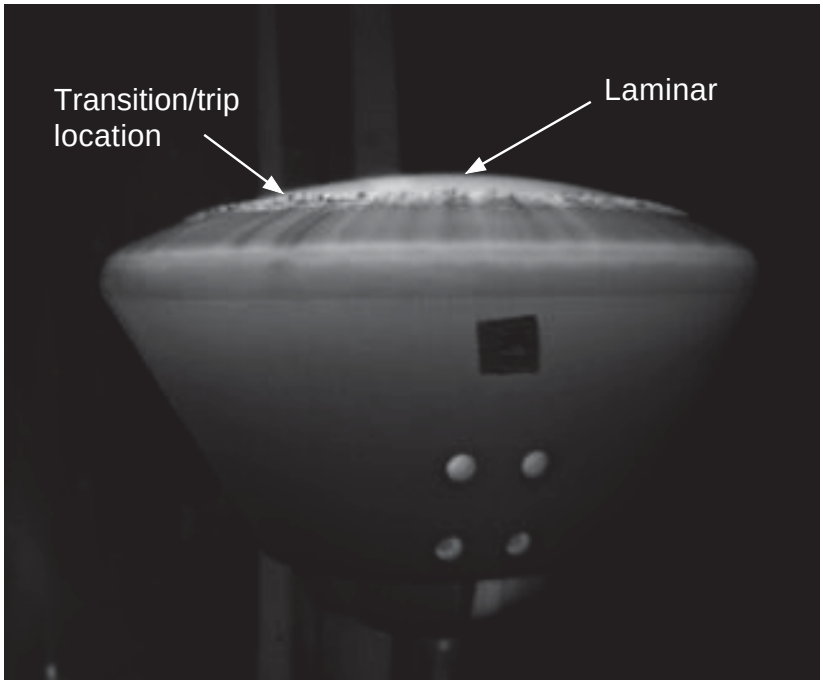

Figure 6.1-2. IR Image of the Orion Model Showing Transition on the Heatshield at the Trip Location

Figure 6.1-3. Oil Flow Visualization on the Heatshield Corresponding to the IR Image in Figure 6.1-2
Note: Streaky oil may be coincident with the streaks in IR image; separation is indicated by the white band around the shoulder.

6.2 Trip Study at Texas A&M University Low-Speed Wind Tunnel

The CEV CPAS team performed a study of wake flows and parachute loads downstream of the Orion CM in the 7x10-ft Low-Speed Wind Tunnel at Texas A&M University [ref. 5]. The test used an aluminum, 24-inch diameter, smooth CM model mounted on a six-component balance. Model drogue parachutes were flown in the CM wake on load cells to measure the loads. The first portion of the test was used to determine the most appropriate method of tripping the boundary layer to simulate higher Reynolds number flight.

This test resulted in interesting data, but was limited due to the time constraints. The main conclusion from the test was that distributed roughness using carborundum grit produced different aerodynamics than trip rings made from the standard Mylar® trip dots.

6.3 High-Reynolds Number Test of Orion CM

The Orion Aeroscience team performed a test in the National Transonic Facility at LaRC to determine the effect of Reynolds number on the CM subsonic/transonic aerodynamics [ref. 6]. The test was run at low and at flight-relevant Reynolds numbers. In addition, the effect of heatshield roughness was examined. The test showed there was a significant effect of roughness (i.e., representative of post-entry Avcoat) on the subsonic aerodynamics. In particular, the rough heatshield increased the CM drag coefficient by approximately 10 percent at a Mach number of 0.3 and Reynolds number of 24 million based on CM diameter. As the Mach number increased,

the change in drag due to roughness decreased until Mach 0.8. Above Mach 0.8, there was no measurable difference due to roughness.

7.0 Transonic Wind Tunnel Test

7.1 Model Configuration

The model was an 8.08 percent-scale (16-inch diameter) representation of the smooth, axisymmetric Orion CM shape. It did not include any of the protuberances or other details on the back shell or heatshield. The geometry definition and the x- and z-axes are shown in Figure 7.1-1 where the y-axis is directed into the page. The origin of the model coordinate system is as shown, at the apex of the heatshield.

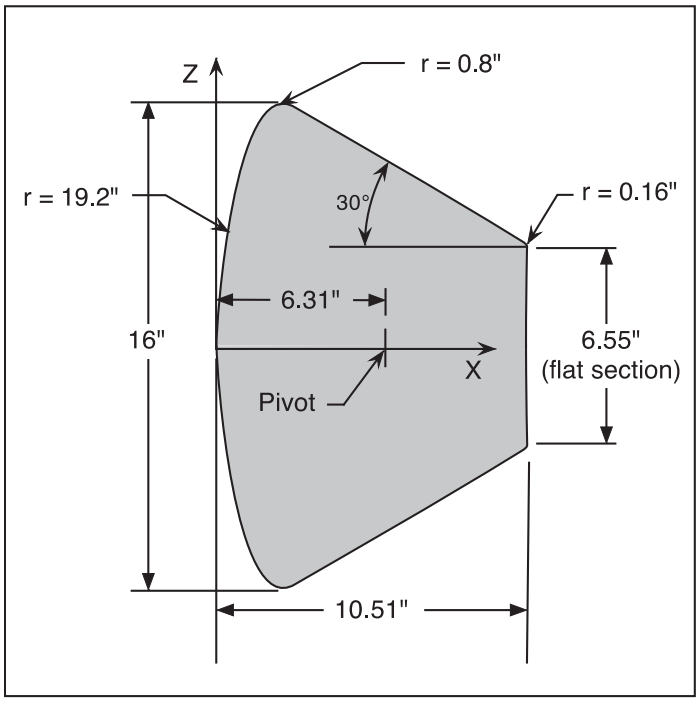

Figure 7.1-1. Definition of Smooth CM Geometry (dimensions are model-scale inches); x- and z-Axes are shown with the Origin at the Heatshield Apex

7.2 Model Mounting

The model was mounted on a pair of struts attached to the floor of the 11x11-ft wind tunnel test section as shown in Figure 7.2-1. The struts were designed to locate the model at two axial and two lateral positions. One axial location placed the model so the vertical wake measurement plane covered the area from the heatshield shoulder to ~3 model diameters downstream while the other axial location allowed the same measurement plane to cover a region to ~6 model diameters downstream. The two lateral locations were on the test section centerline and

4 inches to the left of the centerline (y/D = -0.25). Data were only acquired for the forward and aft positions on the tunnel centerline due to time constraints.

The model was mounted on struts in the wind tunnel to minimize the influence of the model support on the wake flow, particularly in a vertical plane downstream where the PIV measurements were made. Figure 7.2-2 shows the model and struts mounted in the wind tunnel. Model motions were minimized by stabilizing the upper mounting struts with cables to reduce the uncertainty in the various optical measurements. The cables were attached to the test section floor upstream and outboard of the strut attachment points. The upper struts were instrumented with strain gauges near their attachment to the lower struts and on the model side of the cable attachment fairings. The gauges were calibrated with known loads in the lift and drag directions and monitored during the test for safety. The resulting support was very rigid and the model moved less than 0.25 inches (0.015D) due to the mean aerodynamic load. The unsteady model motion was less than 0.1 inch (~0.006D).

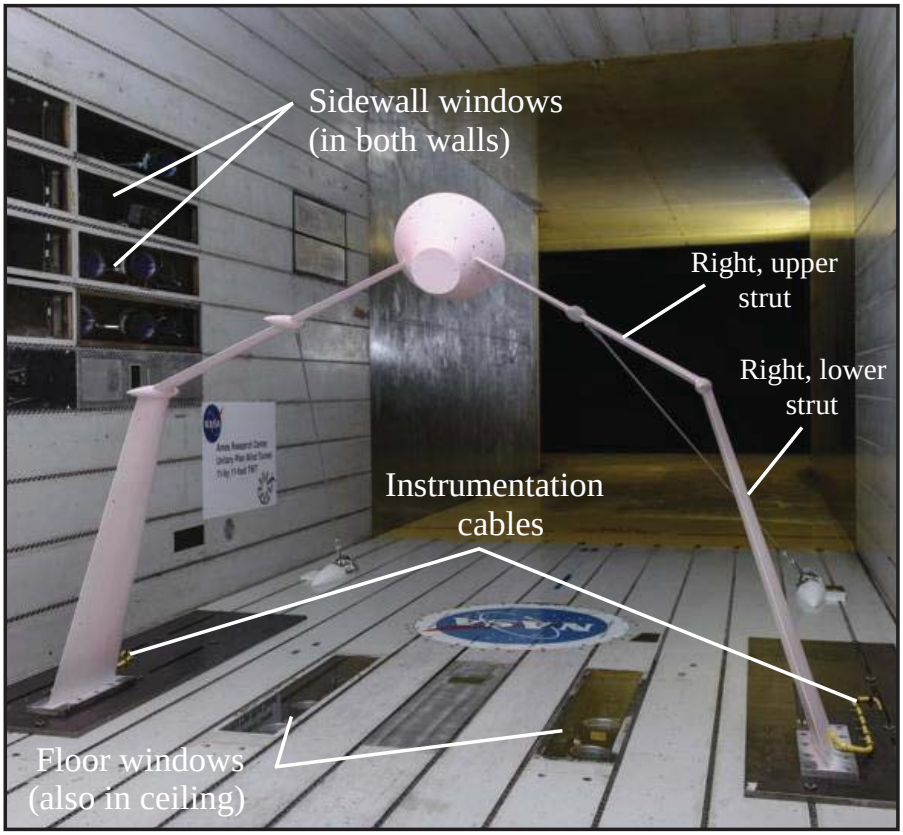

Figure 7.2-1. Oblique View of the Model Support Strut Arrangement

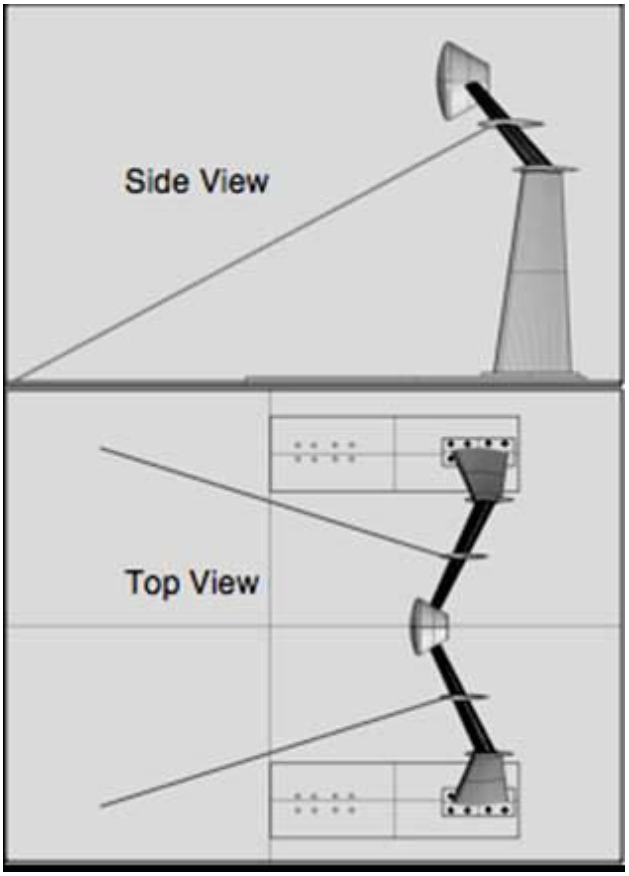

Figure 7.2-2. Side and Top Views of Model Installation showing the Lateral Offset Cable Arrangement (without cable fairings) and the Floor Plates and Feet at the Base of the Lower Struts

The struts are untwisted, tapered 65_4-021 airfoil sections truncated at the 95 percent chord location. The fairings at the upper-to-lower strut junctions provided more bearing area for the bolted joint. The fairing at the junction of the cables and upper struts provided a better aerodynamic shape for the junction to minimize any disturbance to the wake downstream.

The cables were intended to have pivoting fairings to minimize their wakes. During the initial runs of the wind tunnel test the fairings did not pivot into the wind as intended. They were removed and the test was completed without them. The large sweep angle of the cables relative to the flow helped reduce the cable wake.

The model was pivoted at the ends of the mounting struts to AoAs of 0, 15, and 30 degrees. Removable filler pieces around the strut/model intersection maintained the correct model geometry and made a tight seal around the strut tips. The model set at 0 degree AoA was positioned in the wind tunnel by placing the model origin (heatshield apex) at x = 151.7, y = 0.0, and z = -4.9 inch (wind-tunnel coordinates). The rotation center is shown in Figure 7.1-1. The

CM pivot is shown on the model in Figure 7.2-3. The AoA was set by matching specific pin and bolt holes on the strut flange and the CM model.

Figure 7.2-3. Interior Pivot and Pivot Cover Plates on the CM Model

The major objective of the test was to document the wake flowfield up to 6-model diameters downstream. The resulting area of interest was too large to image using the available cameras so either the model or PIV system would have to move to cover the entire region. PIV systems are difficult to set up, align, and calibrate, so the model was moved relative to the measurement plane to acquire velocity data in the near wake and far downstream. The floor plates were drilled and tapped with two bolt patterns for the lower strut attachments, spaced 4 ft apart in the streamwise direction. After all the measurements were made, with the model in the aft position, the lower struts were unbolted from the floor plates and the model was moved to the upstream position and bolted to the second set of threaded holes. The yellow cables in Figure 7.2-1 are the bundles of instrumentation cables that ran through holes bored through the struts with sufficient slack to move the model to the second mounting location.

7.3 CM Model Details

Figure 7.3-1 shows the CM mounted to the struts with the leveling plate and the boundary layer survey probe installed. The strut attachments were covered with a split cover plate that restores the proper back shell shape around the strut penetration. Three sets of cover plates were required for the test (i.e., one for each AoA). The cover plates were manufactured using polycarbonate SLS that was tailor fit around the upper strut tips and flush to the surrounding back shell surfaces. The leveling plate was used to mount a precision inclinometer to establish the installed AoA in the wind tunnel.

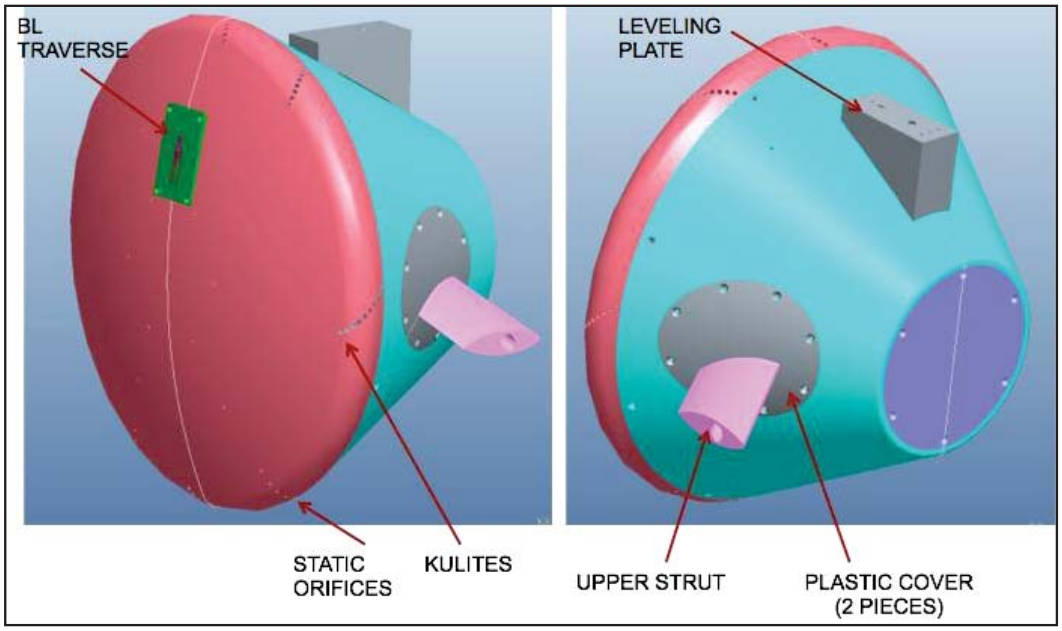

Figure 7.3-1. Computer-Aided Design (CAD) Image of the CM Mounted to Struts showing Cover Plates, Boundary Layer Probe, and Leveling Plate

Figure 7.3-2 shows the pin and bolt arrangement for changing the CM AoA. A single pin and three bolts on one side of the model were sufficient to carry the pitching moment CM with the required factor of safety. The test was run with a pin and at least five bolts on each side.

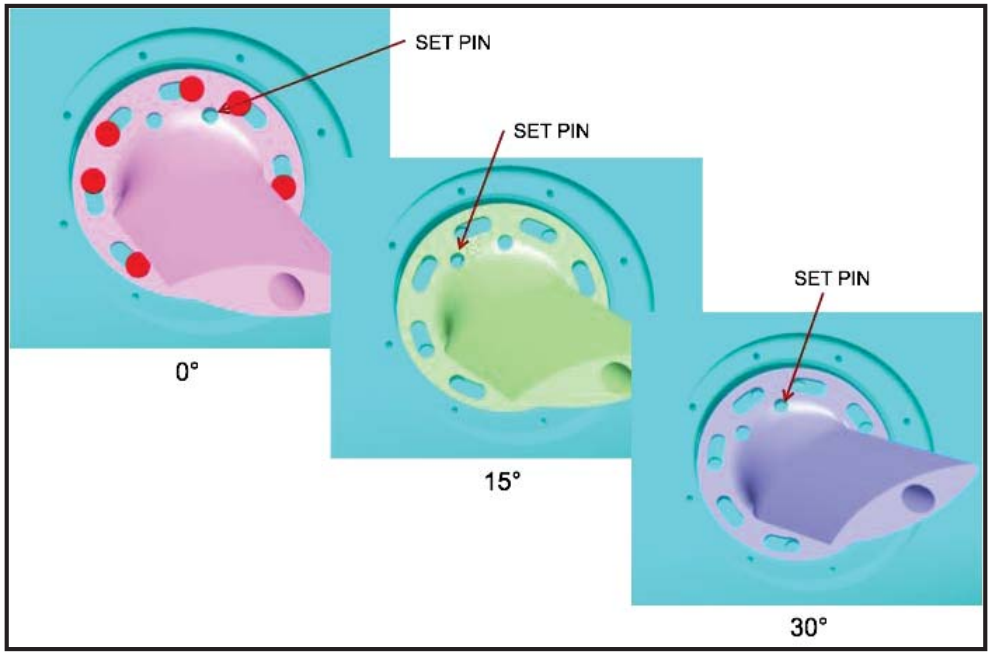

Figure 7.3-2. Pin and Bolt Arrangements for the Three CM AoAs

The CM back shell was fabricated using normal machining techniques from a billet of 7075 aluminum. Figure 7.3-3 shows the details of the inside of the part. The two pivot points and the associated bolt/pin holes are evident in this view as is the mount at the bottom for the AoA sensor. Steel inserts were used for the pivot bearing surface. The strut pocket holes were for quick disconnects that attached the pressure tap tubing from the strut cover plates. A circular flat plate closes the hole of the truncated CM apex.

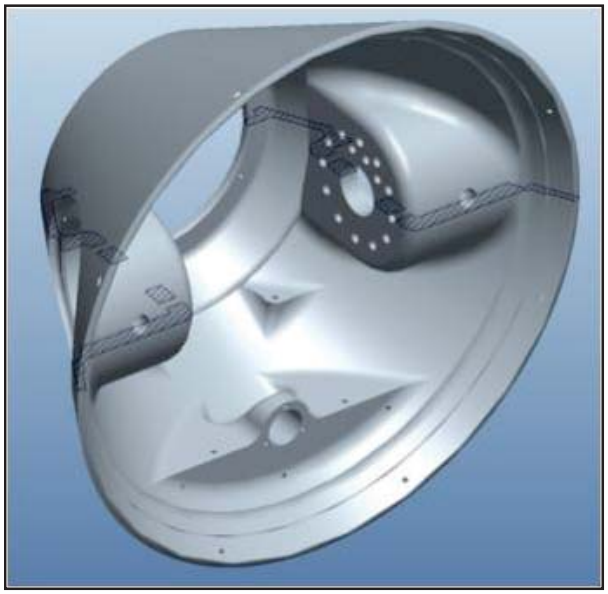

Figure 7.3-3. Back Shell Design showing Inner Details

The heatshield was a two-layer part with an inner layer of turned 7075 aluminum to which a 0.25-inch outer layer of SLS polycarbonate was bonded prior to final machining of the outer surface. This was done to improve the IR imaging based on the prior testing done in the ARC FML using the plastic model, and at the Texas A&M's 7x10-ft low-speed wind tunnel using the aluminum model. The plastic model in the preliminary tests provided a better IR imagery.

Two heatshields were made for the test: one smooth and the other machined with a hexagonal dimple pattern to simulate the expected roughness of the Orion heatshield after atmospheric entry. Because of the expense and lead time to acquire the unsteady pressure transducers, four inserts were made to hold ten transducers each that could be installed in the heatshield. The inserts were made from polycarbonate SLS and machined with the smooth heatshield outer surface to get the correct shape. An image of one insert is shown in Figure 7.3-4 and its corresponding recess in the smooth heatshield is shown in Figure 7.3-5.

Figure 7.3-4. Unsteady Transducer Insert

Figure 7.3-5. Cutout in Heatshield Shoulder to Accommodate an Unsteady Transducer Insert
Note: The red material is epoxy to fill a crack in the polycarbonate material.

The machined surface of the rough heatshield is shown in Figures 7.3-6 and 7.3-7. The fit of the unsteady pressure transducer insert is shown in Figure 7.3-6 (flush with the tops of the dimpled pattern). The details of the pattern are shown in Figure 7.3-7 with the dimensions, which were determined by physically scaling the expected roughness pattern of the Orion Avcoat heatshield

material after atmospheric entry [ref. 7]. The pink color of the dimpled heatshield was due to the PSP coating that was applied prior to the test.

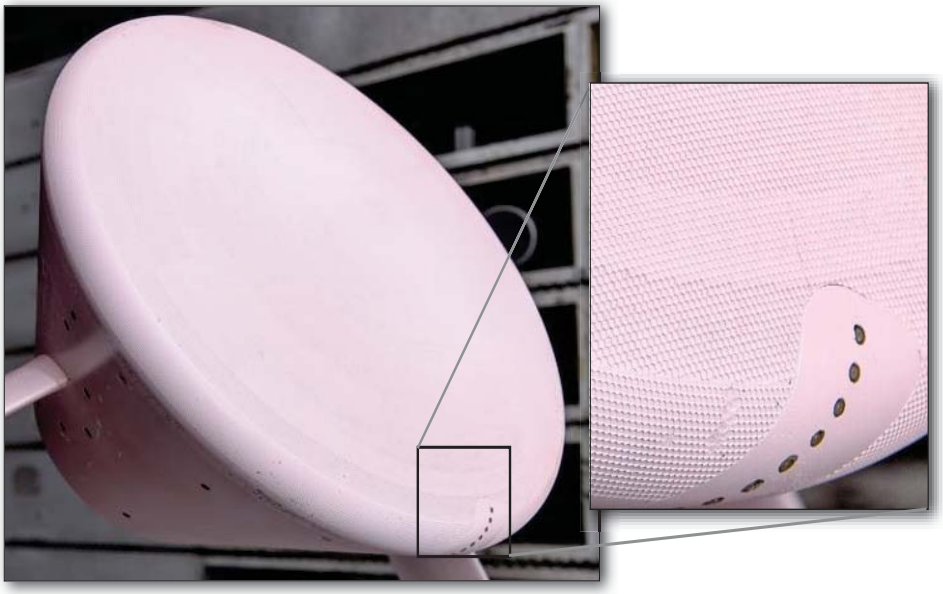

Figure 7.3-6. Rough Heatshield Surface

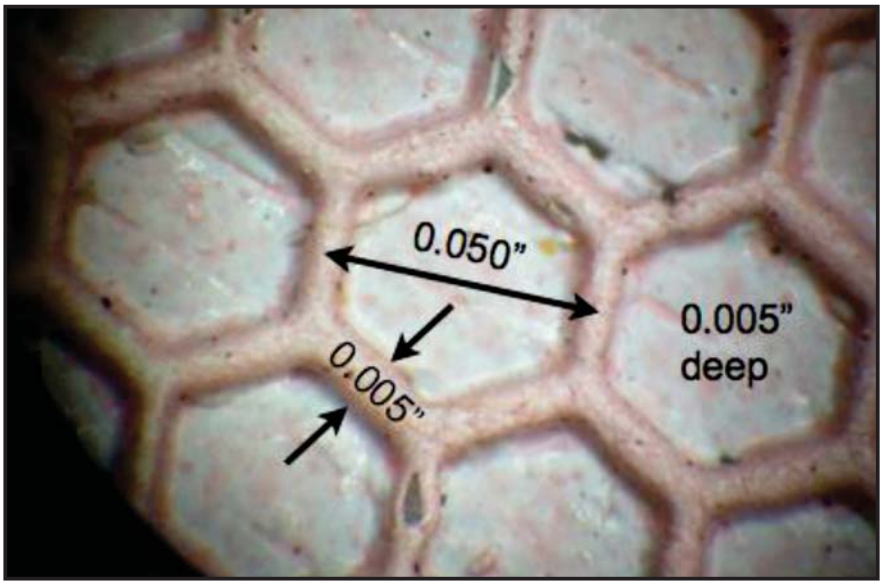

Figure 7.3-7. Dimples Machined into Rough Heatshield Surface

7.4 Instrumentation

7.4.1 Pressure Measurements

The CM model had 63 static pressure taps at the locations listed in Appendix A. These were primarily intended to check/calibrate the PSP results. Since PSP can be temperature sensitive, the various types of surfaces on the model needed to have taps to help correct for temperature effects. The pressure taps were arranged as shown in Figures 7.4-1 and 7.4-2. The static pressure taps were clustered in regions of large pressure gradients. There were taps on the back shell, pivot cover plates, and the flat end of the CM. These areas were expected to have different flow features and associated pressure distributions, but also had different materials and thicknesses. These differences could affect their temperature during the test, potentially affecting the PSP images/data.

The discrete static pressure measurements were acquired using a 15-pounds per square inch (psid), electronically-scanned pressure module (Pressure System, Inc. Model 64HD-0701021000) connected to the AUPWT data acquisition system. This module had 64 pressure transducers and the table of static pressure showed 65 static taps. Standard practice for using these kinds of pressure modules assigns 1 or 2 of the ports on a module to a known reference pressure, meaning that only 62 ports were available for test measurements. The difference is made up by disconnecting three of the back shell pressure taps and using them for the pressure measurements on the boundary layer survey when it was installed (see TAP ID 63-65 in Appendix A).

The unsteady pressure measurements were made using 44 Kulite® Semiconductor Products, Inc., model XCL-32-072-15D transducers. Forty of these transducers were installed in the four inserts described in Section 7.3. The sensor spiral arrangement around the heatshield shoulder was designed so no sensor was in the wake of another sensor. Four additional transducers were located on the back shell to provide information on the unsteady pressure field that might affect the MPCV pressure altimeter. The locations of the unsteady pressure transducers are shown in Figures 7.4-1 and 7.4-2.

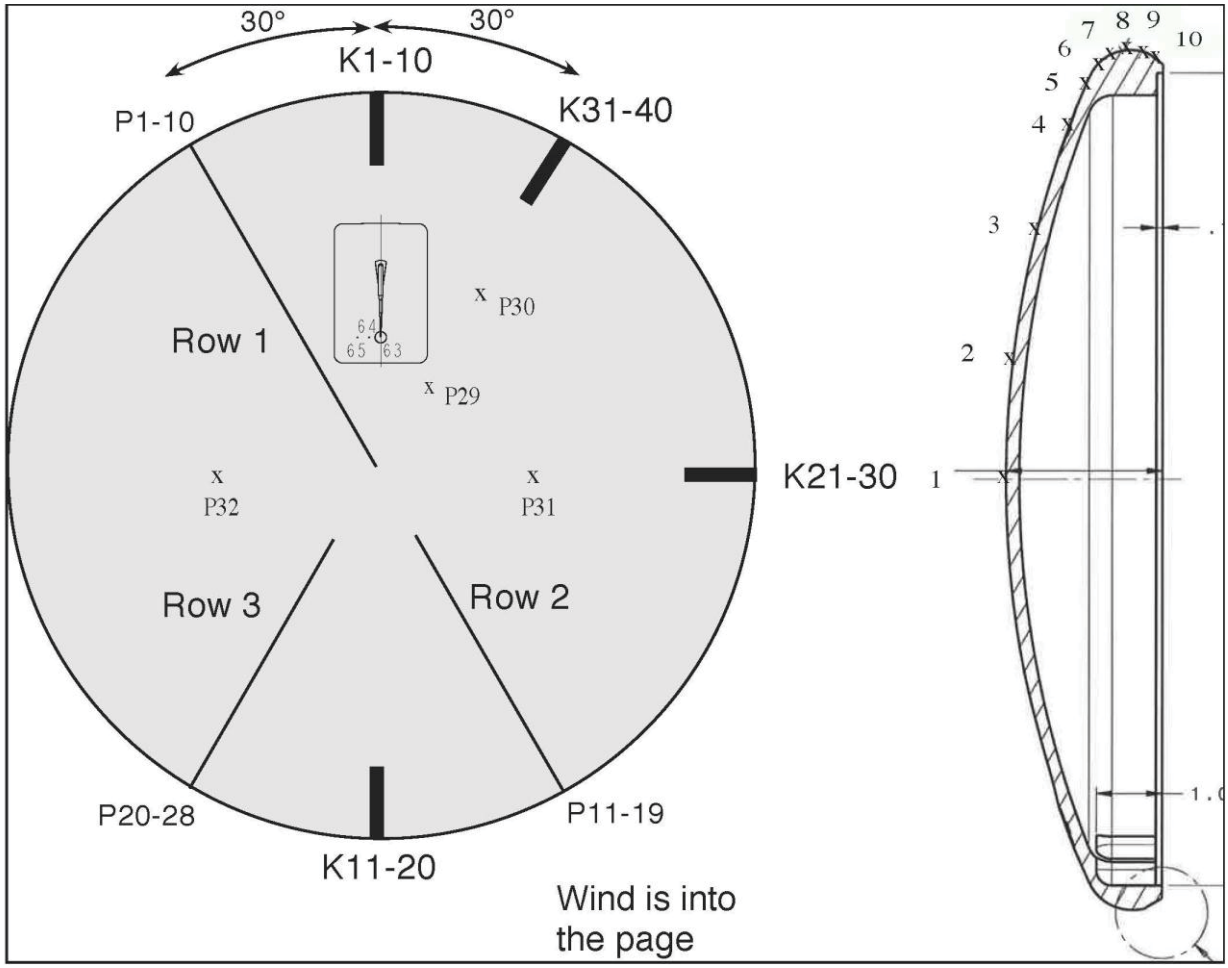

Figure 7.4-1. Pressure Tap Layout on the Heatshield, K1-K40 are Unsteady Transducers

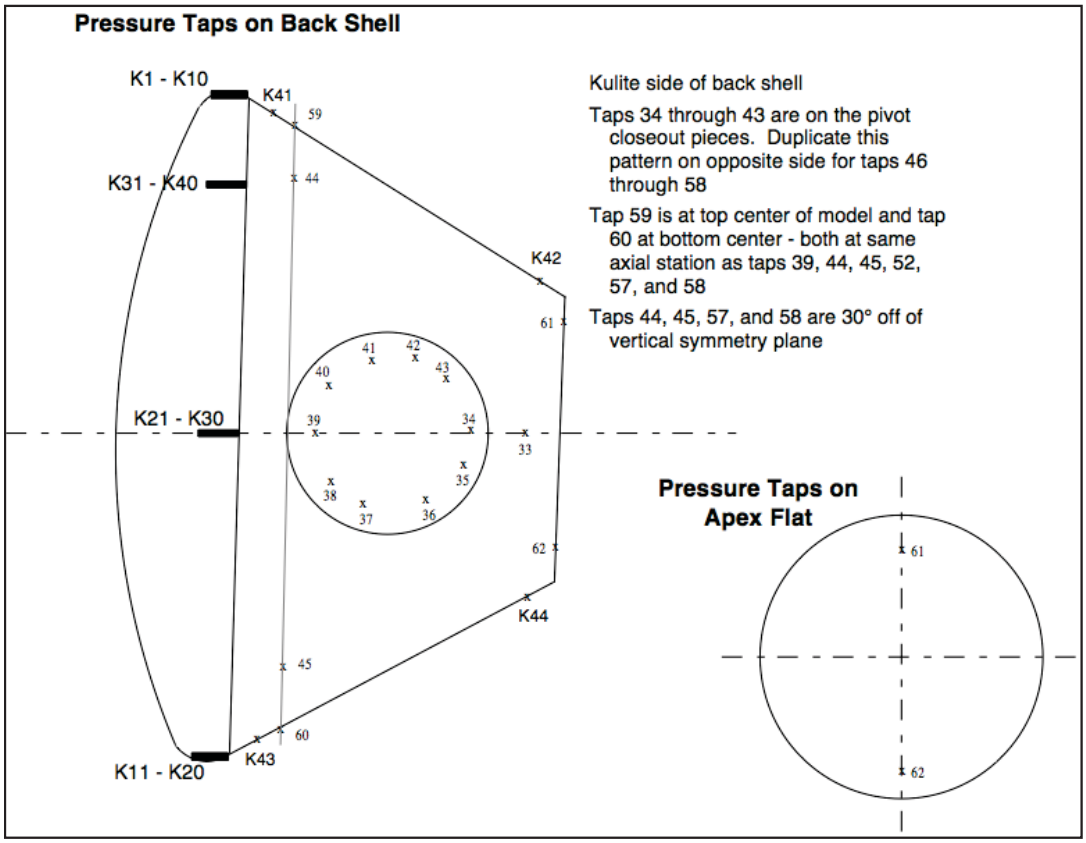

Figure 7.4-2. Pressure Tap Layout on the Heatshield and Back Shell, K1-K44 are Unsteady Transducers

The unsteady transducers were mounted in the model using custom-fit holders (Figure 7.4-3). The holders served two functions: to accurately set the distance between the sensor diaphragm and the model surface and to make it easier to remove and replace sensors in case of failure. The holder was inserted into a countersink in the model surface. The depth of the countersink was machined so all of the sensor diaphragms were set below the model surface (0.030 ±0.002 inch). The holder was machined to be flush to the model surface. The transducers were inserted from the inside of the model into the holder and then were bonded and sealed to the back side of the holder using a soluble glue (Duco™ cement). The locations of the unsteady pressure transducers are given in Appendix B.

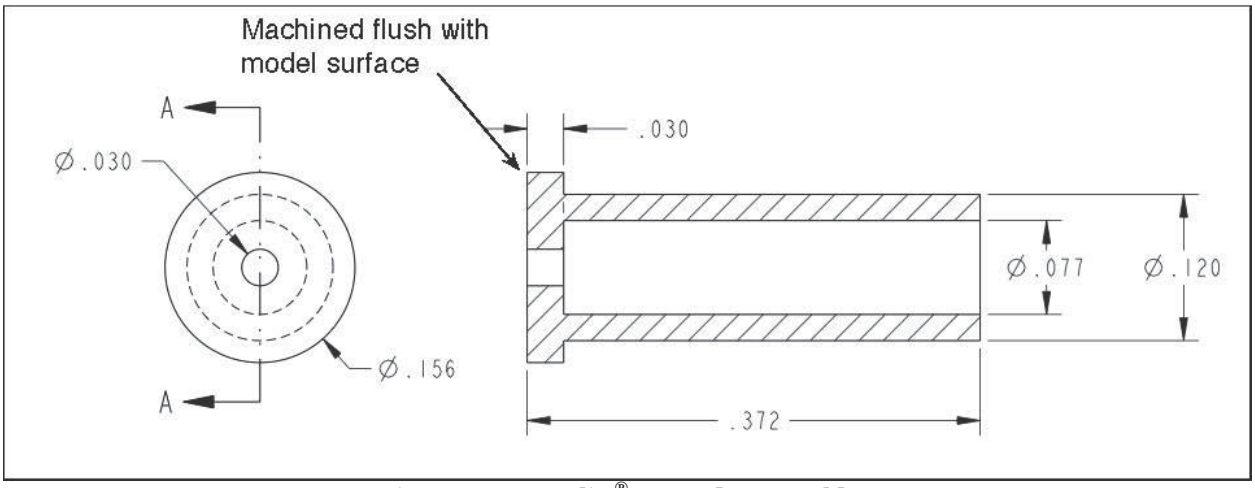

Figure 7.4-3. Kulite® Transducer Holder

7.4.2 PSP

PSP is a mature test technique commonly used in wind tunnels [ref. 8]. The main requirement for its use is good visibility of the model surfaces of interest for illumination and imaging. Multiple cameras were required to cover the model surfaces with acceptably small angles between the imaged surface and the camera view axis. The Vinci modeling program [refs. 9, 10] is used at ARC to plan camera and light placements and to estimate the resulting imaging quality.

Figure 7.4-4 shows the camera arrangement in the right-hand wall of the test section. The cameras and lighting for the various optical measurements need to be included in the Vinci modeling to ensure there is no imaging conflict (i.e., viewing or shadowgraph). The left-side of Figure 7.4-4 shows the PSP lighting quality. In Figure 7.4-5, the blue indicates good illumination and the red areas are approximately two f-stops lower in illumination. The right-side of Figure 7.4-5 shows the surface normal direction relative to the combined views of all the cameras. In this case, green indicates that at least one PSP camera has a view that is within 15 degrees of the surface normal. The darker areas in this image indicate ~60 degrees between the surface normal and the best camera view. These areas have lower data quality. The camera arrangement restricted these areas to relatively small portions of the struts, which were of lower importance to understanding the CM aerodynamics.

Eight Photometrics CoolSnap K4 2048-by 2048-pixel cameras with 7.4 micrometre (μm) pixel pitch were used for the PSP imaging while 15 400 nm light emitting diode lights from Innovative Scientific Solutions, Inc., were used for the illumination. The cameras and lamps were located in both sidewalls, the floor, and ceiling of the test section. Some of the windows for the cameras and lights are shown in Figure 7.2-1.

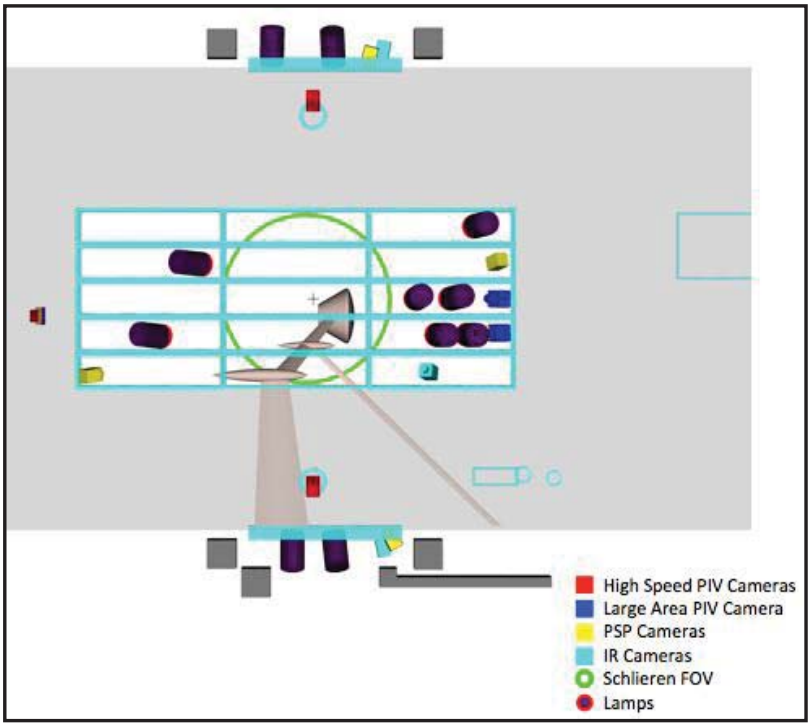

Figure 7.4-4. Layout of Cameras and Lights around Test Section in Vinci Modeling Tool (view of right-hand wall; wind is right to left)

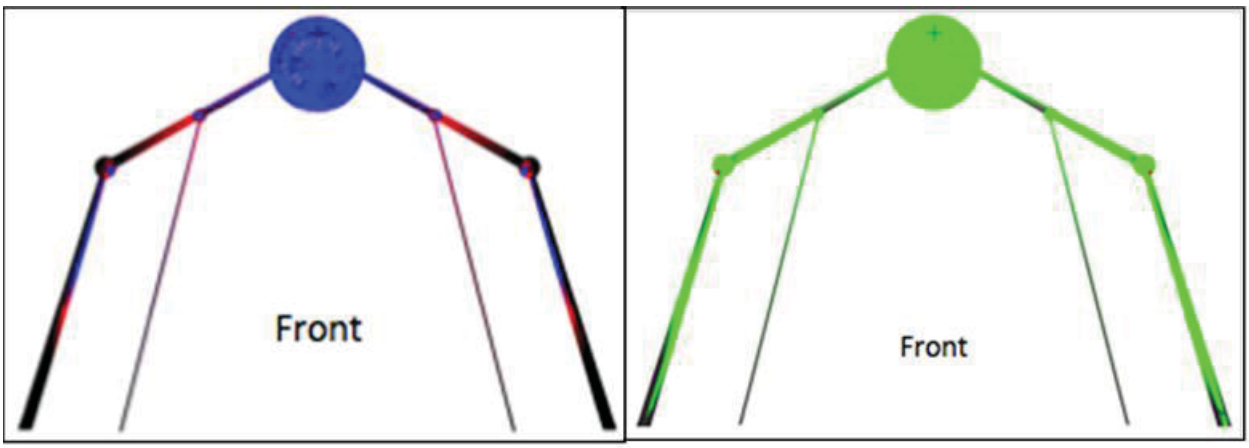

Figure 7.4-5. Illumination quality (left) and Camera View Angle Relative to Surface Normal (right) for PSP Cameras

Note: In left figure, blue indicates good illumination and red is two f-stops lower; in right figure, green indicates surface normal within 15 degrees of at least one camera axis.

7.4.3 Boundary Layer Measurements

A boundary layer traverse mechanism was installed in the model for a portion of the test. When not installed, the mechanism was replaced by a blank plate machined (and textured) to match the heatshield. The traverse insert is shown in Figure 7.4-6. Figure 7.4-7 shows the total pressure probe driven by a Zaber Technologies T-NA08A25 stepper motor and TSB28M translation stage. The probe tip geometry allowed total pressure measurements to 0.0049 inch above the surface and the traverse had approximately 1 inch of travel. The traversing mechanism and overall construction of the insert are shown in Figure 7.4-7.

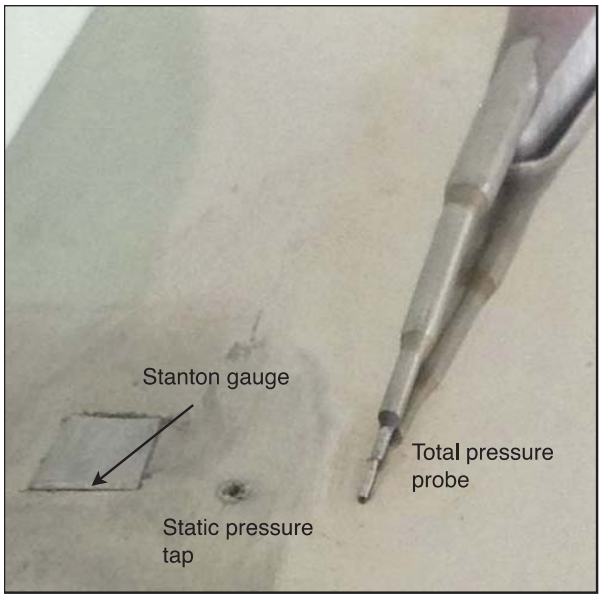

Figure 7.4-6. Traversing Boundary Layer Total-Pressure Probe, Stanton Gauge, and Static Pressure Tap

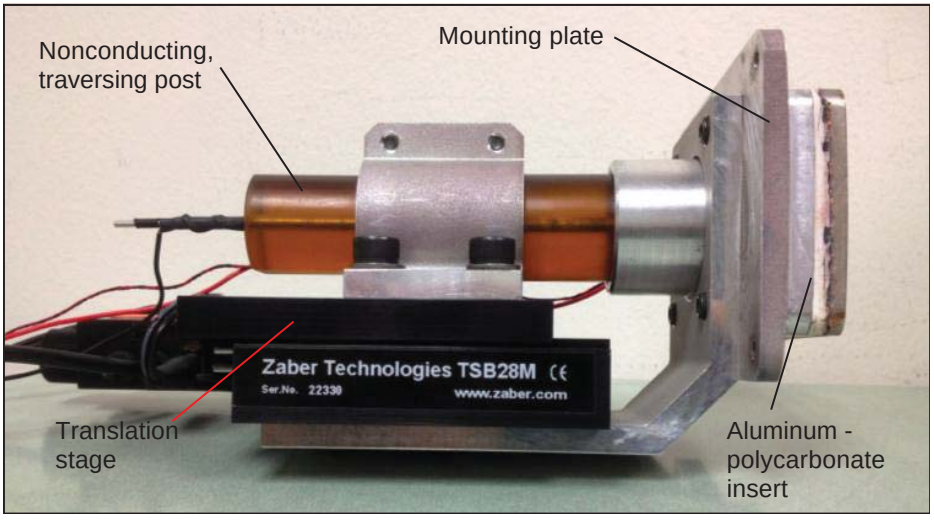

Figure 7.4-7. Boundary Layer Insert

The boundary layer traverse insert was made of the same materials as the rest of the heatshields (i.e., an aluminum base plate with 0.25 inches of bonded polycarbonate). The insert was machined flush with the smooth heatshield to ensure minimal flow disturbance. Blank plates of aluminum/polycarbonate laminate were machined to replace the insert for most of the test series. Separate blanking plates were made for the smooth and rough heatshields with the appropriate surface texture. The outer surface of the traverse insert was nickel-plated to provide a smooth, reflective surface for the oil-film interferometry (OFI) measurement of the skin friction. OFI is an established measurement technique that is minimally intrusive [refs. 1, 12]. Adjacent to the probe were a static pressure tap and a Stanton gauge (Figure 7.4-6) used to measure the skin friction [refs. 13, 14, 15]. The Stanton gauge was calibrated against the OFI skin friction measurements, which were only obtained at a few test conditions due to the time required for accurate OFI measurements. The machining and nickel-plating process left the tap recessed below the surrounding surface. This recession was filled with cyanoacrylate glue, sanded smooth, and the tap hole re-drilled.

An image of the insert installed in the rough heatshield is shown in Figure 7.4-8. The black fiducial marks around the insert were measured precisely on the model using a portable FaroArm™ coordinate measuring machine. These marks were used to calibrate the OFI images. OFI skin-friction measurements depend on accurate determination of the spacing of fringes generated by a sheared layer of oil.

Figure 7.4-8. Boundary Layer Insert Mounted in Rough Heatshield

7.4.4 Mounting Strut Strain Gauges

The upper mounting struts were strain gauged for bending to monitor the aerodynamic loads acting on the model during the test. This was primarily to ensure safety. Full-bridge gauges were located on both upper struts, upper and lower surfaces, near the junction with the lower struts, and on the model side of the cable attachment fairing. Figure 7.4-9 shows the strain gauge locations on the left upper strut. The flat ribbon cables from the gauges adjacent to the cable attachments run along the upper strut trailing edge to the junction with the lower struts. The cables run into the main cable bore in the lower struts where the rest of the instrumentation cables were located.

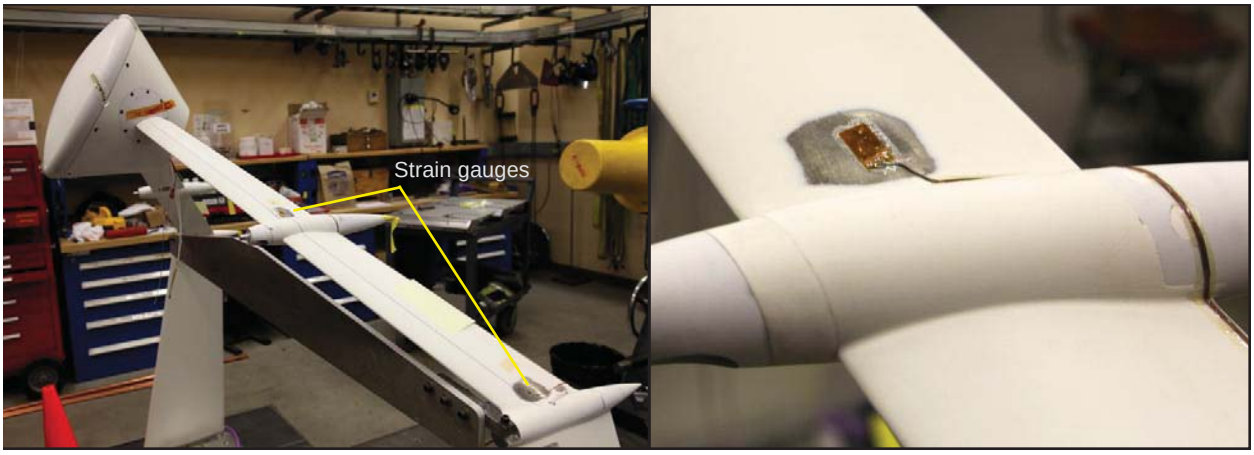

Figure 7.4-9. Strain Gauges on Left Upper Strut

7.4.5 Additional On-Board Instrumentation

In addition to the electronically-scanned pressure module, an AoA sensor and a high-rate, 3-axis accelerometer were mounted inside the CM model. The AoA was measured using a Honeywell QA2000 accelerometer, which was mounted to the back shell in the machined pocket at the bottom in the CAD view as shown in Figure 7.3-3. An Omega® model ACC301 3-axis accelerometer was used to monitor model vibrations, primarily as a diagnostic tool in case the model vibrations were larger than expected. The vibration data was recorded with the unsteady pressure signals.

7.4.6 IR Thermography

Three IR cameras were used to image the temperature variation over the model from which a variety of flow features could be discerned. Two FLIR™ model 6800 cameras and a model 7800 camera were used for the IR imaging. Germanium windows were mounted in the wind tunnel wall, floor, and ceiling to provide the necessary optical access (i.e., two existing window locations and one new window location). Vinci [refs. 9, 10] was used to optimize the camera and the new window locations and to eliminate potential conflicts with other cameras and lighting for PSP, PIV, and shadowgraphy. The IR images were stored in the FLIR™ examiner software format as individual tiff or jpeg images, enhanced for specific flow features.

7.4.7 High-Speed Shadowgraph Imaging

The wind tunnel shadowgraph system was used to image the flow during the test. The frames were acquired at a rate of 6,000 per second using a Photron SA1 1024x1024 pixel camera with a 20 μm pitch. At every test condition, 80 individual images were acquired. The 80 images were made into a movie and a single, averaged image showing the mean flow structure.

7.4.8 PIV Measurements

The use of PIV for flow measurements has been well-established in laboratories and wind tunnels [ref. 16]. PIV system installation is more problematic in larger wind tunnels, particularly pressurized wind tunnels where optical access is not straightforward. The measurement plane location can increase the installation difficulty. For this experiment, there were two planes of interest: a horizontal cross-stream plane with a relatively small imaging area to look at the details of the wake shedding near the model, and a stream-wise vertical plane through the center of the wake with a large imaging area. The velocity in the smaller plane near the model was measured at a rate of 2,000 measurements per second. The velocity in the larger, vertical plane was measured at a rate of 2 measurements per second. These two PIV systems are referred to as the high-speed and wide-view systems, respectively. For both systems, the goal was to acquire at least 2,000 samples for each test condition. The number of samples was chosen to ensure convergence of the turbulence statistics on the high-speed system.

The laser sheet for the wide-view system required installation of several optical elements inside the plenum. Figure 7.4-10 shows the laser path and the location of the optics required to form the vertical sheet at the center of the test section. The mirrors in the flow downstream of the slotted walls, on the sidewall, and on the vertical strut required careful design and installation to minimize vibrations. Vibration of those mirrors causes large motions of the laser sheet because of the distance from the mirrors to the image area. Custom enclosures were built to house these mirrors and to protect them from the airflow and contamination from the PIV seed material (i.e., atomized mineral oil). Figure 7.4-11 shows laser sheets for the wide-view and high-speed PIV systems. The final mirror in the wide-view laser delivery system was mounted to the vertical strut downstream of the test section.

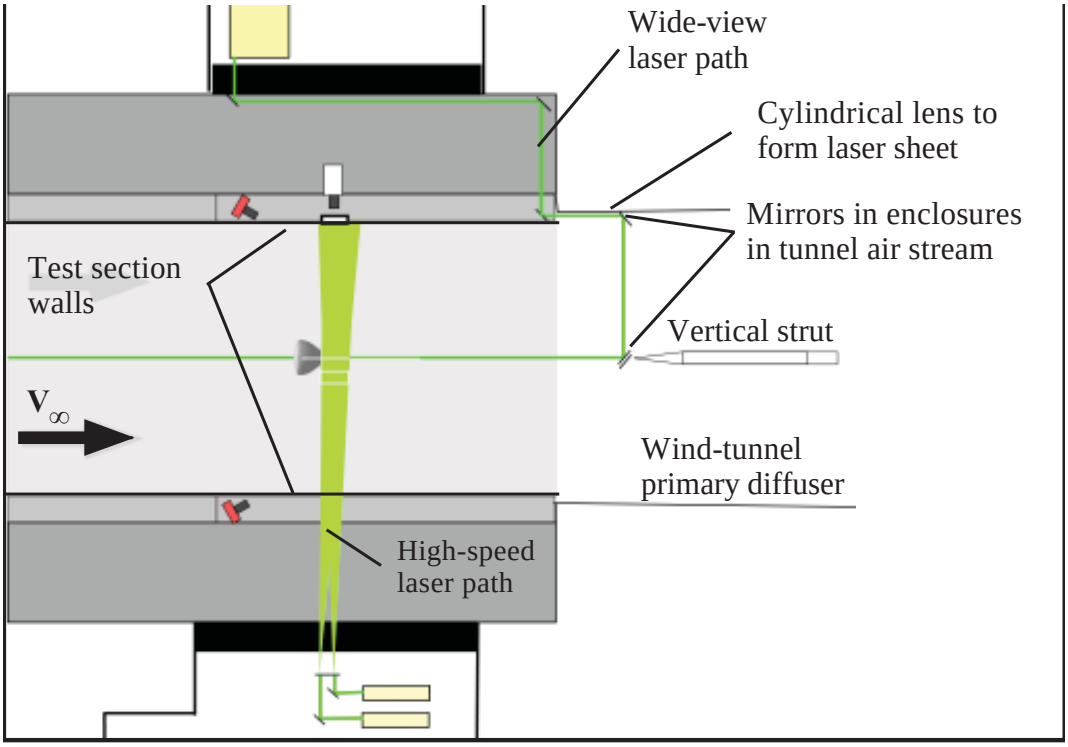

Figure 7.4-10. Laser Sheet Paths in 11x11-ft Test Section

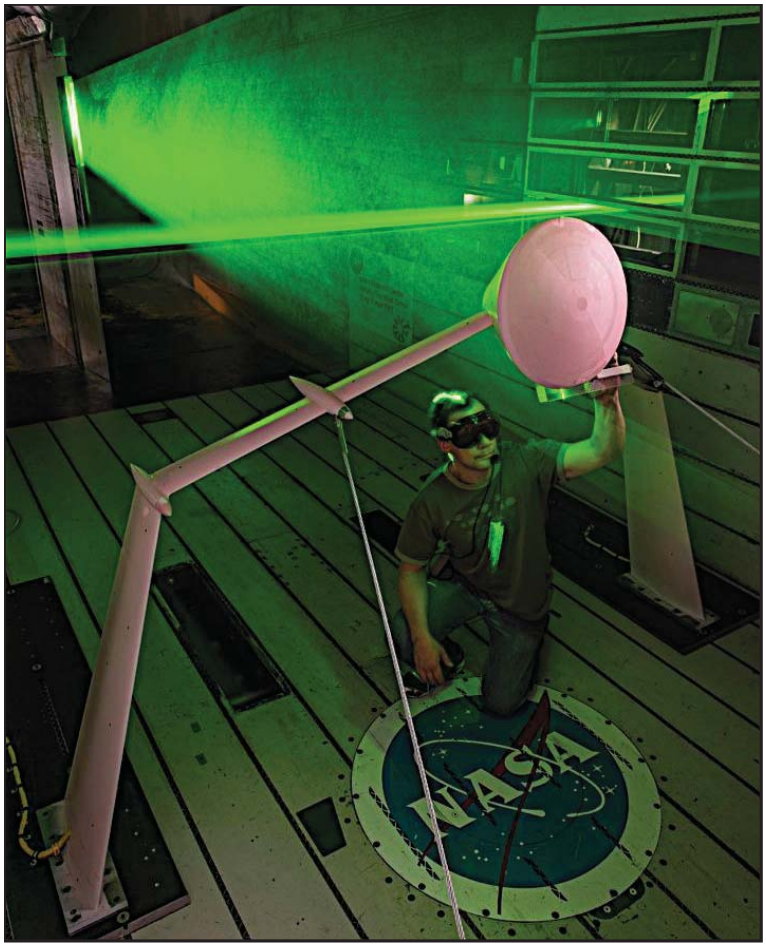

Figure 7.4-11. PIV Laser Sheets

The horizontal laser sheet in Figure 7.4-12 was for the high-speed system. It entered the plenum through the opposite window from where the wide-view laser entered (i.e., right-side of the image in Figure 7.4-11). This sheet traveled through the plenum and across the test section into a beam dump to minimize stray reflections.

The locations of the PIV measurement areas for both systems and model locations are shown in Figure 7.4-12. The greyed-out areas of the wide-view image areas were contaminated by laser reflections on the wind tunnel wall, which eliminated the ability to compute the flow velocity in that area.

The wide-view PIV image area was captured by two Redlake EC11000 cameras with 4008x2672 pixels and 9 μm pixel pitch. The object space resolution was ~4 pixels per millimeter. The laser sheet was generated by a Spectra-Physics PIV 400 laser tuned to deliver 400 mJ/pulse.

PIV data acquisition and processing was performed using La Vision DaVis versions 7.4 and 8.1.4, respectively. The processing parameters included a 6-pixel high-pass filter, multi-pass correlation using 256 pixel windows initially, then finishing with 128x128 pixel, Gaussian-weighted windows with 75 percent overlap. This window size was chosen because of the low signal-to-noise ratio of the images. The turbulence statistics did not converge when the data was processed on smaller windows. The resulting measurement grid was 262 by 154 points in the x- and z-directions, respectively. Each vector was measured in a time window of ~32 milliseconds. The window deformation scheme interpolates and adjusts the vectors to capture gradients smaller than an interrogation window.

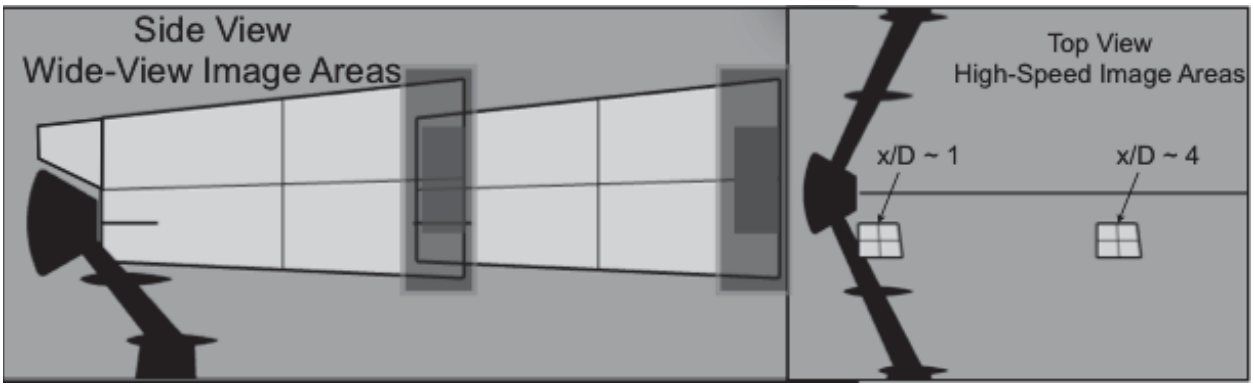

Figure 7.4-12. PIV Imaging Areas for Both Model Positions

The high-speed PIV data were acquired using Phantom 641 cameras with a sensor resolution of 2560x1600 pixels and a pixel pitch of 10µm. The images were captured using only 2000x600 pixels in order to achieve the 4,000 frames/second imaging required for 2,000 velocity measurements per second. The laser sheet was generated using two Quantronix Darwin Duo lasers providing 40 mJ/pulse.

As with the wide-view measurements, La Vision DaVis software was used for data acquisition and processing. The high-speed data were processed using a 6-pixel high-pass filter, correlated with the multi-pass scheme starting with 64x64 pixel windows, and reduced to 32x32 pixel Gaussian-weighted windows with 75 percent overlap. The resulting measurement grid was 257x132 points in the x- and y-directions, respectively.

For both PIV systems, the instantaneous velocity measurements were archived with the velocity statistics. A summary of the computed statistical information is given in Table 7.4-1.

Table 7.4-1. Flow Statistics in Archived PIV Data Files

File Name	Derived Flow Variable, High-Speed Data	Derived Flow Variable, Wide-View Data
B00001.dat	Average V_x	Average V_x
B00002.dat	Average V_y	Average V_y
B00003.dat	Average V_z	Average V_z
B00004.dat	Average Kinetic Entergy	rms V_x
B00005.dat	rms V_x	rms V_y
B00006.dat	rms V_y	rms V_z
B00007.dat	rms V_z	Turbulent Kinetic Energy
B00008.dat	Turbulent Kinetic Energy	Reynolds Stress, xy
B00009.dat	Reynolds Stress, xy	Reynolds Stress, xz
B00010.dat	Reynolds Stress, xz	Reynolds Stress, yz
B00011.dat	Reynolds Stress, yz	Reynolds Stress, xx
B00012.dat	Reynolds Stress, xx	Reynolds Stress, yy
B00013.dat	Reynolds Stress, yy	Reynolds Stress, zz
B00014.dat	Reynolds Stress, zz	2D Max Turbulent Shear Stress
B00015.dat	2D Max Turbulent Shear Stress	-

8.0 Test Conduct

The test was run over a 3-week period from August 20, 2012, to September 6, 2012. An additional 3 weeks was spent in the model preparation room prior to installing the test article in the wind tunnel. Table 8.0-1 shows the runs accomplished during the test. The highest priority was to acquire all data at Mach 0.7 and 15-degree AoA, which represented close to the nominal drogue parachute deployment conditions.

Table 8.0-1. List of Runs Accomplished During Test

CM Wake Characterization Study						Mach Number									
Purpose	XCM/D	YCM/D	α	Re (M/ft)	FISM	0.30	0.50	0.70	0.90	0.95	1.05	1.10	1.05 + or -	1.30	1.40
PSP, IR, and Kulites															
PSP, IR, and Kulites			Rough HS			Block pri 1 hours		5.8					Block pri 1 runs		0
Static and unsteady pressures + IR	0.0	0.0	30	1	N	3	3	36, 42	3	3	3	3	43	3	3
				7.5		44	45	46	47	3	3	3	48	3	3
			15	1		3	3	3	3	3	3	3	3	3	3
				7.5		54	55	56	57	3	3	3	58	3	3
			0	1		3	3	3	3	3	3	3	3	3	3
				7.5		3	3	3	3	3	3	3	3	3	3
PSP - repeats			Block Repeats	#DIV/0!		Block repeat hours		0.0					Block pri 1 runs		0.0
	0.0	0.0	30	1	N	3	3	3	3	3	3	3	3	3	3
Static and unsteady pressures + IR				7.5		3	3	60	3	3	3	3	3	3	3
PSP, IR, and Kulites			Smooth heat shield			Block pri 1 hours		1.8					Block pri 1 runs		0
Static and unsteady pressures + IR	0.0	0.0	30	1	N	3	3	69	3	3	3	3	70	3	3
				7.5		71	72	73	74	3	3	3	75	3	3
			15	1		3	3	3	3	3	3	3	3	3	3
				7.5		3	3	3	3	3	3	3	3	3	3
			0	1		3	3	3	3	3	3	3	3	3	3
				7.5		3	3	3	3	3	3	3	3	3	3
PSP - repeats			Block Repeats	#DIV/0!		Block repeat hours		0.0					Block pri 1 runs		0.0
	0.0	0.0	30	1	N	3	3	3	3	3	3	3	3	3	3
Static and unsteady pressures + IR				7.5		3	76	3	3	3	3	3	3	3	3
															PSP/IR Runs/H
BL Survey - With rough HS			Rough HS			Block pri 1 hours		2.5					Block pri 1 runs		0
Boundary layer survey	0.0	0.0	15	7.5	Y	98 - 100	3	101,102	3	3	3	3	103 - 105	3	3
Boundary layer survey			15	7.5	N	3	3	3	3	3	3	3	3	3	3
Boundary layer survey			30	7.5	N	107,108	3	109,110	3	3	3	3	111 - 113	3	3
Boundary layer survey			30	1	N	3	3	3	3	3	3	3	3	3	3
Boundary layer survey			0	7.5	N	115 - 118	119 - 121	122 - 123	3	3	3	3	3	3	3
															BL Survey Runs/H
PIV, Kulites, and Schieren															
PIV and Kulites			Rough HS			Block pri 1 hours		5.0					Block pri 1 runs		0
PIV - Rough HS	0.0		15	7.5	N	126, 129 132, 135	136, 138	139, 141, 142	3	3	3	3	143	3	3
			30	7.5		3	3	3	3	3	3	3	3	3	3
			0	7.5		3	3	3	3	3	3	3	3	3	3
PIV repeats			Block Repeats	#DIV/0!		Block repeat hours		0.0					Block pri 1 runs		0.0
PIV- rough			30	7.5		3	3	3	3	3	3	3	3	3	3
PIV and Kulites			Smooth			Block pri 1 hours		3.0					Block pri 1 runs		0
PIV and Kulites at X/D = -3.0			Rough HS			Block pri 1 hours		5.0					Block pri 1 runs		0
PIV - Rough HS	-3.00	0.00	15	7.5	N	150	147, 151	146, 153	3	3	3	3	3	3	3
PIV - Rough HS			30	7.5		3	3	3	3	3	3	3	3	3	3
PIV - Rough HS			0	7.5		3	3	3	3	3	3	3	3	3	3
PIV and Kulites at X/D = -3.0			Smooth HS			Block pri 1 hours		3.0					Block pri 1 runs		0

The test was divided into three phases. The first was to acquire PSP, IR, and unsteady pressure data with the rough and smooth heatshields. The original plan was to acquire those data types for AoA of 0, 15, and 30 degrees. The rough heatshield at 30 degrees AoA was tested first because previous testing of the Orion CM showed the flow was the most unsteady at 0 degrees AoA with a smooth (un-tripped) heatshield. The load limits of the test (monitored using the strain gauges on the upper struts) made it uncertain whether the team could test at 0 degrees AoA. Ultimately, time constraints on PIV lighting borrowed from the Air Force's Arnold

Engineering and Development Center, and other aspects of the test (e.g., primarily installation and calibrating the strain gauges for aero loading) prevented completion of the planned test matrix for this test portion and no data was acquired for 0 degrees AoA with either heatshield. Testing of the smooth heatshield was only performed at 30 degrees AoA because of the same resource constraints.

This portion of the test was run mostly at high Reynolds number that varied with Mach number, but some runs were done at lower Reynolds numbers, primarily to check out the model at lower dynamic pressure. These data proved to be instructive as described in the results section.

The second test phase was relatively short and examined the heatshield boundary layer. With the boundary layer insert installed in the model, the NESC team did not acquire other data types except for IR imagery. Only the rough heatshield was tested and only at the high Reynolds number conditions. However, some data was acquired at a 0 degree AoA for Mach numbers of 0.3, 0.5, and 0.7.

In the third test phase, the PIV measurements took the longest to prepare and run. Throughout the first two portions of the test, refinements were made to the PIV system. Camera operation was checked out and laser sheet optics were adjusted on the off-shift to minimize the impact on the other portions of the test. Keeping the PIV hardware operating and in alignment proved to be more challenging than anticipated, which limited the conditions for which PIV data was acquired. The NESC team limited this portion of the test to only the rough heatshield and 15 degrees AoA. For the initial model installation, near wake measurements, data was acquired at Mach numbers of 0.3, 0.5, and 0.7. The Mach 0.9 condition was not tested because it generated the most unsteady flow and vibration caused PIV system alignment issues. No data were obtained at Mach 1.03 since the seeding was poorly distributed across the test section because of the plenum evacuation required to reach supersonic conditions. For the second model position, far wake measurements, data was acquired at Mach numbers of 0.3, 0.5, and 0.7.

The first two test phases acquired data for approximately half of the planned test conditions. The main omission was the 0 degree AoA conditions. The smooth heatshield data, as will be discussed, was contaminated by premature transition caused by surface flaws, so additional data would not have been helpful. However, the data acquired were instructive concerning the sensitivity of the boundary layer transition to the smoothness of the model surface.

The PIV portion of the test was less successful in covering the planned test conditions. Only about 25 percent of the planned measurements were acquired. Given the lower-than-planned productivity, the data acquired was of good quality and covered the flight conditions for drogue deployment to a location in the wake close to the drogue parachute location (i.e., 5.5 versus 7 diameters for the drogue parachutes).

The following sections describe the results obtained from the various measurement techniques. In most cases, representative samples of the data are presented. The archived data is described in Appendices C through H, with Appendix C describing the files containing the test conditions and

static pressure data. The complete data set is available on the test website on aeroCOMPASS. The data can be made available on hard disk.

8.1 IR Thermography

The IR thermography worked well during the test providing details of boundary layer transition and flow separation. The images showed the suction peak on the heatshield as an area of cooler surface temperature, which had not been previously visualized in the AUPWT. The IR data was archived as tiff or jpg images of individual runs from the three IR camera views, and as FLIR™ proprietary files that contain a few seconds of IR video that can be interrogated using FLIR™ ExaminIR™ software. Appendix C provides a description of the archived IR images.

8.1.1 Rough Heatshield IR

Figure 8.1-1 shows an example of an IR image taken at M 0.7, 30 degrees AoA, and Reynolds number $10x10^6$. This image covers a temperature range that shows the flow details around the heatshield shoulder so the stagnation point indicated is not shown. The attached, accelerating flow gradually decreases in temperature as the flow accelerates approaching the shoulder. The much cooler flow at the maximum velocity region (i.e., lowest pressure or maximum suction) is visible as a dark line in the image. The dark line (i.e., ring around the model) is followed by a lighter area showing the flow slows after the suction peak. The separation line is apparent as an abrupt decrease in temperature, shown as the black area at the beginning of the back shell (but still part of the heatshield model part with the plastic overlay) in the image. The aluminum back shell was at a different temperature during the testing and the joint between the model materials shows up as an abrupt increase in temperature. The plastic fairings over the model strut attachment points had a temperature similar to the post-separation heatshield as shown by the dark circle around the strut penetrations through the back shell. The transition strips that were applied to the support struts (e.g., lower surface of the left-hand strut) are visible. The separated shear layer can be seen passing over the right-hand upper strut as a bright band with darker (i.e., colder) temperature on the strut further toward the model.

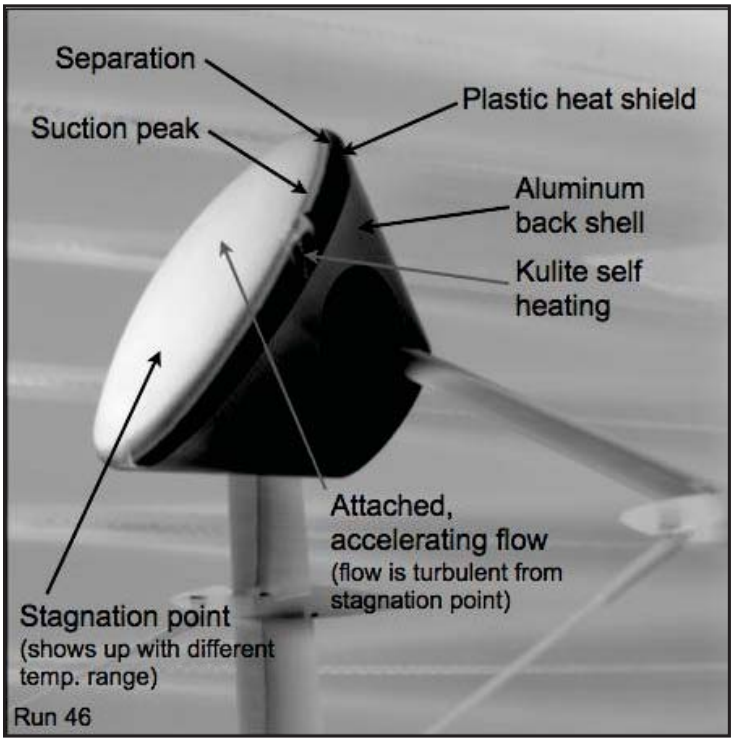

Figure 8.1-1. IR Image of the Rough Heatshield at Mach 0.7, AoA 30 degrees, and Reynolds Number 10^7

An unexpected result was the ability to see the individual Kulite® pressure transducers. The transducers generate a small amount of heat when energized which makes them visible as light dots. The IR images with the Kulites® turned off and the overall flow patterns were unchanged so for most of the test the sensors were left energized.

Figure 8.1-2 shows a comparison between the pressure distribution and the temperature distribution on the model at Mach 0.3, 15 degrees AoA, and Reynolds number 5.3×10^6. The two images show the same flow patterns. The IR and PSP show the stagnation point and suction peak while the IR image shows the separation point more clearly than the PSP. The local flow disturbances caused by the Kulite® inserts shows more clearly in the IR image.

Changes in flow patterns with Mach number are shown in Figure 8.1-3. The images were scaled to a temperature range highlighting the flow at the heatshield perimeter. The differences are subtle with the largest effect being the diminishing disturbance to the flow by the Kulite® inserts with increasing Reynolds number. There is an abrupt change in the extent of the cooler suction peak band and an upstream shift in the separation line as Mach number increases from 0.7 to 0.9. This is likely due to the formation of a shock at the higher Mach numbers, which tends to force the separation location. There will be more discussion of this effect in the sections on the unsteady pressure measurements and Schlieren/shadowgraph images.

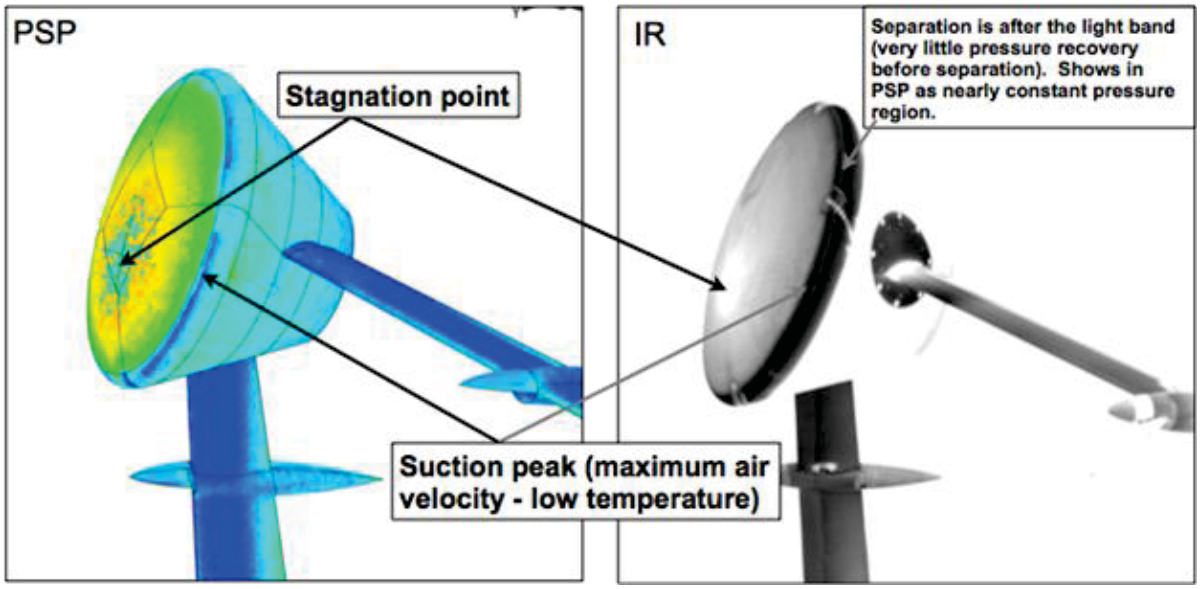

Figure 8.1-2. PSP Image Compared to IR Image with Temperature Range to Show Stagnation Point; Rough Heatshield at Mach 0.3, AoA of 15 degrees, and Reynolds Number 5.3x10^6

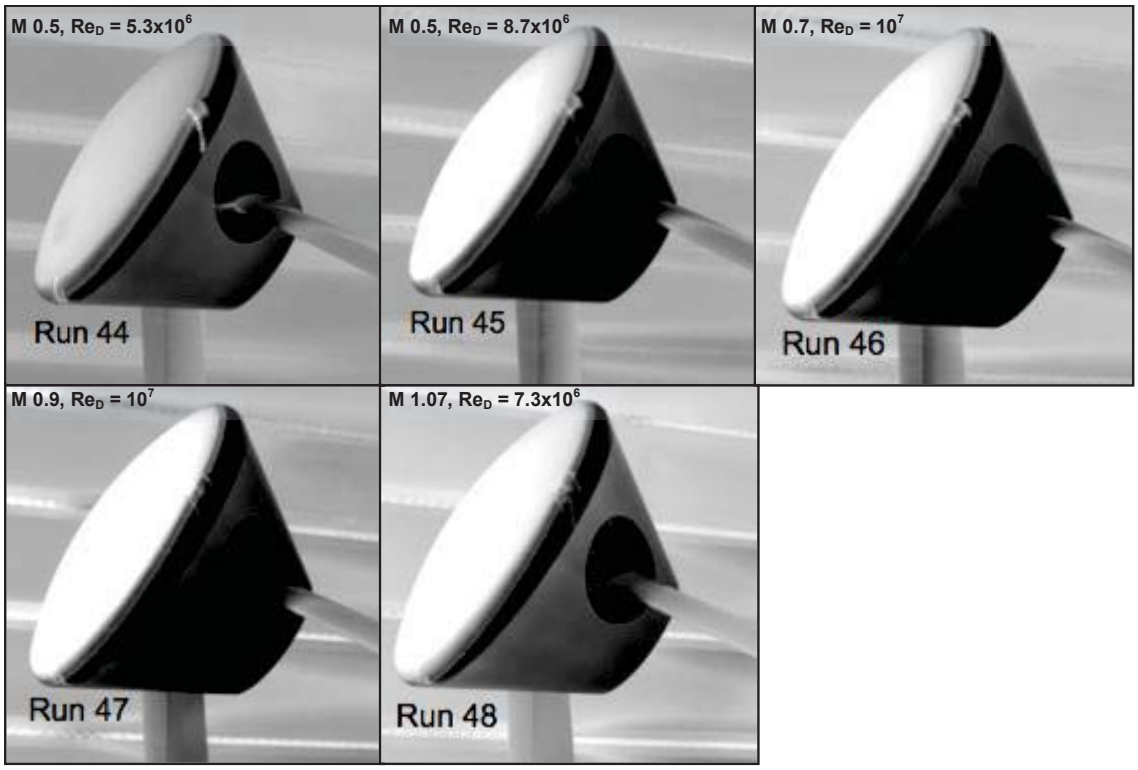

Figure 8.1-3. IR Image Showing Changes in Flow Structure with Increasing Mach Number

8.1.2 Effect of Reynolds Number on Rough Heatshield

Given the roughness pattern that was machined into the plastic heatshield surface, it was assumed the boundary layer would transition to turbulent near the stagnation point. The IR images obtained at the lower Reynolds number (i.e., $1.33x10^6$) were surprising. Figure 8.1-4 shows IR images for two runs at the same test conditions (i.e., Mach 0.5 and AoA 30 degrees). The dark to light patterns are nearly identical for the two runs performed several hours apart. The patterns do not correspond to any physical pattern on the rough heatshield. There were variations in the depth of the hex pattern on various parts of the heatshield, particularly nearer the stagnation point for this test condition. The note in Figure 8.1-4 points to a seam in the hex pattern. To the right of the seam, the depth of the pattern is less than the depth to the left of the seam. Figure 8.1-5 shows the difference in roughness depth across the seam at the opposite end of the seam. The IR cameras could see the difference in the hex-pattern depth as a difference in temperature. It was not clear whether the resulting dark-light (i.e., colder-warmer) pattern in the IR images were a result of a bias in transition location due to the roughness difference, particularly with the expectation of fully, or nearly so, turbulent flow on the rough heatshield. There was a small area of the model where the PSP did not stick to the rough heatshield that is visible in Figure 8.1-5. This may be an area where some residual machining lubricant (detergent) was left on the surface preventing good adhesion of the base coat of paint.

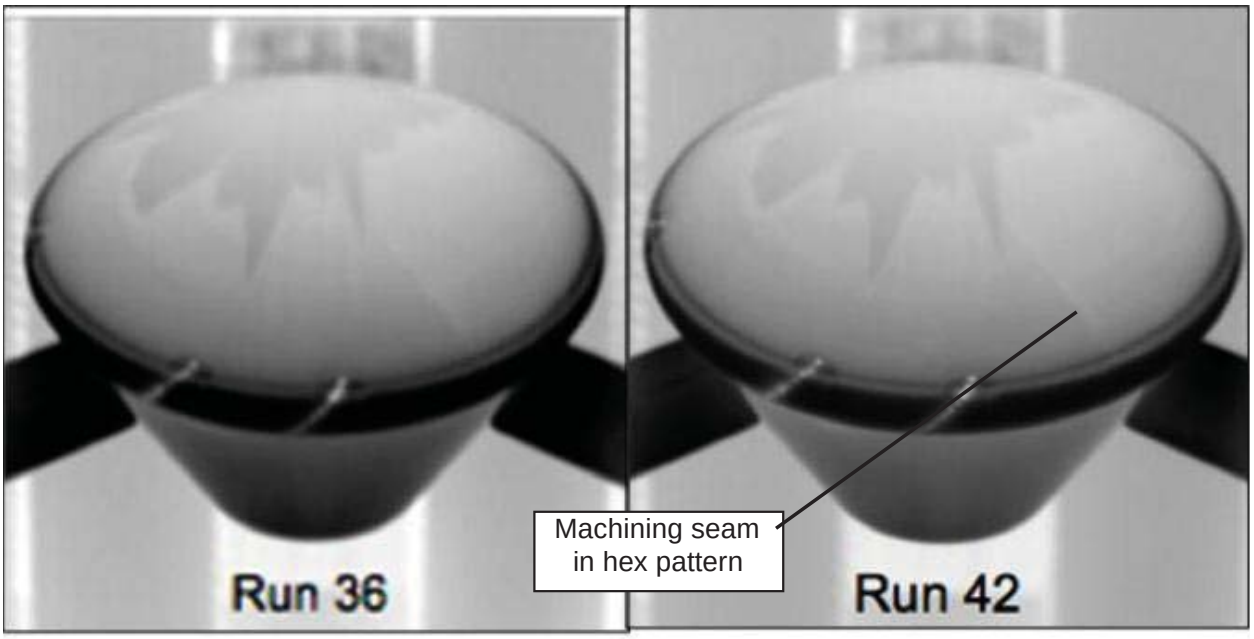

Figure 8.1-4. IR Images of Heatshield taken with the Ceiling Mounted Camera at Mach 0.5, AoA of 30 degrees, and Reynolds Number $1.33x10^6$

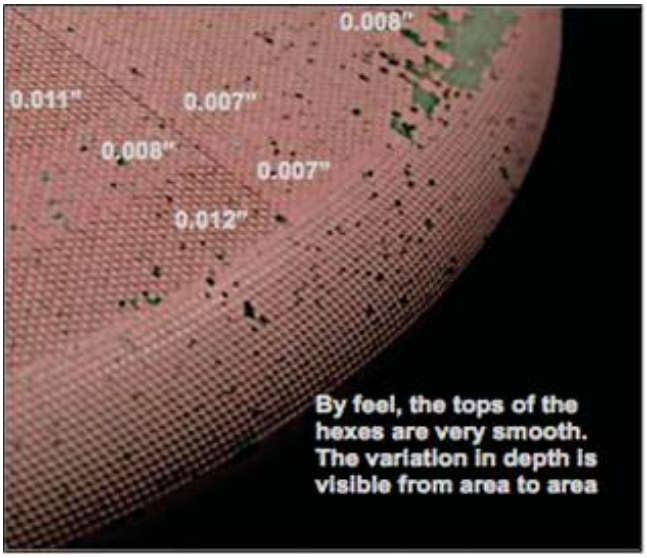

Figure 8.1-5. Difference in Roughness Depth Across Machining Seam
Note: dimensions in inches.

8.1.3 Smooth Heatshield

The smooth heatshield at low Reynolds number showed a complicated pattern of transition that was nearly always traceable to a surface defect. Figure 8.1-6 shows a top-view IR image of the smooth heatshield at Mach 0.7. Laminar flow is present where the temperature is lower (i.e., darker) with turbulent flow in the warmer (i.e., lighter) areas. Figure 8.1-7 shows the same test point taken with the side-view camera. Both images show that where the boundary layer remains laminar to the shoulder, the flow separates immediately downstream of the suction peak with little pressure recovery.

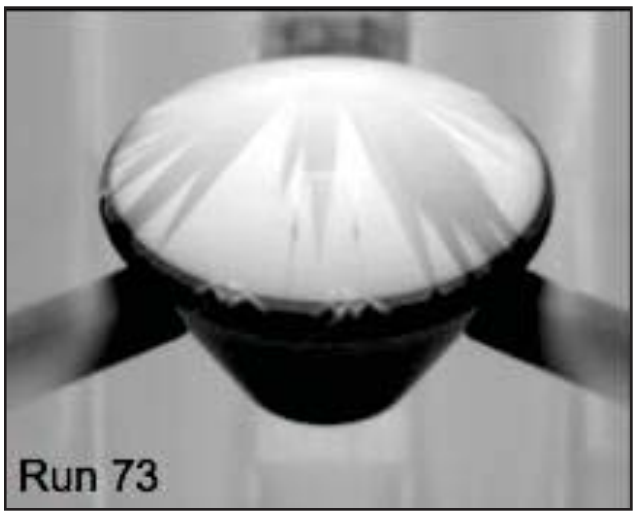

Figure 8.1-6. Top-view IR Image of Smooth Heatshield; M = 0.7, AoA of 30 degrees, and Reynolds Number $10x10^6$

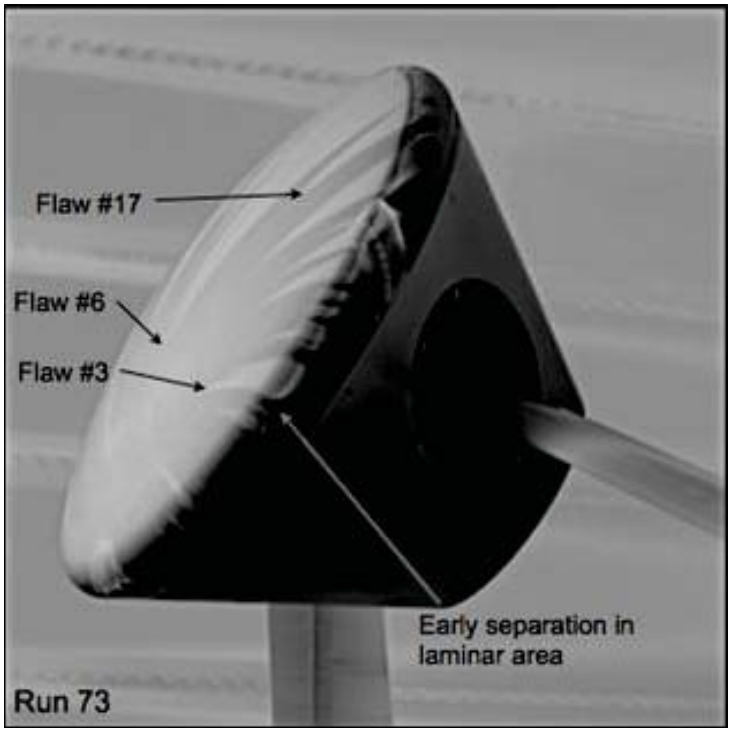

Figure 8.1-7. Side-view of IR Image; M = 0.7, AoA of 30 degrees, and Reynolds Number 10x10^6

In addition to identifying specific locations where transition occurs, the images show the effect of surface discontinuities around the Kulite® inserts. Where the insert edges were not flush with the adjacent model surface, the flow generally separates prematurely.

The flaws on the smooth heatshield were identified visually and by touch. Some are noted in Figure 8.1-7, while the complete map of defects is shown in Figure 8.1-8. The boundary layer was sensitive to surface irregularities and in some instances flush 0.020 inch pressure tap holes.

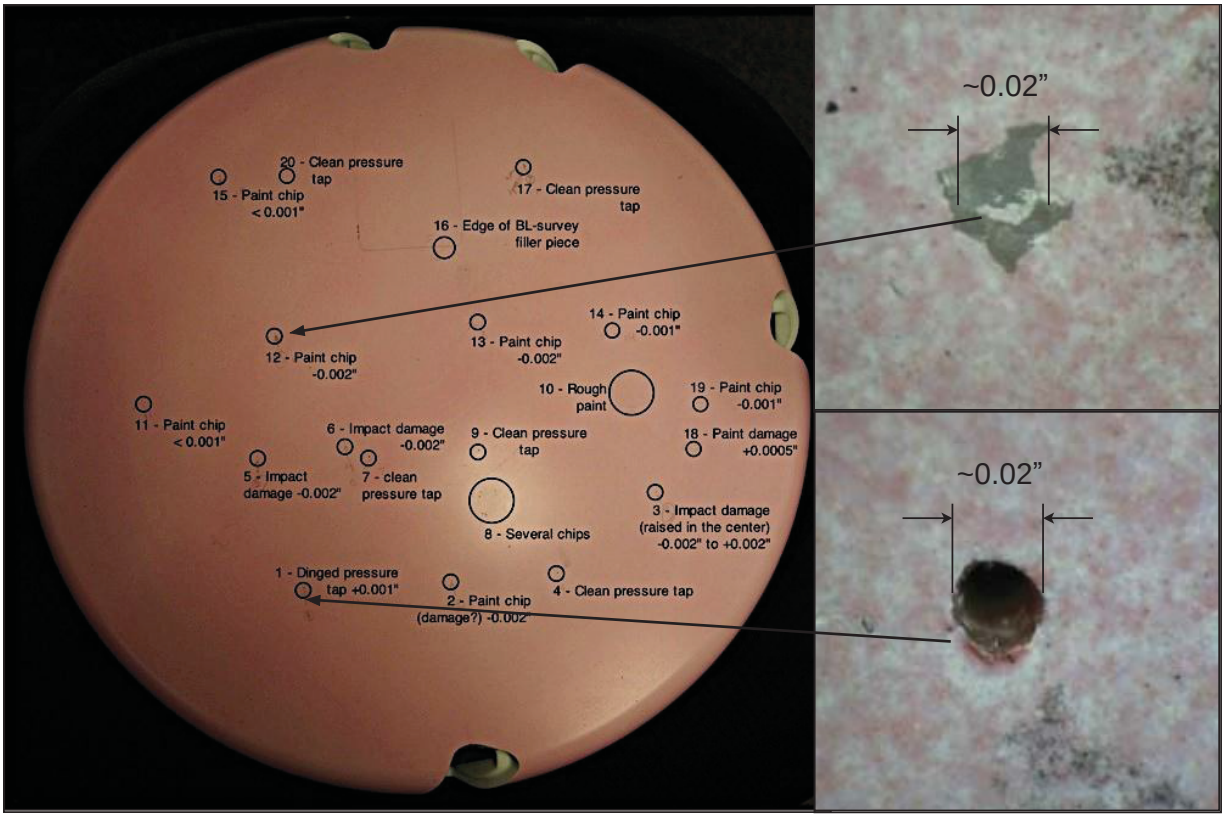

Figure 8.1-8. Map of Defects on Smooth Heatshield

At low Reynolds numbers the boundary layer behavior was significantly different. The flow remained laminar for all test conditions to the suction peak around the heatshield shoulder. Figure 8.1-9 shows an IR image of a low Reynolds number case at Mach 1.02. The flow accelerates to the shock location, where it separates. This is typical of the flow behavior at higher Mach numbers, particularly for the smooth heatshield.

Figure 8.1-9. IR Image of Smooth Heatshield Mach 1.02, AoA of 30 degrees, and Reynolds Number $1.33x10^6$

8.2 PSP Measurements

In general, the PSP data was of high quality. Since it is three-dimensional by its nature, some sample results will be shown. The data archive is described in Appendix D.

8.2.1 Rough Heatshield Results

Figure 8.2-1 shows the time averaged pressure coefficient plotted on the model and strut surfaces for AOA of 30 degrees and Mach numbers of 0.3, 0.7, and 1.07. For the Mach 0.3 case, the pressure coefficient over the surface was noticeably noisier than the other two cases. This was a general finding with PSP, that the data quality is better at high static and dynamic pressure. The noise in the data could have been reduced by sampling longer, but the data was deemed sufficiently converged as acquired. The noise diminishes as the flow accelerates toward the heatshield shoulder. All of the higher Mach number data was clean and represents the state-of-the-art for PSP measurements. Figure 8.2-1 shows the flow was separated over the entire back shell at all Mach numbers, although the separation location was difficult to pinpoint in these color maps. Also apparent in the figure are the pressure data on the upper struts. The PSP was applied to the full length of the upper struts and most of the lower strut surfaces to ensure CFD validation efforts have good documentation of the aerodynamic surfaces present in the test.

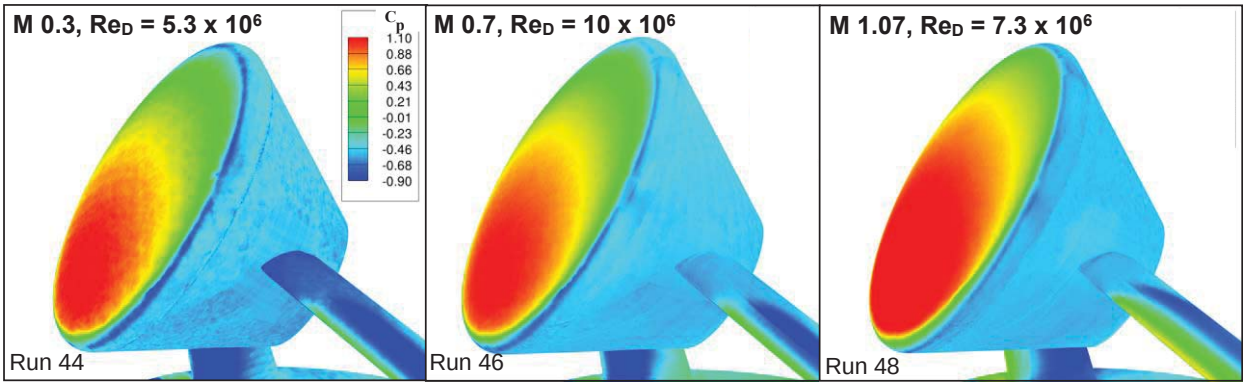

Figure 8.2-1. Pressure Distributions on CM at AoA of 30 Degrees

8.2.2 Integrated Forces and Moments

Since the PSP technique provides pressure over the entire model surface, integration of the pressure to obtain aerodynamic forces and moments was possible. This has been done successfully, but is less accurate and repeatable than a balance measurement [ref. 8]. Since there was no balance in this model, integrating the pressure was the only way to get the aerodynamic information. Table 8.2-1 shows the results of these integrations. The moment reference point is at the heatshield apex.

Table 8.2-1. Integrated Forces and Moments from Surface Pressures

Mach	Alpha	Re (x10-6)	Smooth /Rough	CA	CY	CN	CPM	CLN	Run #
0.70	29.2	1.38	R	0.922	0.011	0.025	-0.075	-0.001	36
0.30	29.2	1.35	R	0.931	0.011	0.026	-0.076	-0.001	42
1.11	29.28	1.65	R	1.225	0.011	0.050	-0.073	-0.002	43
0.30	29.19	5.33	R	0.796	0.016	0.034	-0.059	-0.003	44
0.50	29.19	8.67	R	0.858	0.003	0.034	-0.067	-0.001	45
0.70	29.19	10	R	0.932	0.002	0.029	-0.071	-0.002	46
0.90	29.36	10.01	R	1.064	0.003	0.035	-0.071	-0.003	47
1.07	29.46	6.64	R	1.223	0.006	0.054	-0.074	-0.003	48
0.30	14.05	5.33	R	0.858	0.009	0.074	-0.038	0.001	54
0.50	14.22	8.67	R	0.919	0.004	0.029	-0.036	-0.001	55
0.70	14.31	10	R	1.005	0.002	0.011	-0.035	-0.002	56
0.90	14.39	10.01	R	1.105	0.004	0.004	-0.034	-0.003	57
1.07	14.57	6.62	R	1.265	0.004	0.019	-0.037	-0.002	58
0.70	14.36	10	R	0.993	0.002	0.009	-0.035	-0.002	60
0.70	29.15	1.37	S	0.921	-0.002	0.052	-0.074	0.000	69
1.02	29.21	1.61	S	1.171	0.002	0.066	-0.076	-0.001	70
0.30	29.05	5.33	S	0.812	-0.016	-0.092	-0.062	0.001	71
0.50	29.01	8.67	S	0.895	0.004	-0.116	-0.060	-0.006	72
0.70	28.95	10	S	0.989	0.005	0.076	-0.063	-0.004	73
0.90	29.19	10.02	S	1.096	0.007	0.012	-0.065	-0.004	74
1.08	29.41	6.64	S	1.212	0.005	0.043	-0.067	-0.003	75
0.50	28.9	8.66	S	0.896	0.003	-0.118	-0.058	-0.004	76

Note: Alpha is AoA and Re is Reynolds number.

The integrated axial force coefficient is shown in Figure 8.2-2(a) for the rough heatshield. The results are shown for AoAs of roughly 15 and 30 degrees. Figure 8.2-2(b) shows the axial force coefficient for the rough and smooth heatshields as a function of Mach number at 30 degrees AoA. The rough heatshield produces less axial force than the smooth heatshield because of the pressure recovery after the suction peak that does not occur with the smooth heatshield.

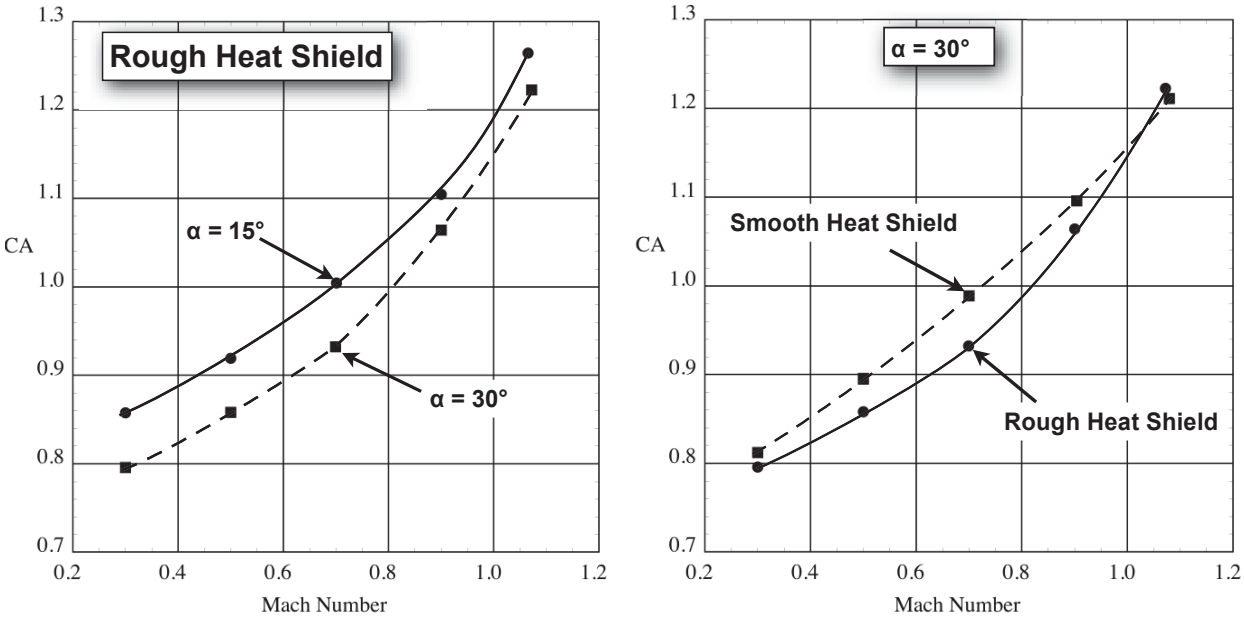

a) Rough heatshield at AoA of 15 and 30 degrees

(b) Rough and smooth heatshields at AoA of 30 degrees

Figure 8.2-2. Axial Force Coefficient Variation with Mach Number

8.3 PIV Measurements

The PIV measurements of the wake velocity distributions were the primary goal of this test and provide insight into the mean flow and turbulence. In addition, the high-speed PIV data in the near wake gives time-accurate velocity data for the lower Mach numbers from which frequency information was computed. The PIV data archive is described in Appendix E.

Figure 8.3-1 shows the mean velocity distribution in the wake from the wide-view PIV system. Velocity fields are shown with the model in the upstream and downstream locations. The cutout in the lower left of the figure shows the model location relative to the measurements. The velocity measurements were continuous between the two measurement areas, in spite of the gap between them. The gap was caused by an area of reflected laser light on the wind tunnel wall, which was visible in one of the cameras. The image contamination from the reflected light meant the velocities could not be computed. A smaller reflection is noted in Figure 8.3-1, which caused a bias in the computed velocity in that region.

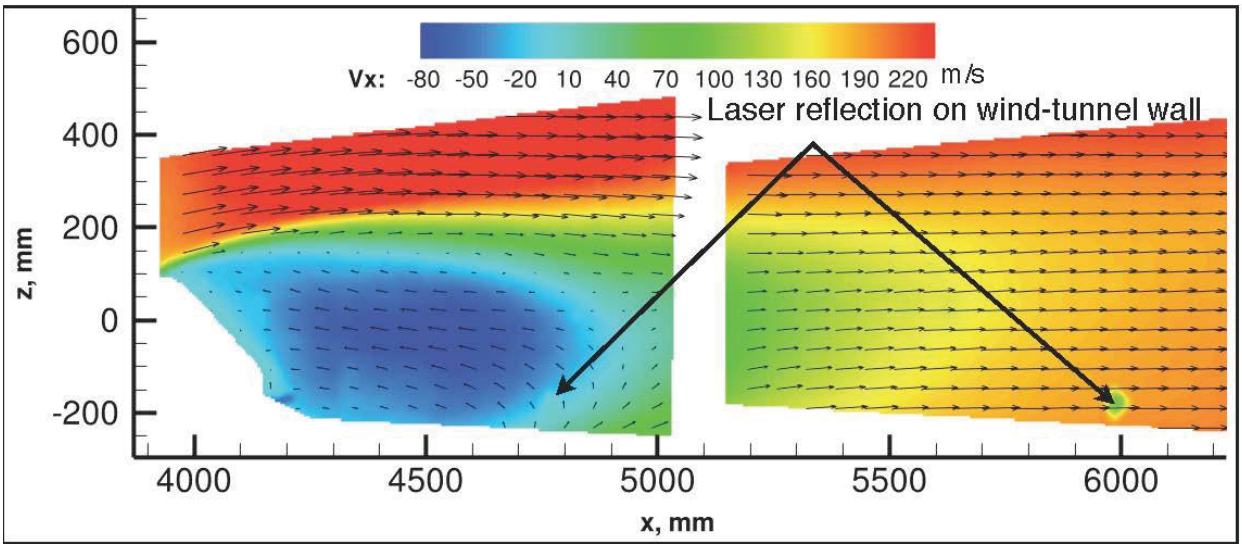

Figure 8.3-1. Average Velocity in CM Wake; Mach 0.7, AoA of 14.0 degrees, and Reynolds Number $10x10^6$ Color Contours of Vx, Every 10^{th} Vector Shown

The root mean square (RMS) of V_x is shown in Figure 8.3-2 for Mach 0.7, AoA of 14.0 degrees, and Reynolds number $10x10^6$. At this test condition, a total of 4,000 image pairs were acquired and the turbulence statistics (e.g., RMS, turbulent kinetic energy, etc.) were nearly identical when computed with either 2,000 or 4,000 velocity measurements. The distribution of V_x RMS was consistent between the two measurement stations in spite of the measurements being taken on different days at the two locations.

One frame of instantaneous velocity data from the high-speed PIV system is shown on the left side of Figure 8.3-3. Vectors show the in-plane velocity (i.e., V_x and V_y) while the color contours show the velocity normal to the plane (i.e., V_z). V_∞ for the measurements in Figure 8.3-3 is 102 meters per second (m/s), so the instantaneous out-of-plane velocity can be a significant fraction of free-stream.

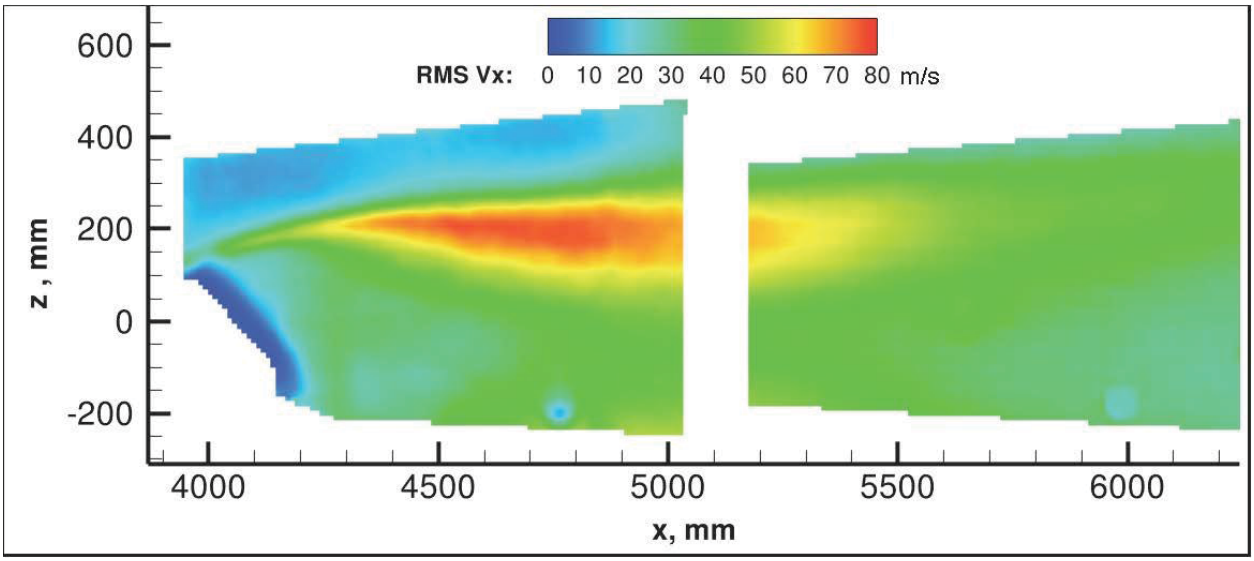

Figure 8.3-2. RMS of Vx in CM Wake; Mach 0.7, AoA of 14.0 degrees, and Reynolds Number 10x10^6

The right-side of Figure 8.3-3 shows the time-averaged velocity vectors for the same test conditions as on the left side, with color contours of V_x. The location of the high-rate PIV measurement plane was selected to capture the shear layer at Mach 0.7 at 15 degrees AoA in the near wake. The location was based on a Reynolds-averaged Navier-Stokes computation of the flow around an isolated capsule. The measurements in Figure 8.3-3 show the measurement area may have missed getting all the way outside the shear layer, but most of the shear layer is resolved at Mach 0.7.

The V_x RMS is shown in Figure 8.3-4 for the same test conditions. Figure 8.3-4 confirms the measurement area did not reach the inviscid outer flow since the V_x RMS reached a minimum of 8 percent of the free-stream velocity at the edge of the measurement area.

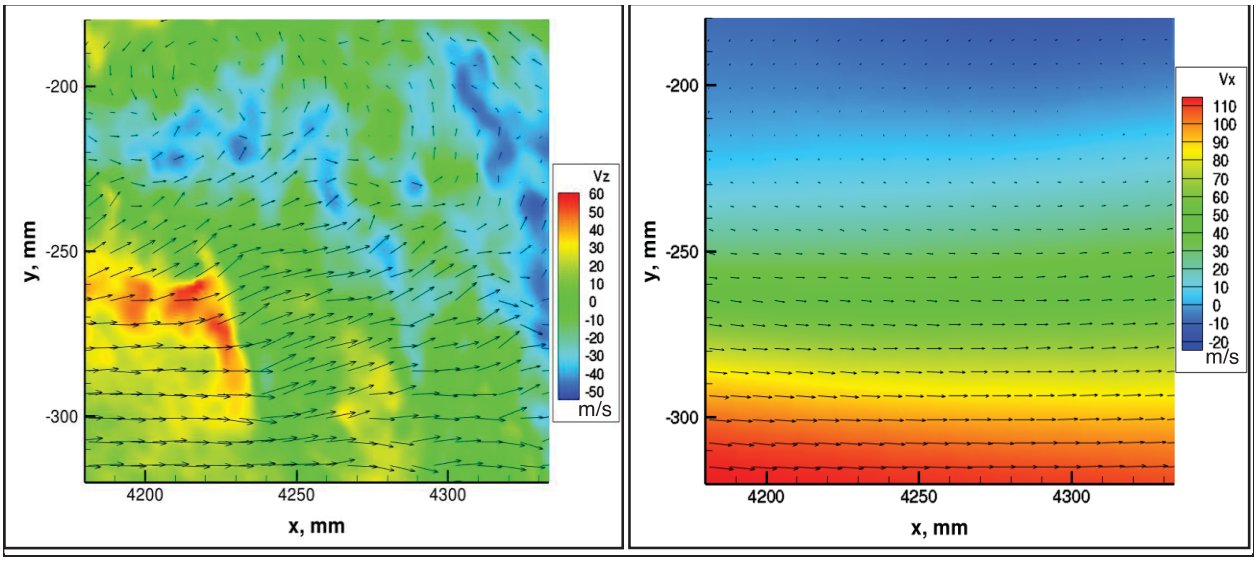

Figure 8.3-3. Velocity Measurements from High-speed PIV; Mach 0.3, AoA of 14.0 degrees, Reynolds Number 5.3x10^6, and V_∞ = 103 m/s

Note: Instantaneous velocity on left, average velocity on right.

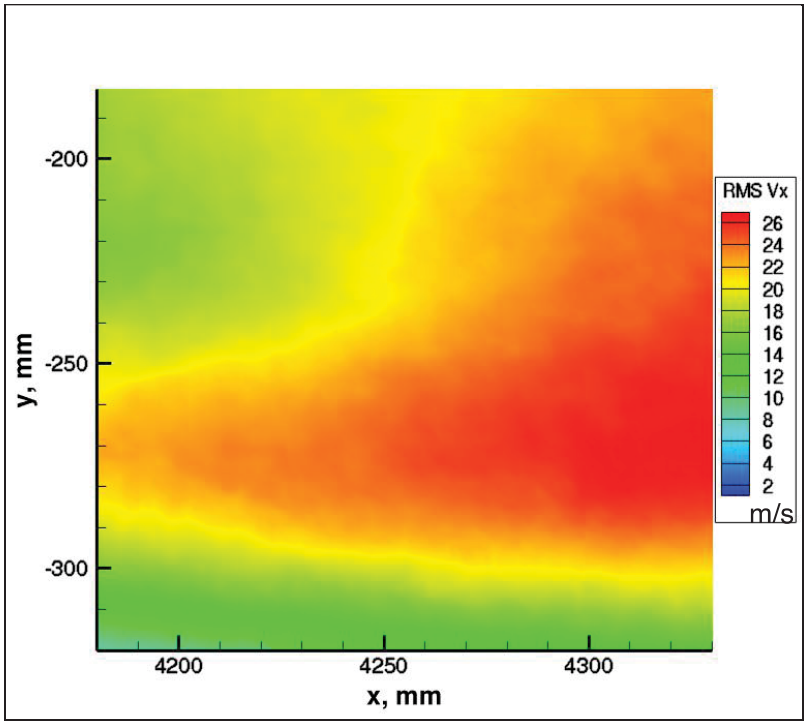

Figure 8.3-4. RMS X-velocity Measurements from High-speed PIV; Mach 0.3, AoA of 14.0 degrees, and Reynolds Number 5.3x10^6

The information needed for the parachute load estimates is the dynamic pressure at the appropriate distance downstream of the capsule. Figure 8.3-5 shows the measured velocity along the center of the wake from the PIV measurements at Mach 0.7 and AoA of 30 degrees. At ~5.1 diameters downstream, the wake velocity was relatively low (i.e., ~145 meters per second (m/s)) compared to the free-stream value of 235 m/s. The velocity fluctuations were large in the wake with an RMS level near 50 m/s (Figure 8.3-2).

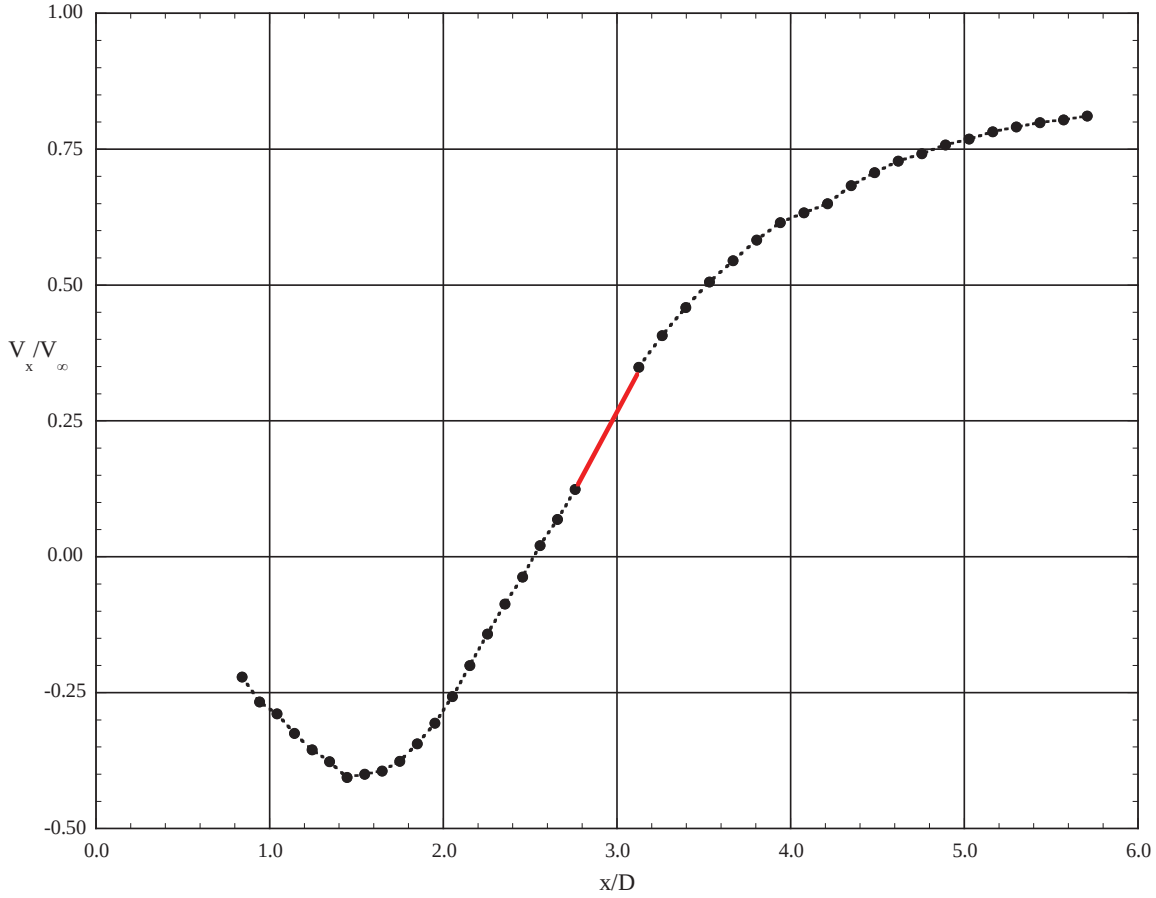

Figure 8.3-5. Distribution of V_x Along Center of Wake at Mach 0.7, AoA of 13.9 degrees, and Reynolds Number 10^7

Note: Red line connects data collected with model in aft position to that collected in the forward position.

Figure 8.3-6 shows time-averaged velocity profiles through the wake at several downstream locations. The profile nearest the model was beyond where the minimum mean axial velocity was no longer negative. At that location the PIV measurement plane extended just outside of the shear layer and the flow acceleration due to wind tunnel blockage and streamline curvature is evident (i.e., velocity greater than free-stream). The y/D value in the figure is referenced to the minimum velocity point at the given axial station rather than from a physical location in the wind tunnel.

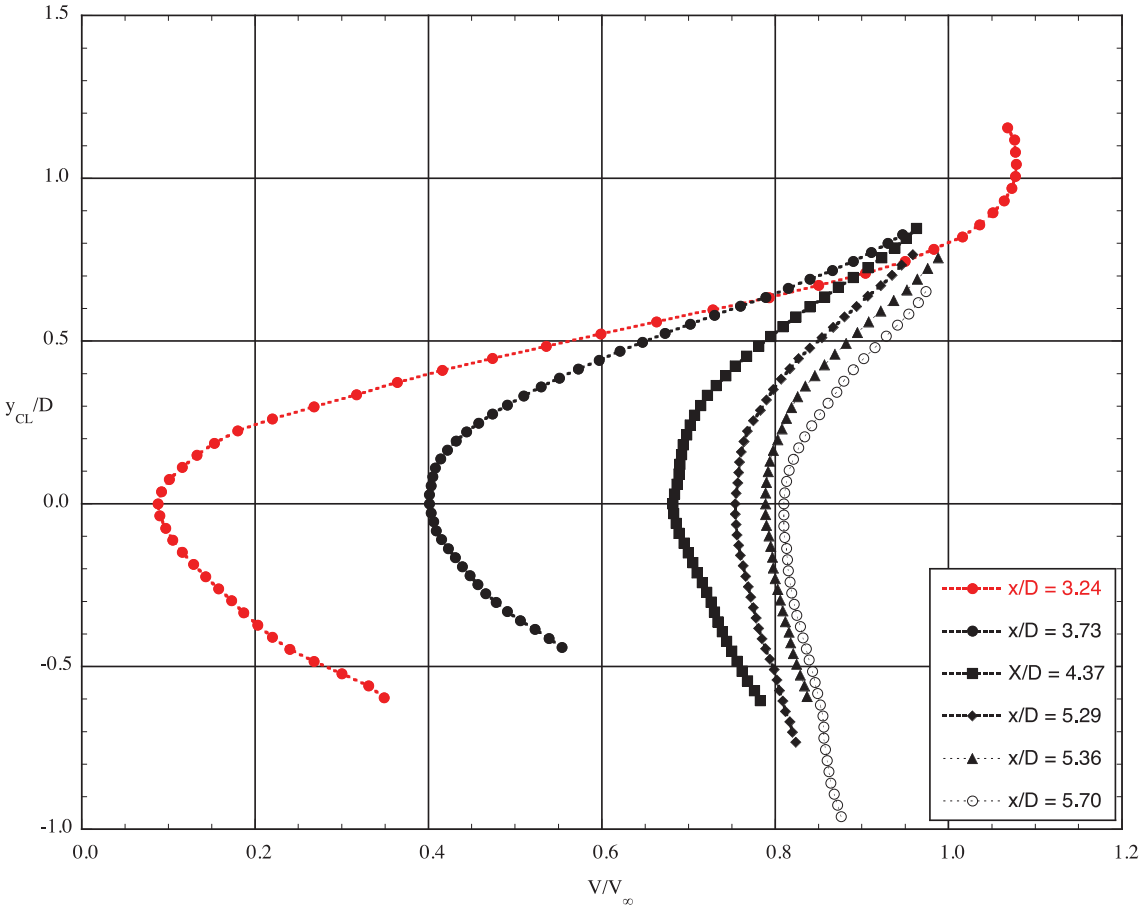

Figure 8.3-6. Variation in Total Velocity at Various Downstream Locations; Mach 0.7, AoA of 13.9 degrees, and Reynolds Number 10^7

Note: Velocity normalized by the free-stream velocity, y_{CL}/D is referenced to the minimum velocity point in the wake at a given x/D location.

The effect of the wake unsteadiness on the load history of a parachute in the wake is difficult to establish from the model data. Figures 8.3-7 and 8.3-8 show instantaneous velocity fields far downstream of the model with a line approximating the parachute diameter and position centered on the wake. The inflated Orion drogue parachute is approximately the same diameter as the CM. Figure 8.3-7 shows a velocity field that is relatively low at the parachute location while Figure 8.3-8 is at an instant showing high velocity at the parachute location.

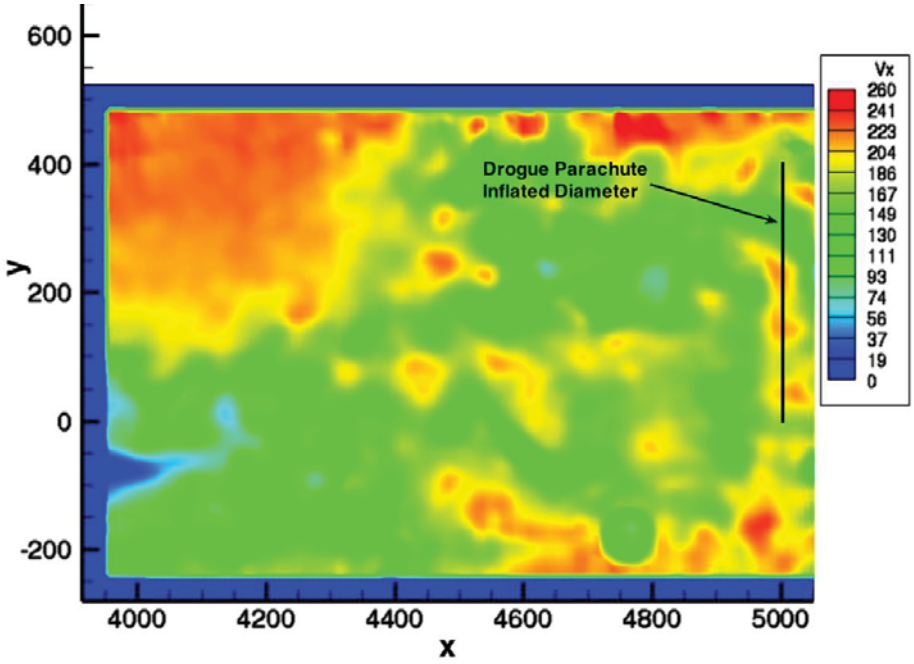

Figure 8.3-7. Contours of V_x in Far-field Wake (Mach 0.7, AoA of 15 degree) at an Instant Showing Low Velocity Across Approximate Drogue Parachute Diameter, V_∞ = 234 m/s

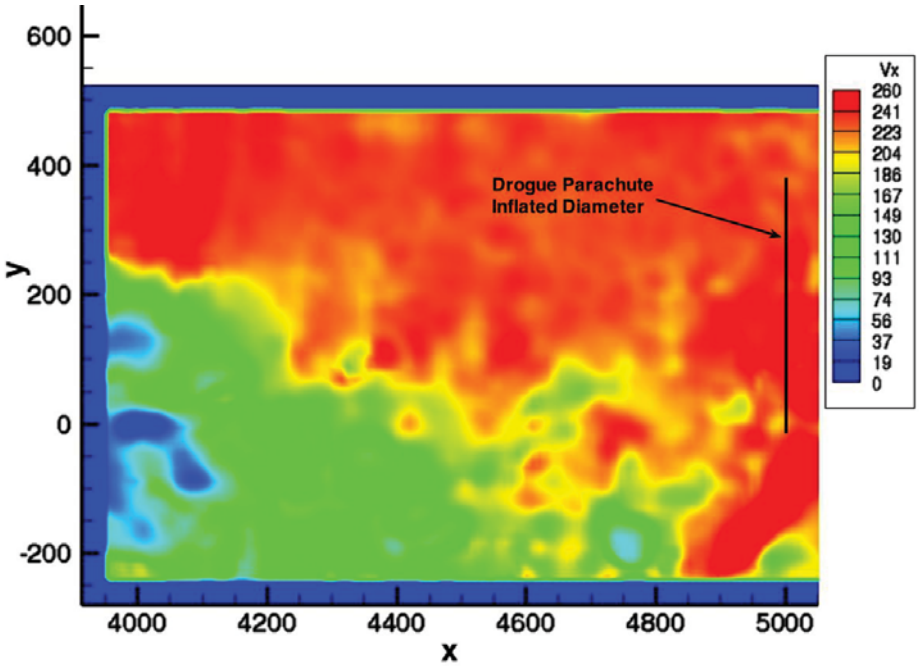

Figure 8.3-8. Contours of V_x in Far-field Wake (Mach 0.7, AoA of 15 degrees) at an Instant Showing High Velocity Across Approximate Drogue Parachute Diameter, V_∞ = 234 m/s

Knacke defines the drag loss coefficient (DLC) to estimate the loads acting on a parachute in the wake of another body (Figure 21 in reference 1). It is determined by measuring the parachute drag in a uniform free-stream and in the wake of the other body. The ratio of the value in the wake to that in the uniform free-stream is the DLC:

$$DLC = \frac{C_{Dwake}}{C_{D\,freeair}}$$

If the parachute shape does not change significantly when in the wake, then the DLC is an indirect measure of the relative integrated effective dynamic pressure acting on the parachute in the wake to that experienced by the parachute in free air. An approximation of the effective dynamic pressure acting on a parachute can be made by integrating the dynamic pressure in the flowfield over the parachute plan area. Assuming the flow on the parachute upper and lower halves are axi-symmetric around the center of the parachute, the DLC can be approximated as:

$$DLC \approx \int_{y=-r}^{y=r} \frac{V^2(y)}{V^2{}_\infty} y dy$$

The DLC can be calculated instantaneously or using time-averaged velocities. The DLC as reported in reference 1 is a time-averaged quantity. It was computed at a variety of downstream locations from the current velocity data at Mach 0.7. Figure 8.3-9 shows the results of these integrations for available locations in the current data set. It is clear from the comparison with the D_p/D_B ~1 curve that integrating the current results in lower values of DLC than in the literature. One reason is the bodies for most of the data referenced in the figure were obtained with a parachute behind and body with a higher fineness ratio than the capsule. The Apollo drogue chute behind the CM was an exception and it lies on the curve-fit to the rest of the data plotted by Knacke. It is not clear how to account for this discrepancy, but the approximation of axi-symmetric flow from the planar data set and the asymmetry apparent in the current data could be part of the issue. Regardless, it appears using the curves in Knacke would be reasonable.

Using the instantaneous velocity fields shown in Figures 8.3-6 and 8.3-7 to compute DLC gives a range of fluctuating loads that the parachute might experience. For the low-velocity instance, the DLC is 0.35 while at the high-velocity instance it is 0.79. The two velocity measurements do not necessarily represent the highest and lowest integrated loads. These measurements were selected as representative high- and low-velocity from the first 100 of the 4,000 velocity instances measured at this test condition.

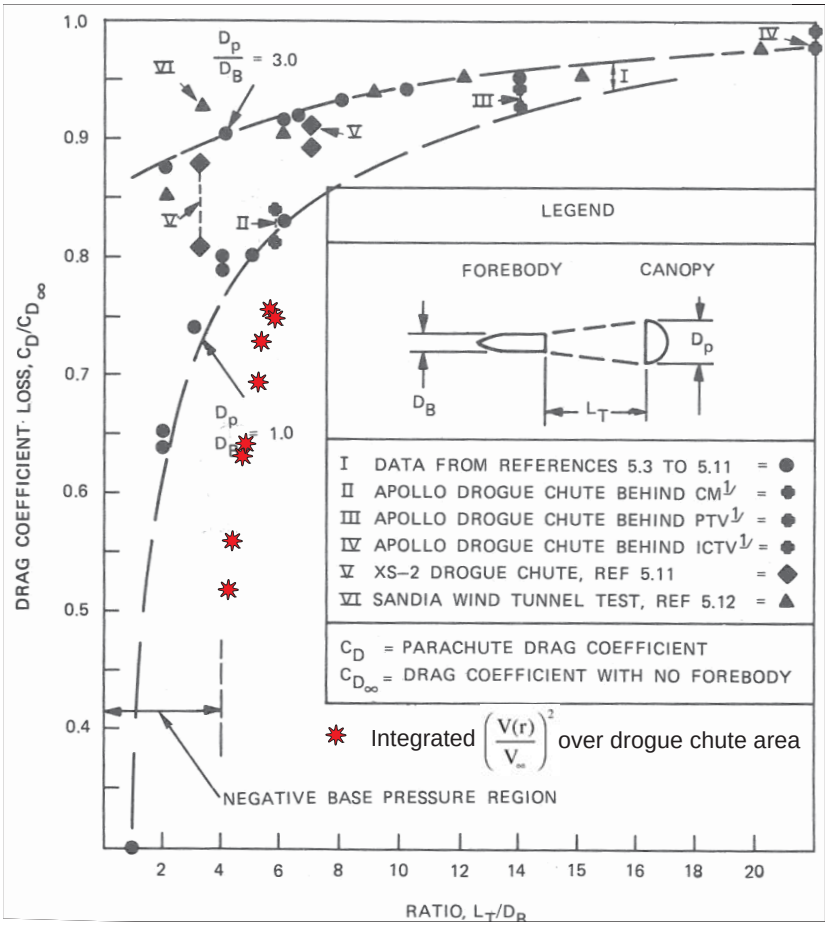

Figure 8.3-9. DLC from Current Study Compared to Results in Reference 1
Note: The red symbols should be compared with the lower curve, D_p/D_B ~1.0. Should be most comparable to the Apollo drogue chute behind CM (symbol II, Figure scanned from reference 1).

8.4 Unsteady Pressure Measurements

The flow over bluff bodies is generally unsteady and the unsteady pressure measurements provide insight into the character of the unsteadiness. The unsteady pressure data archive is described in Appendix F. Observing the model motion and unsteady strain gauge readings gave a good indication of the unsteadiness. In general, the model shook more at lower AoAs at a given Mach number than at higher AoAs. The unsteadiness increased with Mach number to above Mach 0.7. Above Mach 0.7, the flow separation seemed to be fixed by the shocks at the heatshield shoulder, which greatly reduced the model dynamics. When the flow was supersonic, the unsteadiness was small. The upper strut strain gauge readings became steadier and the model motion was almost completely eliminated. These observations were consistent with the unsteady pressure measurements. At supersonic conditions the pressure fluctuations were low and increased at Mach numbers below 0.9.

The unsteady pressure transducers provided quantitative information that corroborated the visual observations. Figure 8.4-1 is a map showing the 1/3rd octave sound pressure levels (SPLs) for the heatshield transducers on the rough heatshield at Mach 0.7, AoA of 29.25 degrees, and Reynolds number $10x10^6$. The color of each box in the figure represents the 1/3-octave SPL for a given sensor with the sensor numbers on the left-side of the SPL map. There are four groups of 10 Kulites® and the transducers in each group of 10 are located in the inserts as shown in the heatshield sketch on the left-side of the figure. The level of unsteadiness is an indicator of flow separation as noted in Figure 8.4-1. The SPL for sensors upstream of the flow separation is relatively low (i.e., green or blue) while at, or slightly downstream of separation, the levels are significantly higher (i.e., orange or red). The separation locations determined from the unsteady pressure levels match well with the locations visualized in the IR images.

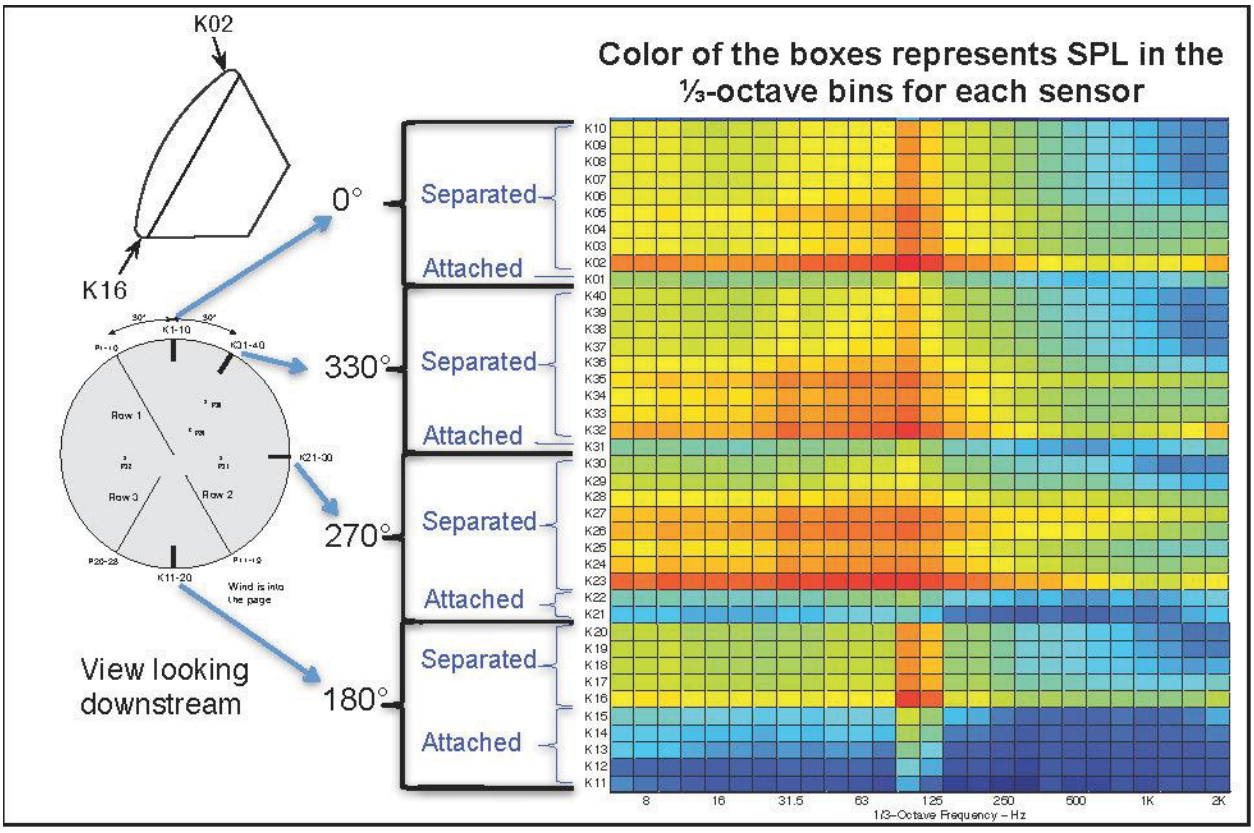

Figure 8.4-1. 1/3-octave SPL Levels for Unsteady Pressures; Mach 0.7, AoA of 29.25 degrees, and Reynolds Number $10x10^6$

The dominant shedding frequency of the model is apparent in the SPL map in Figure 8.4-1. The levels in the 100 to 125 Hertz (Hz) frequency range are higher on almost all the sensors relative to the adjacent frequency bins. Figure 8.4-2 shows the narrow-band spectra of two of the sensors (i.e., K02 and K16) for sensors at the same free-stream conditions as in Figure 8.4-1. Two sets

of curves are shown for the smooth and rough heatshields. The Strouhal number (*St*) for the rough heatshield is ~15 percent lower than for the smooth heatshield, which is defined as:

$$St = \frac{fD}{V}$$

where f is the shedding frequency, D is the characteristic width of the body (diameter in this case), and V is the free-stream velocity.

The roughness increases the effective model diameter in regard to the dominant shedding frequency. A decrease in *St* for a circular cylinder with roughness is documented in reference 17, which reported up to a 12 percent decrease in *St* using wire mesh attached to the model surface for roughness. While the boundary layer turbulence generated by a wire mesh may differ from that due to a hexagonal dimple pattern, the current findings are consistent with those in reference 17.

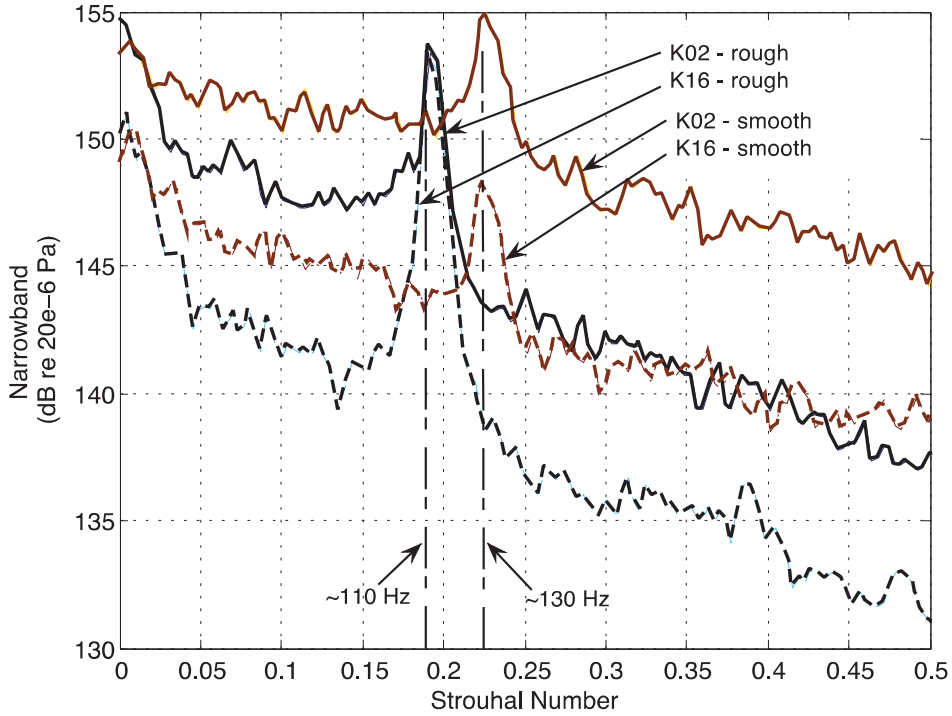

Figure 8.4-2. Narrow Band SPL Levels Showing Effect of Roughness on Shedding Frequency; Mach 0.7, AoA of 29.25 degrees, and Reynolds Number 10x10^6

The Mach number has an effect on the *St*. Figure 8.4-3 shows the Mach number effect for the CM at 30 degrees AoA. The Reynolds number is not the same at all Mach numbers, but the change in shedding is striking at Mach 1.07 where the shedding is weaker than the subsonic

Mach numbers. The frequency was higher for the supersonic case where *St* = 0.33 versus ~0.2 for the subsonic/transonic conditions.

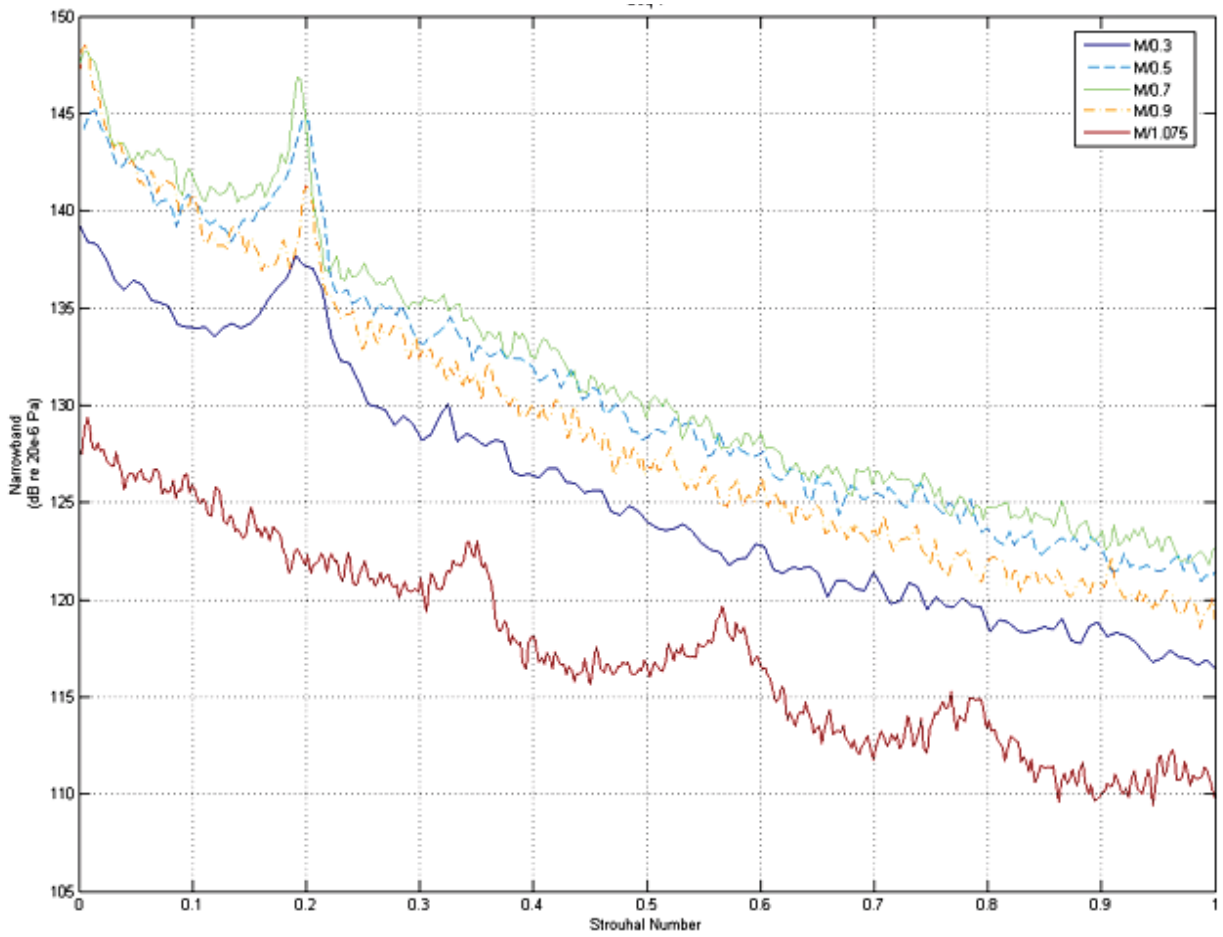

Figure 8.4-3. Narrow Band SPL Levels Showing Effect of Mach Number on Shedding Frequency; Mach 0.7, AoA 29.25 degrees, and Reynolds Number 10x10^6

Time correlations between various sensors were examined to ascertain whether the pattern of flow separation dynamics could be discerned. Figure 8.4-4 shows the results of time correlations on the rough heatshield for the Mach 0.7, 30 degrees AoA, and high Reynolds number condition. In Figure 8.4-4 the reference signal comes from K8, at the top of the model and is located in the separated flow. K19, K29, and K39 are 180, 90, and 30 degrees from the reference transducer, respectively. Following the logic in the figure with K39, K29, and K19 lagging K8 in that order, the case can be made for a spiral separation pattern moving clockwise looking at the heatshield. Additional analysis and/or testing is required to verify or refute this conjecture.

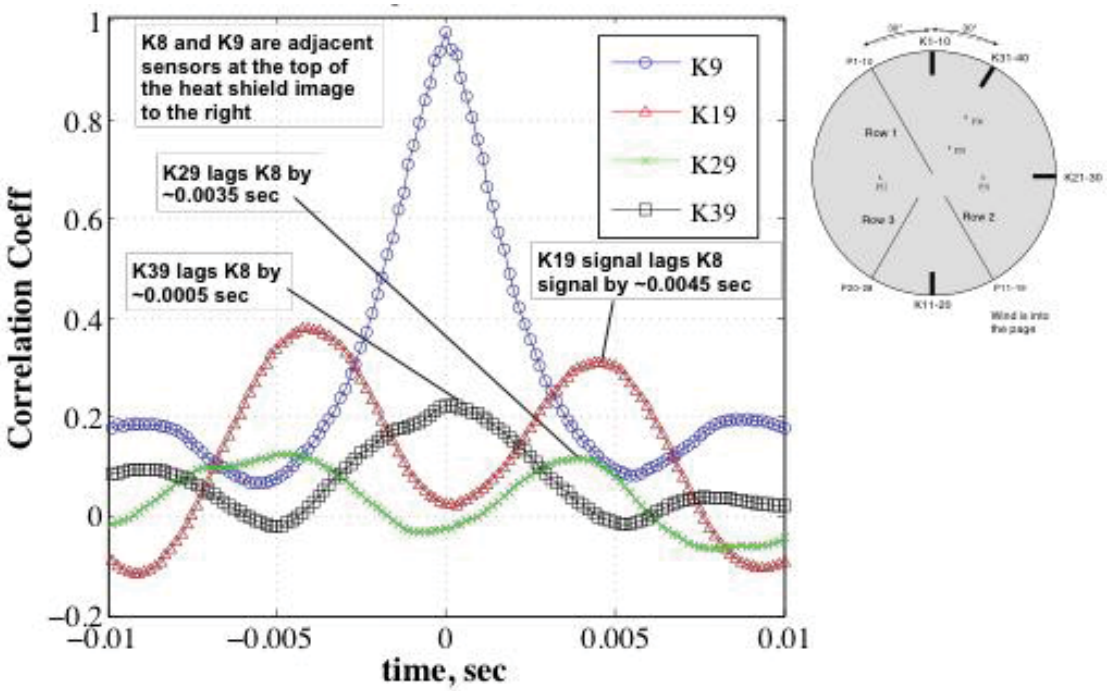

Figure 8.4-4. Correlation Coefficient versus Time Referenced to Sensor K8; Mach 0.7, AoA of 29.25 degrees, and Reynolds Number 10x10^6

8.5 Boundary Layer Measurements

Boundary layer measurements were made on the heatshield for a limited set of conditions and outlined in Table 5.2-1. All of the measurements were made on the rough heatshield because of time constraints during the test. The boundary layer data archive is described in Appendix G.

8.5.1 Boundary Layer Surveys

Boundary layer profiles were documented at the traversing probe location (x = 0.205 inch, y = 0 inch, and z = 2.800 inch) from the heatshield apex. The insert is smooth and the length of smooth surface from the edge of the insert to the probe tip is 0.5 inch. Figure 8.5-1 shows boundary layer profiles plotted as local Mach number versus distance from the model surface. The plot shows the effect of AoA at free-stream Mach 0.7 with an additional profile for Mach 1.05 at 29.4 degree AoA. In general, increasing the AoA increases the boundary layer thickness due to the longer run from the stagnation point to the measurement location. The Mach number at the edge of the boundary layer increased with AoA at the measurement station. Increasing the Mach number from 0.7 to 1.05 at 29.4 degrees AoA did not change the boundary layer thickness. This change increased the local Mach number at the boundary layer edge.

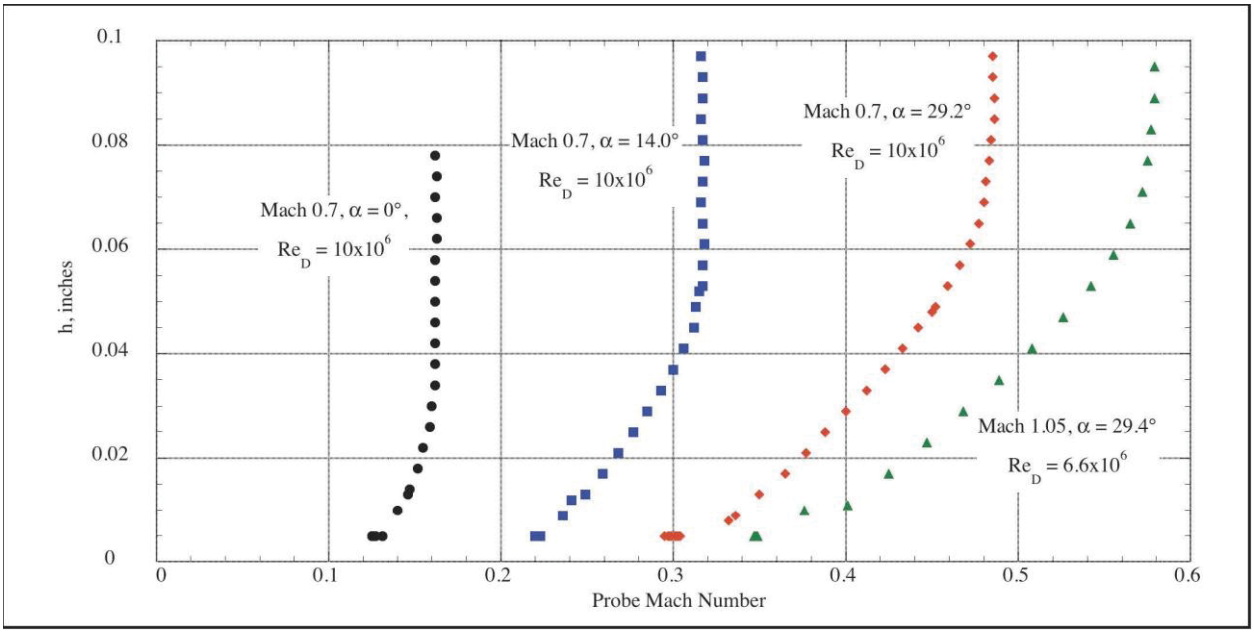

Figure 8.5-1. Boundary Layer Profiles for Rough Heatshield

The skin friction was measured using OFI for three flow conditions at 15 degrees AoA: Mach 0.3 at Reynolds number $5.3x10^6$, Mach 0.7 at Reynolds number $10x10^6$, and M 1.05 at Reynolds number $6.6x10^6$. Figure 8.5-2 shows the oil fringes with the resulting skin friction values for the Mach 0.7 condition. These three OFI skin friction values were used to calibrate the Stanton gauge, located adjacent to the probe. The Stanton gauge provided the skin friction measurements for the rest of the test conditions for which boundary layer profiles were acquired. Limiting the number of OFI skin friction measurements was done to minimize wind tunnel test time as each oil film measurement required approximately an hour of testing. The location of the probe relative to the rough heatshield surface is shown in Figure 8.5-2 as are the locations of the static pressure tap and the Stanton gauge adjacent to the probe. The dots surrounding the insert are fiducial marks allowing precise registration of the image relative to the model surface. The dots provide accurate scaling in the image from which the fringe spacing can be determined.

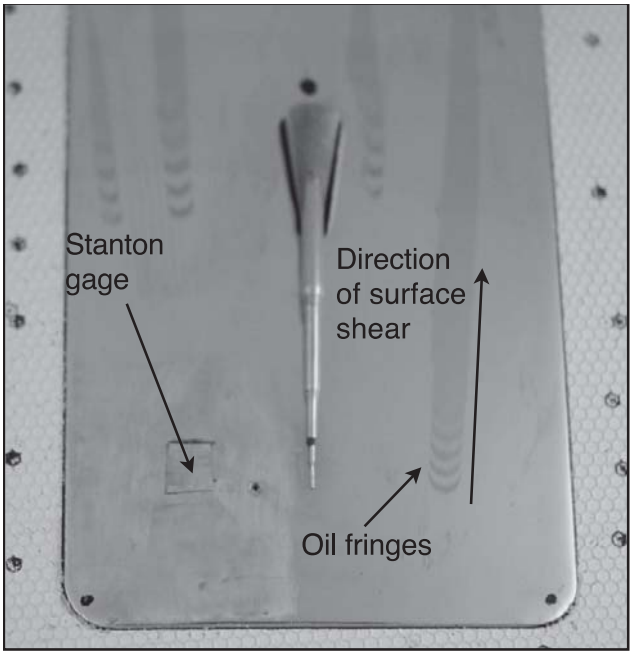

Figure 8.5-2. Example of Oil Film Images for Measuring Skin Friction; Mach 0.7, AoA of 15 degrees, and Reynolds Number 10x10^6, Skin Friction Coefficient = 0.0026 directed 4.6 degrees from Vertical

9.0 Findings, Observations, and NESC Recommendations

9.1 Findings

The following findings were identified:

F-1. The heatshield roughness has a significant effect on the capsule aerodynamics (e.g., smooth heatshield drag is up to 8 percent higher than for the rough heatshield).

F-2. The fundamental unsteadiness of the flow around a capsule precludes the use of non-time-accurate computational tools to determine the wake deficit.

F-3. The unsteadiness increases as the AoA is decreased from 30 to 0 degrees.

F-4. Handbook values for the wake deficit behind capsules at subsonic/transonic Mach numbers are similar to the results of the current test. The handbook values appear to be conservative for trailing distances less than ~6 capsule diameters with no evidence the trend changes at larger downstream distances.

F-5. Wake motion and velocity fluctuation are not well represented in the handbook information used for parachute load estimates, but these qualities could be important when designing for maximum loads.

F-6. Large unsteadiness in the near wake could lead to unexpectedly large instantaneous loads on inflating parachutes.

9.2 Observations

The following observations were identified:

O-1. The *St* for the capsule shape is close to 0.2 for Mach numbers below 0.9. For supersonic free-stream, the shedding is less periodic with the lowest dominant frequency at a *St* of 0.4.

O-2. Large velocity fluctuations are seen in the CM model wake. In the near wake, the RMS of V_x exceeds 20 percent of the free stream velocity. The eddies shed from the capsule are large, particularly at Mach numbers of 0.3, 0.5, and 0.7. The shadowgraph videos show at a distance of 2 capsule diameters downstream of the model, the eddies can travel laterally ±0.25D from the mean shear layer location.

9.3 NESC Recommendations

The following NESC recommendations were identified and directed towards the MPCV CPAS project unless otherwise identified:

R-1. Include the effect of physically scaled heatshield roughness in wind tunnel tests. ***(F-1)***

R-2. Perform computational modeling of bluff-body aerodynamics in a time-accurate manner. ***(F-4, F-5)***

10.0 Alternate Viewpoint

There were no alternate viewpoints identified during the course of this assessment by the NESC team or the NESC Review Board (NRB) quorum.

11.0 Other Deliverables

No unique hardware, software, or data packages, outside those contained in this report, were disseminated to other parties outside this assessment.

12.0 Lessons Learned

No applicable lessons learned were identified for entry into the NASA Lessons Learned Information System (LLIS) as a result of this assessment.

13.0 Recommendations for NASA Standards and Specifications

No recommendations for NASA standards and specifications were identified as a result of this assessment.

14.0 Definition of Terms

Corrective Actions	Changes to design processes, work instructions, workmanship practices, training, inspections, tests, procedures, specifications, drawings, tools, equipment, facilities, resources, or material that result in preventing, minimizing, or limiting the potential for recurrence of a problem.
Finding	A relevant factual conclusion and/or issue that is within the assessment scope and that the team has rigorously based on data from their independent analyses, tests, inspections, and/or reviews of technical documentation.
Lessons Learned	Knowledge, understanding, or conclusive insight gained by experience that may benefit other current or future NASA programs and projects. The experience may be positive, as in a successful test or mission, or negative, as in a mishap or failure.
Observation	A noteworthy fact, issue, and/or risk, which may not be directly within the assessment scope, but could generate a separate issue or concern if not addressed. Alternatively, an observation can be a positive acknowledgement of a Center/Program/Project/Organization's operational structure, tools, and/or support provided.
Problem	The subject of the independent technical assessment.
Proximate Cause	The event(s) that occurred, including any condition(s) that existed immediately before the undesired outcome, directly resulted in its occurrence and, if eliminated or modified, would have prevented the undesired outcome.
Recommendation	A proposed measurable stakeholder action directly supported by specific Finding(s) and/or Observation(s) that will correct or mitigate an identified issue or risk.
Root Cause	One of multiple factors (events, conditions, or organizational factors) that contributed to or created the proximate cause and subsequent undesired outcome and, if eliminated or modified, would have prevented the undesired outcome. Typically, multiple root causes contribute to an undesired outcome.
Supporting Narrative	A paragraph, or section, in an NESC final report that provides the detailed explanation of a succinctly worded finding or observation. For example, the logical deduction that led to a finding or observation; descriptions of assumptions, exceptions, clarifications, and boundary conditions. Avoid squeezing all of this information into a finding or observation

15.0 Acronyms List

µm	Micrometre
A&M	Agricultural and Mechanical
AMA	Analytical Mechanics Associates, Inc.
AoA	Angle of Attack
ARC	Ames Research Center
AUPWT	Ames Unitary Plan Wind Tunnel
CAD	Computer-aided Design
CEV	Crew Exploration Vehicle
CFD	Computational Fluid Dynamics
CM	Crew Module
CPAS	Capsule Parachute Assembly System
DLC	Drag Loss Coefficient
FML	Fluid Mechanics Laboratory
ft	Foot
Hz	Hertz
IR	Infrared
LaRC	Langley Research Center
m/s	Meters per Second
MPCV	Multi-Purpose Crew Vehicle
NESC	NASA Engineering and Safety Center
NRB	NESC Review Board
OFI	Oil-Film Interferometry
PIV	Particle Image Velocimetry
psid	Pounds per Square Inch
PSP	Pressure Sensitive Paint
RANS	Reynolds-averaged Navier-Stokes
Re	Reynolds Number
RMS	Root Mean Square
SDS	Standard Data System
SLS	Selective Laser Sintering
SPL	Sounds Pressure Level
St	Strouhal Number

15.1 Nomenclature

AF	Axial Force, acting in the x-direction in the model-fixed coordinate system
CA	Axial Force Coefficient, $CA = \frac{AF}{q_{\square}}$

Re	Reynolds Number, $\mathrm{Re} = \frac{V_\infty D}{\nu}$
M	Mach number
$P_s(t)$	Static Pressure at time = t, $P_s(t) = \bar{P}_s + P_s'(t)$
$\bar{P}_s$	Time-averaged Static Pressure
$P_s'(t)$	Fluctuating component of Static Pressure
P_∞	Time-averaged free-stream Static Pressure
q_∞	Free-Stream Dynamic Pressure
t	Time, seconds
V_∞	Free-stream Velocity
V_x	x-component of local velocity
V_y	y-component of local velocity
V_z	z-component of local velocity
x	Stream-wise coordinate, wind-tunnel axes
y	Cross-stream, lateral coordinate, wind-tunnel axes
z	Cross-stream, vertical coordinate, wind-tunnel axes
ρ	Free-stream air density
ν	Free-stream kinematic viscosity

16.0 References

1. Knacke, T. W., Parachute Recovery Systems Design Manual, Para Publishing, January 1992.
2. Braslow, A. L., and Knox, E. C., "Simplified Method for Determination of Critical Height of Distributed Roughness Particles for Boundary Layer Transition at Mach Numbers from 0 to 5," NACA TN 4363, 1958.
3. Braslow, A. L., Hicks, R. M., and Harris, R. V., Jr., "Use of Grit-Type Boundary-Layer-Transition Trips on Wind-Tunnel Models," NASA TN D-3579, 1966.
4. Amaya, M. A., and Boone, A. R., "Calibration of the 11x11-Foot Transonic Wind Tunnel at the NASA Ames Research Center," AIAA 41st AIAA/ASME/SAE/ASEE Joint Propulsion Conference and Exhibit, AIAA paper 2005-4277, Tucson, AZ, July 10-13, 2005.
5. Sengupta, A., et al, "Performance of a Conical Ribbon Drogue Parachute in the Wake of a Subscale Orion Command Module," 2012 IEEE Aerospace Conference, Big Sky, MT, March 3-10, 2012.
6. Brauckmann, G. J., "Final Report for Test 89-CA: High-Reynolds Number Test of the Orion Crew Module in the NASA LaRC National Transonic Facility," MPCV Aerosciences Report EG-CAP-12-65, September 2012.

7. Alunni, A. I., Olson, M. W., Gökçen, T., and Skokova, K. A., "Comparisons of Surface Roughness in Laminar and Turbulent Environments for Orion Thermal Protection System," AIAA paper 2011-3776, 42nd AIAA Thermophysics Conference, Honolulu, HI, June 27-30, 2011.

8. Sellers, M. E., "Demonstration of a Temperature-Compensated Pressure Sensitive Paint on the Orion Launch Abort Vehicle," AIAA Paper 2011-3166, AIAA Applied Aerodynamics Conference, Honolulu, HI, June 2011.

9. Driver, D. M., "Application of Oil-Film Interferometry Skin-Friction Measurements to Large Wind Tunnels," *Experiments in Fluids*, vol. 34, pp. 717-725, 2003.

10. Naughton, J. W., and Liu, T., "Photogrammetry in Oil-Film Interferometry," AIAA Journal, vol. 45, no. 7, pp. 1620-1629, July 2007.

11. Bradshaw, P. and Gregory, N., "The Determination of Local Turbulent Skin Friction from Observations in the Viscous Sub-Layer," Aeronautical Research Council Report R&M No. 3202, Her Majesty's Stationery Office, London, March 1959.

12. East, L. F., "Measurement of Skin Friction at Low Subsonic Speeds by the Razor-Blade Technique," *A.R.C.R. & M*, 1968.

13. Smith K. G, Gaudet L., and Winter K. G., "The Use of Surface Pitot Tubes as Skin-Friction Meters at Supersonic Speeds," *A.R.C.R. & M*, 1964.

14. Schairer, E. T., Heineck, J. T., Walker, S. M., and Yaste, D. M., "Predicting Camera Views for Image-Based Measurements in Wind Tunnels," AIAA Paper 2005-1349, 43rd AIAA Aerospace Sciences Meeting and Exhibit, Reno, NV, Jan. 10-13, 2005.

15. Kushner, L. K., "Planning Image-Based Measurements in Wind Tunnels," AIAA Paper 2011-930, 49th AIAA Aerospace Sciences Meeting and Exhibit, Orlando, FL, Jan. 4-7, 2011.

16. Heineck, J. T., Schairer, E. T., and Walker, S. M., "PIV in NASA Ames Unitary Wind Tunnels," AIAA 49th Aerospace Sciences Meeting, Orlando, FL, January 4-7, 2011.

17. Shih, W. C. L., Wang, C., Coles, D., and Roshko, A., "Experiments on Flow Past Rough Circular Cylinders at Large Reynolds Numbers," *Journal of Wind Engineering and Industrial Aerodynamics*, vol. 49, pp. 351-368, 1993.

17.0 Appendices

Appendix A. Static Pressure Tap Locations
Appendix B. Unsteady Pressure Tap Locations
Appendix C. IR Thermography Image Archive Description
Appendix D. PSP Data Archive Description
Appendix E. PIV Data Archive Description
Appendix F. Unsteady Pressured Data Archive Description
Appendix G. Boundary Layer Data Archive Description
Appendix H. Test Condition and Static Pressure Tap Data Archive Description

Appendix A. Static Pressure Tap Locations

TAP ID	COMPONENT	NOMINAL ANGLE	X, inch	Y, inch	Z, inch	RADIUS, inch
1	HEATSHIELD	0	0.000	0.000	0.000	0.000
2	HEATSHIELD	30	0.109	1.022	1.770	2.043
3	HEATSHIELD	30	0.587	2.356	4.081	4.712
4	HEATSHIELD	30	1.313	3.489	6.043	6.978
5	HEATSHIELD	30	1.492	3.710	6.425	7.419
6	HEATSHIELD	30	1.657	3.859	6.683	7.717
7	HEATSHIELD	30	1.928	3.962	6.862	7.924
8	HEATSHIELD	30	2.259	4.000	6.927	7.999
9	HEATSHIELD	30	2.593	3.965	6.868	7.930
10	HEATSHIELD	30	2.891	3.881	6.722	7.762
11	HEATSHIELD	210	0.109	-1.022	-1.770	2.043
12	HEATSHIELD	210	0.587	-2.356	-4.081	4.712
13	HEATSHIELD	210	1.313	-3.489	-6.043	6.978
14	HEATSHIELD	210	1.492	-3.710	-6.425	7.419
15	HEATSHIELD	210	1.657	-3.859	-6.683	7.717
16	HEATSHIELD	210	1.928	-3.962	-6.862	7.924
17	HEATSHIELD	210	2.259	-4.000	-6.927	7.999
18	HEATSHIELD	210	2.593	-3.965	-6.868	7.930
19	HEATSHIELD	210	2.891	-3.881	-6.722	7.762
20	HEATSHIELD	150	0.109	1.022	-1.770	2.043
21	HEATSHIELD	150	0.587	2.356	-4.081	4.712
22	HEATSHIELD	150	1.313	3.489	-6.043	6.978
23	HEATSHIELD	150	1.492	3.710	-6.425	7.419
24	HEATSHIELD	150	1.657	3.859	-6.683	7.717
25	HEATSHIELD	150	1.928	3.962	-6.862	7.924
26	HEATSHIELD	150	2.259	4.000	-6.927	7.999
27	HEATSHIELD	150	2.593	3.965	-6.868	7.930
28	HEATSHIELD	150	2.891	3.881	-6.722	7.762
29	HEATSHIELD	330	0.109	-1.022	1.770	2.043
30	HEATSHIELD	330	0.587	-2.356	4.081	4.712
31	HEATSHIELD	270	0.109	-2.043	0.000	2.043
32	HEATSHIELD	90	0.109	2.043	0.000	2.043
33	BACK SHELL		9.500	-3.947	0.000	3.947
34	STRUT FAIRING LHS		8.272	-4.655	0.089	4.656

35	STRUT FAIRING LHS		7.954	-4.738	-0.989	4.840
36	STRUT FAIRING LHS		7.083	-5.093	-1.613	5.342
37	STRUT FAIRING LHS		6.108	-5.679	-1.618	5.905
38	STRUT FAIRING LHS		5.298	-6.279	-1.090	6.373
39	STRUT FAIRING LHS		4.901	-6.601	-0.089	6.602
40	STRUT FAIRING LHS		5.200	-6.357	0.962	6.429
41	STRUT FAIRING LHS		5.967	-5.777	1.570	5.987
42	STRUT FAIRING LHS		6.929	-5.174	1.652	5.431
43	STRUT FAIRING LHS		7.844	-4.772	1.125	4.903
44	BACK SHELL	330	4.901	-3.300	5.718	6.602
45	BACK SHELL	210	4.901	-3.300	-5.718	6.602
46	BACK SHELL		9.500	3.947	0.000	3.947
47	STRUT FAIRING RHS		8.272	4.655	0.089	4.656
48	STRUT FAIRING RHS		7.954	4.738	-0.989	4.840
49	STRUT FAIRING RHS		7.083	5.093	-1.613	5.342
50	STRUT FAIRING RHS		6.108	5.679	-1.618	5.905
51	STRUT FAIRING RHS		5.298	6.279	-1.090	6.373
52	STRUT FAIRING RHS		4.901	6.601	-0.089	6.602
53	STRUT FAIRING RHS		5.200	6.357	0.962	6.429
54	STRUT FAIRING RHS		5.967	5.777	1.570	5.987
55	STRUT FAIRING RHS		6.929	5.174	1.652	5.431
56	STRUT FAIRING RHS		7.844	4.772	1.125	4.903
57	BACK SHELL	150	4.901	3.300	-5.718	6.602
58	BACK SHELL	30	4.901	3.300	5.718	6.602
59	BACK SHELL	0	4.901	0.000	6.602	6.602
60	BACK SHELL	180	4.901	0.000	-6.602	6.602
61	BACK FACE	0	10.504	0.000	2.500	2.500
62	BACK FACE	180	10.504	0.000	-2.500	2.500
63	PROBE	0	0.205	0.000	2.800	2.800
64	TRAVERSE	0	0.207	0.250	2.800	2.811
65	TRAVERSE	0	0.212	0.500	2.800	2.844

Appendix B. Unsteady Pressure Tap Locations

TAP ID	NOMINAL ANGLE	X, IN	Y, IN	Z, IN	RADIUS, IN	ACTUAL ANGLE
1	0	1.490	0.775	7.374	7.415	6.00
2	0	1.584	0.686	7.584	7.615	5.17
3	0	1.712	0.564	7.755	7.776	4.16
4	0	1.866	0.418	7.880	7.892	3.03
5	0	2.035	0.257	7.961	7.965	1.85
6	0	2.212	0.089	7.997	7.997	0.64
7	0	2.391	-0.081	7.989	7.989	-0.58
8	0	2.566	-0.247	7.937	7.941	-1.78
9	0	2.732	-0.404	7.844	7.854	-2.95
10	0	2.895	-0.558	7.741	7.761	-4.12
11	180	1.490	-0.775	-7.374	7.415	186.00
12	180	1.584	-0.686	-7.584	7.615	185.17
13	180	1.712	-0.564	-7.755	7.776	184.16
14	180	1.866	-0.418	-7.881	7.892	183.03
15	180	2.035	-0.257	-7.961	7.965	181.85
16	180	2.212	-0.089	-7.997	7.997	180.64
17	180	2.391	-0.081	-7.989	7.990	180.58
18	180	2.566	0.247	-7.937	7.941	178.22
19	180	2.732	0.404	-7.844	7.854	177.05
20	180	2.895	0.558	-7.740	7.761	175.87
21	270	1.490	-7.374	0.775	7.415	276.00
22	270	1.584	-7.584	0.686	7.615	275.17
23	270	1.712	-7.755	0.564	7.776	274.16
24	270	1.866	-7.881	0.418	7.892	273.03
25	270	2.035	-7.961	0.257	7.965	271.85
26	270	2.212	-7.997	0.089	7.997	270.64
27	270	2.391	-7.989	-0.081	7.989	269.42
28	270	2.566	-7.937	-0.247	7.941	268.22
29	270	2.732	-7.844	-0.404	7.854	267.05
30	270	2.895	-7.740	-0.558	7.761	265.87
31	330	1.490	-3.016	6.774	7.415	336.00
32	330	1.584	-3.198	6.911	7.615	335.17
33	330	1.712	-3.389	6.998	7.776	334.16
34	330	1.866	-3.578	7.034	7.892	333.03

TAP ID	NOMINAL ANGLE	X, IN	Y, IN	Z, IN	RADIUS, IN	ACTUAL ANGLE
35	330	2.035	-3.758	7.023	7.965	331.85
36	330	2.212	-3.921	6.970	7.997	330.64
37	330	2.391	-4.064	6.878	7.989	329.42
38	330	2.566	-4.182	6.751	7.941	328.22
39	330	2.732	-4.272	6.591	7.854	327.05
40	330	2.895	-4.354	6.424	7.761	325.87
41	0	4.061	0.000	7.087	7.087	0.00
42	0	10.061	0.000	3.623	3.623	0.00
43	180	4.061	0.000	-7.087	7.087	180.00
44	180	10.061	0.000	-3.623	3.623	180.00

Appendix C. Test Condition and Static Pressure Tap Data Archive Description

Whenever data was acquired during the wind-tunnel test, the Standard Data System (SDS) acquired its own set of data to document the test section conditions and the time-averaged static pressures measured on the model. In addition, the wall static pressure measurements made on the test-section walls are in the files in the form of pressure coefficients. The first line of this space-delimited file defines the data in each column. The files are located in the folder titled SDS. The files are named by run number (R0066.dat, for example). The two files named WallPortCoordinate11ftTWT contain the locations of the wall static pressure taps in wind-tunnel coordinates (in feet).

Appendix D. IR Thermography Image Archive Description

All of the acquired IR images are located in the folders named 120CA_ceiling_IR, 120CA_floor_IR, and 120CA_Nsidewall. The folder names refer to the camera locations. The files in these folders are in a proprietary FLIR™ format that is read by the ExaminIR™ software. Non-proprietary images taken from the FLIR™ software are presented in another set of folders named 120CA_ceiling_images, 120CA_floor_images, and 120CA_Nsidewall_images. At least one image (in tiff format) from each run is presented in this folder. In some cases multiple images for particular runs are presented, usually processed over different temperature ranges to bring out different flow features.

Appendix E. PSP Data Archive Description

The PSP data is stored by run and sequence number according to the model geometry. The files are stored in the folders named PSP_AoA_15_Rough, PSP_AoA_30_Rough, and PSP_AoA_30_Smooth. Inside each of these folders is the grid file onto which the pressures are mapped for that particular model configuration (configx.grid) and a folder (named "grid") containing the corresponding pressure data as pressure coefficients. The grids used are multi-grids that are stored in Plot3D format. The corresponding pressure coefficient data is stored in Plot3D function format. Multiple CFD plotting packages are available that can read this data format.

Within the "grid" folders are the individual Cp data files. They are named using the run and sequence numbers (for example, "005503.p3d" which contains data from Run 55 sequence 03).

Appendix F. PIV Data Archive Description

PIV measures the velocity on a grid of points in the measurement area. In this experiment, two stereoscopic PIV systems were used to acquire three components of velocity measured in the PIV coordinate system. In this coordinate system the x-axis is the same as the wind tunnel x-axis. The y-axis for the PIV measurements is the other axis in the plane of the laser sheet. For the high-speed system, the y-axis is the same as the wind-tunnel y-axis. The PIV y-axis for the wide-view system is equivalent to the wind tunnel z-axis. The PIV data is presented in metric units with the x-, y-, and z-dimensions in millimeters (in the PIV coordinate systems) and the velocity data in meters/second.

The PIV data are located in several compressed files (currently located on aeroCOMPASS) listed in the lower left of Table F-1. The wide-view files contain the reduced data from the wide-view PIV system that captured the vertical centerline plane of the wake. The high-speed files contain the data acquired with the high-speed PIV system in a small area of a horizontal plane in the wake. The folders inside these compressed files are structured similarly and are described below. Table F-1 shows the contents of the all the data folders.

Table F-1. Contents of High-speed and Wide-view PIV Data Folders

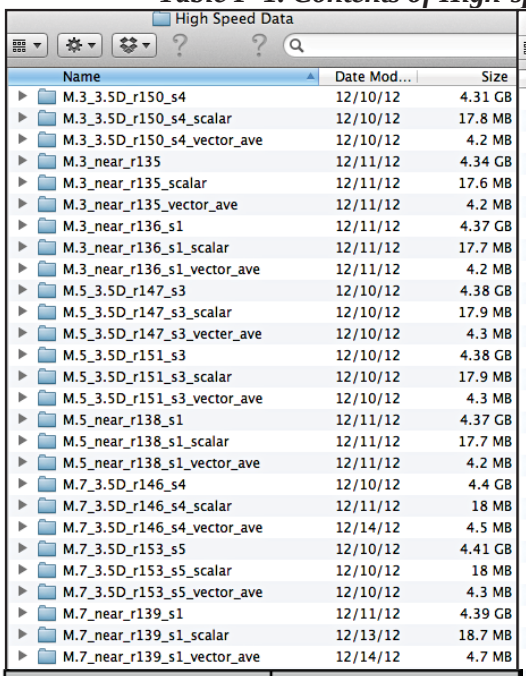

High-Speed Data File Names	Wide-View Data File Names
High-Speed-M03.zip	Wide-View-M03_1of2.zip
High-Speed-M05.zip	Wide-View-M03_2of2.zip
High-Speed-M07.zip	Wide-View-M05_1of2.zip
	Wide-View-M05_2of2.zip
	Wide-View-M07_1of3.zip
	Wide-View-M07_2of3.zip
	Wide-View-M07_3of3.zip

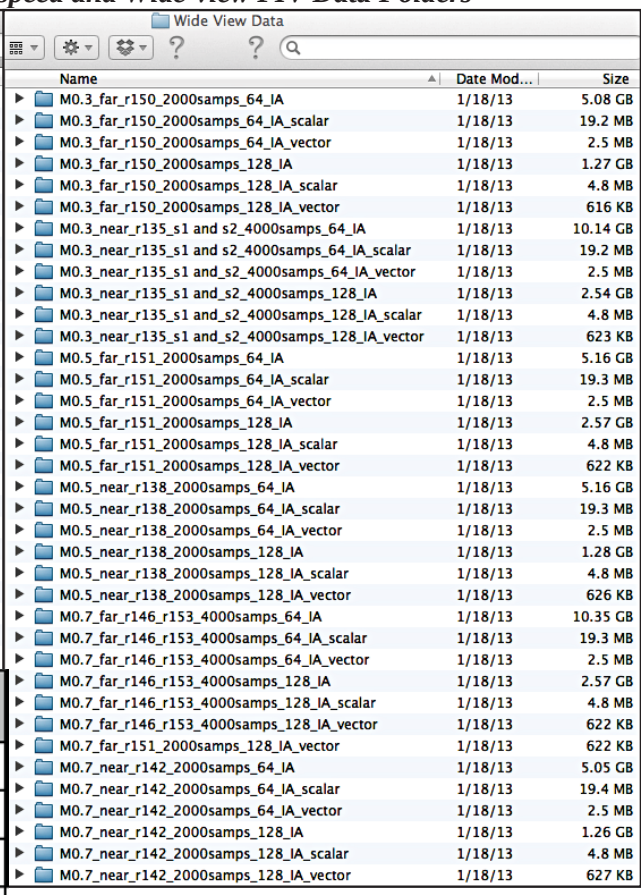

Using the high-speed data as an example, the folder names contain information about the particular run during which the data was acquired. For example, the "M.3_3.5D_r150_s4" folder contains all 2000 of the measured vector fields, in Tecplot format, for run 150, sequence 4 with a free-stream Mach number of 0.3 and the model in its upstream location. For cases with the model in the downstream location the designation is "near" instead of "3.5D". Each file in this folder contains the measurement grid and the velocity vector at each grid point. Detailed information about the test conditions for all of the runs is located in the SDS Data directory on aeroCOMPASS.

There are two other folders that contain information obtained from the 2000 velocity measurements. The folder "M.3_3.5D_r150_s4_scalar" contains statistical information about the

velocity field for run 150, also in Tecplot format. Each of the 15 files contains the measurement grid with a single scalar value associated at each grid point. The values contained in each of the files are shown in Table F-2.

The third folder for each of the PIV runs contains the averaged velocity vector. For the case described above the folder name is M.3_3.5D_r150_s4_vector. This particular file in the folder has the average velocity vector at each of the grid points of the same measurement grid as in the other folders/files for this data point.

All of the high-speed PIV data was acquired at a rate of 2,000 Hz. Each image was processed on 32x32 pixel interrogation areas with 75 percent overlap between adjacent interrogation areas. The entire image area did not have adequate seeding and/or image quality so a smaller area was chosen for the final processing to ensure that the data is of high quality at every grid point. With that processing and image area, the measurement grid provides a velocity measurement approximately every 1.4 millimeters in the x- and y-directions. For the measurements made with the model in the upstream location the measurement area extends approximately 240mm stream wise and 167mm span wise. When the model was located in its downstream position the measurement area was somewhat smaller, extending approximately 152 millimeters stream wise and 170 millimeters span wise. The measurement areas of the high-speed PIV system are shown in Figure F-1. The x and y locations are given in millimeters.

Table F-2. Scalar Data File Contents

File Name	Derived Flow Variable, High-Speed Data	Derived Flow Variable, Wide-View Data
B00001.dat	Average V_x	Average V_x
B00002.dat	Average V_y	Average V_y
B00003.dat	Average V_z	Average V_z
B00004.dat	Average Kinetic Entergy	rms V_x
B00005.dat	rms V_x	rms V_y
B00006.dat	rms V_y	rms V_z
B00007.dat	rms V_z	Turbulent Kinetic Energy
B00008.dat	Turbulent Kinetic Energy	Reynolds Stress, xy
B00009.dat	Reynolds Stress, xy	Reynolds Stress, xz
B00010.dat	Reynolds Stress, xz	Reynolds Stress, yz
B00011.dat	Reynolds Stress, yz	Reynolds Stress, xx
B00012.dat	Reynolds Stress, xx	Reynolds Stress, yy
B00013.dat	Reynolds Stress, yy	Reynolds Stress, zz
B00014.dat	Reynolds Stress, zz	2D Max Turbulent Shear Stress
B00015.dat	2D Max Turbulent Shear Stress	-

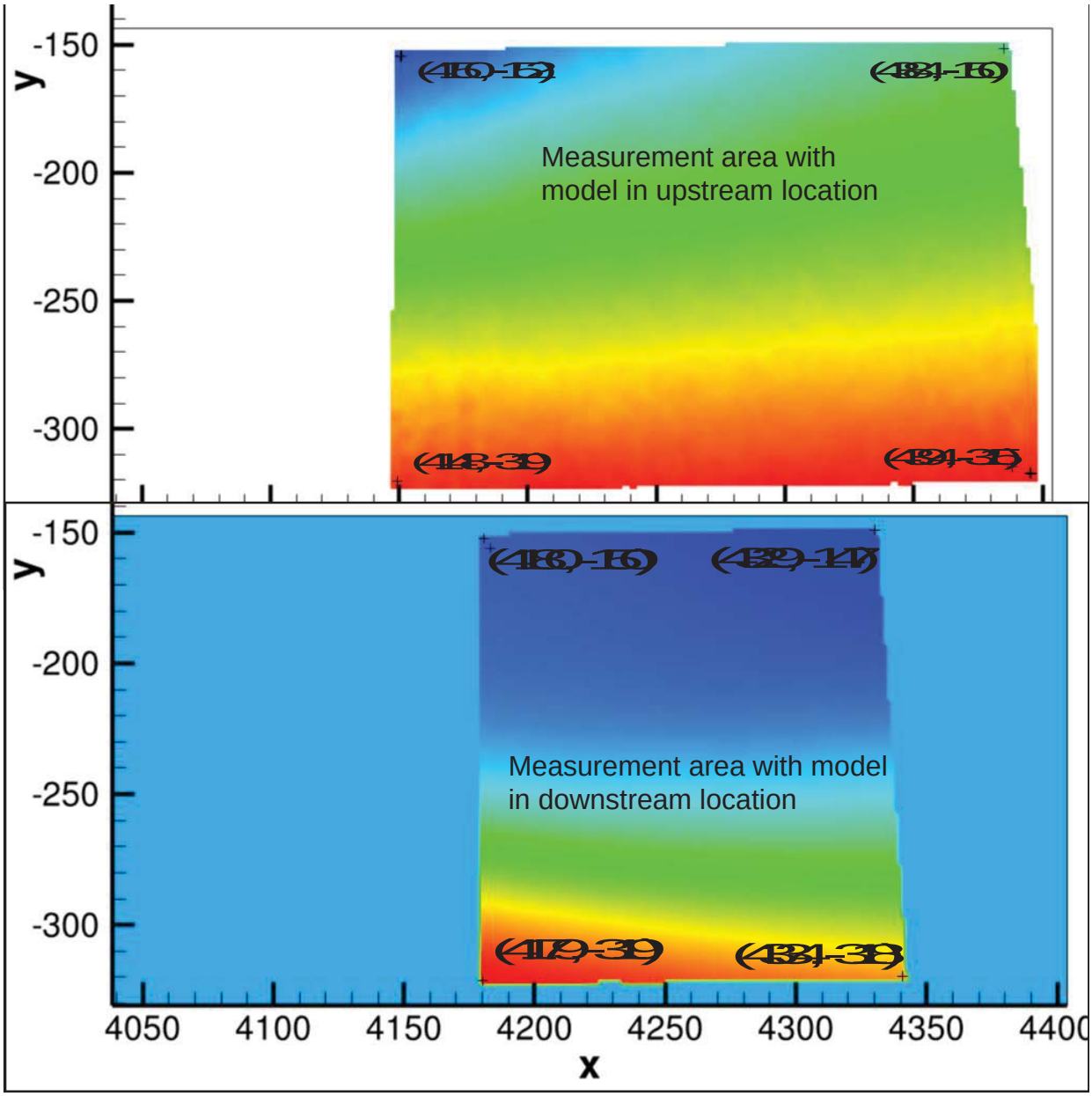

Figure F-1. Measurement Area for High-speed PIV System; Measurements in Millimeters

The wide-view files are arranged in a similar manner, but there are two additional parameters in the file name because results processed on two different interrogation areas are given and additional samples are available for some conditions. A basic folder name for the wide-view data is "M0.3_far_r150_2000samps_64_IA_vector." "M0.3" designates Mach 0.3, "far" designates model in the upstream location (near is for the downstream model location),

"2000samps" says there are 2000 samples for this particular data set ("4000samps" or "_s1 and s2_4000samps" would indicate 4000 samples), and "64_IA" indicates a 64x64 pixel interrogation area (alternate is "128_IA" for a 128x128 interrogation area).

The imaging area was much larger for the wide-view PIV system, but once again not all of the area provided images that could be successfully processed. To summarize some of the issues limiting the useful image area, the laser sheet moved more than desired (probably about 1 sheet thickness or about 5mm), the seed was not uniformly dispersed in the image area, and there were several reflections of stray laser illumination on the test section walls that were visible in the camera images. These imperfections resulted in limiting the size of the area of the flow that could be accurately measured and increased the size of the interrogation area. This effectively reduced the measurement density from that seen from the high-speed system.

A 64x64 interrogation area was the smallest that gave accurate (interrogation-area-independent) average velocity measurements. With 75 percent overlap between interrogation areas, the spacing between measurement points was approximately 5.3mm in x- and y-directions. The cut out in the data at the lower left is a mask applied to the processing surrounding the CM model to prevent glare from the laser reflecting off the model from affecting the PIV measurements. The spacing between measurement points increases to 10.6mm for the 128x128 pixel interrogation area processing. The coarser grid processing gives more reliable results for the statistical information about the flowfield while the time-averaged velocities given in the 64x64 processing are very accurate and the resolution is better than in the coarser processing grid. In all cases, the interrogation area for the wide-view measurements has corner points roughly as shown in Figure F-.2 (wind tunnel coordinates in mm).

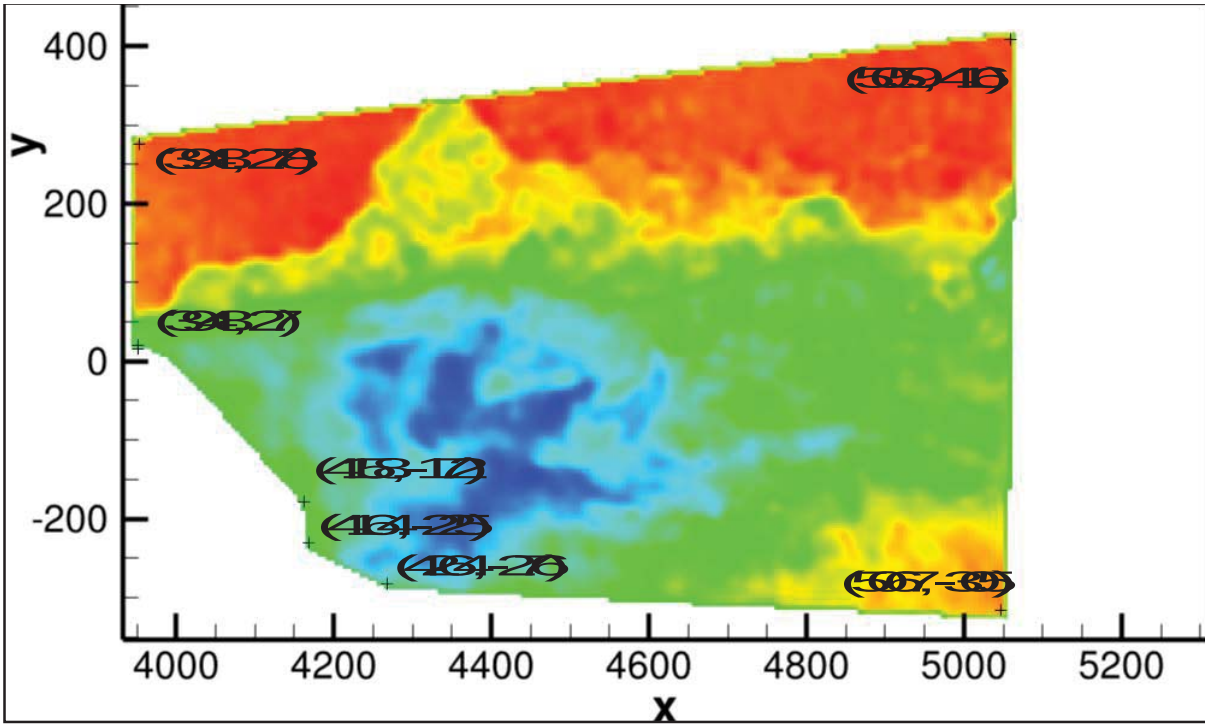

Figure F-2. Measurement Area for Wide-view PIV System; Measurements in Millimeters

Appendix G. Unsteady Pressured Data Archive Description

The unsteady pressure measurements are located on aeroCOMPASS in the final data folder of the 120-CA test location. The unsteady pressure data folder contains a file for each run that includes a summary of the test conditions and the time history of the 44 Kulite® pressure transducers. All data was acquired at a rate of 6400 Hz. The files are comma-separated variable type with names structured as "t11-0247T***xx***p***y***time.cvs" where t11-0247T represents the facility test number, ***xx*** is the run number, and ***y*** is the sequence or point number. When there were multiple data points acquired for a given run, there will be a file for each data point. The data is presented as C_P' at each time step where C_P' is the unsteady component of the pressure coefficient. It is defined as $C_P'(t) = \frac{(P_s(t) - P_\infty) - \overline{P}_s}{q_\infty}$ where $P_s(t)$ is the instantaneous static pressure at time t and $\overline{P}_s$ is the time-averaged static pressure.

Appendix H. Boundary Layer Data Archive Description

The boundary layer data is archived in a folder named "BL data files," currently on the aeroCOMPASS site. Each of the files in this folder contains the boundary layer survey acquired during the run in the file name (BLrun122.txt, for example). The files are tab-delimited text with the first line defining what values are in each of the columns.

REPORT DOCUMENTATION PAGE

Form Approved
OMB No. 0704-0188

1. REPORT DATE *(DD-MM-YYYY)*	2. REPORT TYPE	3. DATES COVERED *(From - To)*
01- 02 - 2014	Technical Memorandum	May 2011 - January 2014

4. TITLE AND SUBTITLE
Orion Multi-Purpose Crew Vehicle (MPCV) Capsule Parachute Assembly System (CPAS) Wake Deficit Wind Tunnel Testing

5a. CONTRACT NUMBER

5b. GRANT NUMBER

5c. PROGRAM ELEMENT NUMBER

6. AUTHOR(S)
Ross, James C.; Schuster, David M.

5d. PROJECT NUMBER

5e. TASK NUMBER

5f. WORK UNIT NUMBER
869021.05.07.07.32

7. PERFORMING ORGANIZATION NAME(S) AND ADDRESS(ES)
NASA Langley Research Center
Hampton, VA 23681-2199

8. PERFORMING ORGANIZATION REPORT NUMBER
L-20384 NESC-RP-11-00697

9. SPONSORING/MONITORING AGENCY NAME(S) AND ADDRESS(ES)
National Aeronautics and Space Administration
Washington, DC 20546-0001

10. SPONSOR/MONITOR'S ACRONYM(S)
NASA

11. SPONSOR/MONITOR'S REPORT NUMBER(S)
NASA/TM-2014-218171

12. DISTRIBUTION/AVAILABILITY STATEMENT
Unclassified - Unlimited
Subject Category 16-Space Transportation and Safety
Availability: NASA CASI (443) 757-5802

13. SUPPLEMENTARY NOTES

14. ABSTRACT

During descent after re-entry into the Earth's atmosphere, the Orion CM deploys its drogue parachutes at approximately Mach 0.7. Accurately predicting the dynamic pressure experienced by the drogue parachutes at deployment is critical to properly designing the parachutes. This NASA Engineering and Safety Center assessment was designed to provide a complete set of flowfield measurements on and around an idealized Orion Crew Module shape with the most appropriate wind tunnel simulation of the Orion flight conditions prior to parachute deployment. This document contains the details of testing and the outcome of the assessment.

15. SUBJECT TERMS
Capsule Parachute Assembly System; Wind Tunnel Testing; Multi-Purpose Crew Vehicle; NASA Engineering and Safety Center; Wake Deficit

16. SECURITY CLASSIFICATION OF:			17. LIMITATION OF ABSTRACT	18. NUMBER OF PAGES	19a. NAME OF RESPONSIBLE PERSON
a. REPORT	b. ABSTRACT	c. THIS PAGE			STI Help Desk (email: help@sti.nasa.gov)
					19b. TELEPHONE NUMBER *(Include area code)*
U	U	U	UU	91	(443) 757-5802